

**Nonlinear Dynamics of Two-Dimensional
Josephson Junction Arrays**

Science

MASSACHUSETTS INSTITUTE
OF TECHNOLOGY

by

JUN 05 1996

Mauricio Barahona García
Licenciado, Universidad Complutense de Madrid

LIBRARIES

Submitted to the Department of Physics
in partial fulfillment of the requirements for the degree of

Doctor of Philosophy

at the

MASSACHUSETTS INSTITUTE OF TECHNOLOGY

May 1996

© Massachusetts Institute of Technology 1996. All rights reserved.

Author

Department of Physics
May 24, 1996

Certified by

Steven H. Strogatz
Associate Professor of Theoretical and
Applied Mechanics, Cornell University
Thesis Supervisor

Certified by

Mehran Kardar
Professor of Physics
Thesis Supervisor

Accepted by

George F. Koster
Chairman, Physics Graduate Committee

Nonlinear Dynamics of Two-Dimensional Josephson Junction Arrays

by

Mauricio Barahona García

Submitted to the Department of Physics
on May 24, 1996, in partial fulfillment of the
requirements for the degree of
Doctor of Philosophy

Abstract

Arrays of superconducting Josephson junctions can be modelled as systems of coupled nonlinear oscillators. We present analytical and numerical studies of the spatio-temporal behavior of two-dimensional, open-ended, frustrated, dc-driven arrays of Josephson junctions at zero temperature, no self-fields. We explore the crossover between arrays in one and two dimensions and clarify the role of the horizontal junctions, which are perpendicular to the direction of current injection. A ladder array with perpendicular current injection and two-dimensional square arrays are considered.

For the ladder, we obtain analytical approximate solutions which include corrections from the edges and/or vortices present in the array. The perturbations decay exponentially in space with a calculated characteristic length. The depinning of the array, and its field dependence, is explained by the edge-dominated instability of the superconducting solutions. This critical current does not change under the inclusion of vortices since they are expelled before depinning at calculated currents. The instability of the whirling solution is analytically explained by a cascade of parametric resonances of the driving frequency with the eigenfrequencies of the lattice which, in this case, produces no steps. At zero field, a new step is observed at this instability. This state is reduced to a system of two coupled nonlinear oscillators and characterized analytically as a subwhirling mode where horizontal junctions oscillate non-negligibly. In conclusion, the horizontal junctions modify the dynamics by introducing an intrinsic inductance through the fluxoid quantization; by modifying the eigenfrequencies; and by effectively enabling fully two-dimensional modes.

Simulations of underdamped and overdamped square two-dimensional arrays for varying frustration are presented. The numerical analysis of period, type of motion of the pendula, phase velocity and spatial distribution characterizes the dynamics. In underdamped arrays, an analytical approximation for the spatially inhomogeneous partially row-switched states predicts the critical currents for some row-switching

events. The flux-flow region in the overdamped case exhibits a similar phenomenon of row-activation, alternation of periodic and aperiodic solutions and a final transition to a rigid whirling phase.

Thesis Supervisor: Steven H. Strogatz
Title: Associate Professor, Cornell University

Thesis Supervisor: Mehran Kardar
Title: Professor of Physics

Acknowledgments

In these years, I have learnt about collaboration and exchange.

I thank my advisor, Steve Strogatz, for his trust and the special effort in keeping a long distance advisee. I value most his clarity, dissective power, and purposeful approach to research.

I thank very warmly my adoptive advisor, Terry Orlando. The collaboration with his group, the weekly meetings, his knowledge of the field have made this thesis possible.

Mehran Kardar, my co-supervisor, was always available close to any deadline and made very relevant comments to the thesis. After enjoying his faultless teaching and the reading of his articles, this could only be taken as a compliment.

One miniparagraph goes to the research group: Herre, Shinya, Amy, Enrique. It is not easy to find people with whom vortices and Yellowstone can be equally enjoyable.

I gratefully acknowledge full support during four years through a Spanish MEC-Fulbright Fellowship.

As for the rest, no long list applies: family and friends. They who should be here, already know. The curious browser need not.

A mis padres

Contents

1	Introduction	11
1.1	General background and motivation	11
1.2	Overview of the thesis	20
2	Ladder array of Josephson junctions	23
2.1	Background	23
2.2	Introduction: model and methods	27
2.2.1	Physical description and model equations	27
2.2.2	Experimental I - V characteristics and numerical simulations .	36
2.3	Superconducting solutions	43
2.3.1	Observed and approximate superconducting solutions	43
2.3.2	Instability of the superconducting solutions and depinning . .	62
2.3.3	Other superconducting solutions with vortices	70
2.3.4	Summary and discussion	87
2.4	Whirling solution	91
2.4.1	Observed and approximate whirling solutions	91
2.4.2	Instabilities in the whirling branch and repinning	99
2.4.3	Novel subharmonic whirling state at zero field	110
2.4.4	Summary and discussion	128
3	Two-dimensional Josephson junction arrays	131
3.1	Background	131
3.2	Introduction: model and methods	137

3.2.1	Physical description and model equations	137
3.2.2	Numerical analysis of simulated I - V characteristics	144
3.3	Array of underdamped junctions	152
3.3.1	Superconducting state and depinning	158
3.3.2	Totally row-switched state	159
3.3.3	Partially row-switched states	161
3.3.4	Flux-flow regime	168
3.4	Array of overdamped junctions	175
3.5	Summary and discussion	184

Chapter 1

Introduction

1.1 General background and motivation

This thesis deals with Josephson-junction arrays, superconducting electronic devices which can be modelled as spatially-extended networks of coupled nonlinear oscillators. The theory of *linear* oscillations, grounded in the concepts of linear algebra, provides the basis for most of the solutions of problems of this kind in physics and engineering [77]. However, even the simplest oscillators, like the pendulum, or almost all natural oscillatory phenomena are intrinsically nonlinear. Recently, the progress in the theory of dynamical systems has opened the possibility of studying those systems where the small-angle linear approximation is not appropriate. Thus, the application of these techniques presents promise for the understanding and reinterpretation of several phenomena in engineering, mathematics, physics and even the biomedical and social sciences [78, 102, 46, 79].

The physical system of our study is an array of interconnected Josephson junctions in a given geometry. A Josephson junction is a microscopic device constituted by a thin ($\sim \text{\AA}$) layer of insulating or normal material between two superconducting islands. This network of weakly connected superconducting domains can be described as an array of coupled nonlinear oscillators (a classical mechanical system) as a remarkable result of modelling the physical system from the principles of quantum mechanics and classical electromagnetism [63, 49]. This mechanical analogue has

proved useful in understanding the properties of the array since the tools of nonlinear oscillations and dynamical systems are readily applicable [78]. In this thesis, we approach the problem from the viewpoint, and with the methods, of nonlinear dynamics in contrast with the more usual static considerations derived from statistical and classical mechanics.

Since its discovery by Josephson [38], the interest in Josephson junctions and their applications has remained steady. The constitutive laws of these devices arise from the fundamental description of superconductors with a macroscopic quantum mechanical wavefunction. When the density of Cooper pairs is constant (as in most applications), the state of the superconducting island is fully described by the phase of the wavefunction. Due to the narrowness of the barrier between the superconducting domains, there is a finite probability of quantum tunneling not only of the single electrons but of the Cooper pairs also. The quantum mechanical calculation of the transmittance establishes that the superconducting current across the device is proportional to the sine of the gauge-invariant phase difference between the islands ϕ . Moreover, when a device dependent critical current is reached, the Cooper pairs break and single-electron resistive tunneling appears. Then, a voltage difference, which is found to be proportional to the time derivative of ϕ , develops between the islands. In short, the superconducting current is described by

$$I = I_c \sin \phi, \quad V = \frac{\Phi_0}{2\pi} \frac{d\phi}{dt}, \quad (1.1)$$

where Φ_0 is the quantum of flux [49].

In the most usual approximation, a capacitive channel is added to the superconducting and resistive ones to account for the geometric capacitance. This constitutes the resistively and capacitively shunted (RCSJ) model for the junction

$$\ddot{\phi} + \frac{1}{\sqrt{\beta}} \dot{\phi} + \sin \phi = I \quad (1.2)$$

where the time and current have been normalized properly, and β is the McCumber parameter [57]. This is the equation of a nonlinear pendulum with damping $\Gamma = 1/\sqrt{\beta}$

and forcing I and, hence, the connection of the electronic device to a mechanical system is shown.

The fundamental equations (1.1) suggest the application of junctions as detectors of electromagnetic radiation and, conversely, as dc to ac convertors. Some of their features are technologically attractive: their frequency can reach up to the THz range; they can be made very uniform; and they are energetically efficient. However, their applicability is severely diminished by the low voltage (mV) and power output levels (nW) that a single junction can produce [49].

The most researched solution to overcome these limitations is the fabrication of arrays of junctions, which, in the ideal case, would emit coherently, thus multiplying the output levels. This has been the motivation for an exhaustive search for the optimized parameters which could maximize the output and the coherence. However, the nature of the coupling –intrinsic to the electromagnetic and quantum mechanical constraints of the system and, thus, difficult to be tuned directly– makes this task challenging. These considerations constitute the driving force of our research and are discussed at length in the following.

However, these are not the only justifications for the study of these systems. Arrays of Josephson junctions are also viewed as controlled, regular systems where phenomena arising in more complicated, dirty systems can be studied. That is the case of high- T_c superconductors, which, due to their microcrystalline structure, form naturally highly disordered arrays of weak junctions separating the superconducting domains. More intrinsically, their anisotropic crystalline structure can be viewed itself as a stack of superconducting planes separated by insulating regions [43, 42, 87], i.e. a stack of continuous Josephson junctions.

These arrays can also be used as clean models of flux-flow systems, such as flow of vortices across a continuous type-II superconductor with random pinning sites [16, 74]; or other microscopic systems with intrinsic randomness like charge density waves [30] or arrays of metallic dots [59]; as well as Frenkel–Kontorova models [26, 10, 56] or lattices of coupled chaotic maps [69] .

In addition, these systems provide an excellent area for the interplay between

experiments, numerical simulations and theory. In particular, numerical simulations constitute a powerful tool in this context since they grant an accurate representation of the experimental observations (see Chapter 3). Moreover, the system being deterministic in nature allows for analytical approaches which make use of the concepts of classical mechanics, electrodynamics and, more recently, nonlinear dynamics. The equations of the system are also of interest from a purely mathematical viewpoint. On one hand, the high dimensional system of coupled differential equations can be reduced, in some cases, to standard discrete equations, e.g. sine-Gordon [99]; on the other hand, the continuum version of the equations can be translated in terms of a fluid mechanical description [95]. In summary, these systems constitute an interesting example where the behavior of spatially-extended nonlinear dynamical systems can be studied.

If the arrays are to be used as emitters, the most important characterization is the voltage response when a dc current is injected in the array. A graph which shows how the averaged voltage difference across the array $\langle V \rangle$ depends on the injected current I , is called an I - V characteristic. The ac properties can be explored by studying the time-dependent voltage. I - V characteristics are common tools to study the behavior of electronic devices. We summarize in this light the features of the single junction, described by (1.2). As stated above, below a critical current –equal to 1 in the normalized form of the equation (1.2)– the superconducting channel carries all the current with zero potential. Above $I = 1$, however, the current has to flow through the other non-superconducting channels (resistive and capacitive) and, thus, a potential develops. In fact, the junction switches to a branch characterized by a quasi-ohmic behavior, where the voltage increases almost linearly with the current. When the current is decreased, a hysteretic cycle can occur depending on the value of the McCumber parameter in the system. This simple history-dependent switch was envisioned some time ago as the basis for superconducting computers, which never reached a marketable stage.

The strict equivalence of the RCSJ equation (1.2) to a nonlinear damped pendulum serves to illustrate the observed behavior. In this analogy, I is the driving torque, and

$1/\sqrt{\beta}$, the damping. If the torque is smaller than its critical value, the pendulum has a stationary solution given by $\phi^* = \arcsin I$. However, when the torque reaches the critical value $I = 1$, or $\phi^* = \pi/2$, the static solution ceases to exist and the pendulum “depins”. Then, it can be shown that the junction goes to a unique periodic solution in which the pendulum “whirls” over the top ever more harmonically as I is increased. When the torque is reduced, the system traces its way back reducing its frequency until it reaches the value $I = 1$ again. Then there are two possibilities: if the damping is bigger than a critical value Γ^* , the pendulum goes back to the static solution (it gets “repinned”). If the damping is small, the pendulum has large inertia and it continues to whirl below the depinning torque $I = 1$ until it reaches its repinning value. This is a typical example of a hysteretic loop in which two states coexist and the system can find itself in any of the two depending on its history.

The tools of nonlinear dynamics [78] allow a quantitative description of this picture by analyzing the two-dimensional *phase space* of the system. Note that the dimensionality of the phase space is given by the number of first order differential equations which describe the system and is not related to the *spatial* dimensionality of the system. In short, within this framework: we can characterize the depinning transition as a saddle-node bifurcation; the running periodic solution can be proved to be unique in the cylindrical phase space of the system with analytical arguments; Γ^* can be obtained numerically; and the repinning for the underdamped case can be identified as a homoclinic bifurcation and a limiting behavior can be obtained [31]. If other loads are connected to the single junction, thermal noise is introduced, or ac currents are considered, the dimensionality of the system is effectively increased and more complicated phenomena can be observed [100].

Similar arguments and techniques can be applied to *arrays* of junctions. However, the high dimensionality of the system renders the analytical approaches almost useless. Only when the constraints of the system allow a reduction, can we pursue a full analytical treatment. The methodology can still be used but the solution is necessarily numerical. Finally, another important concept in nonlinear dynamics is that of linear stability of a solution, which is defined as the linear response when a

small perturbation is added on a solution of the system. In very basic terms (only strictly valid for the one-dimensional case), if the perturbation grows, the system is linearly unstable; if it decreases, it is stable; otherwise, it is neutrally stable. More complicated behaviors exist when the dimensionality of the phase space is higher, including the possibility of limit cycles (periodic), saddle points and cycles (stable in some directions, unstable in others) or chaotic attractors (bounded, fractal, aperiodic structures in phase space).

In Figure 1-1 we summarize some of the geometries for arrays of junctions which have been investigated in the literature. The complexity which emerges from just one junction is an indication of the very convoluted behavior that arrays can present. This is specially so, since the junctions are coupled in the array via intrinsic physical constraints: conservation of current at each node (Kirchoff's law) and the fluxoid quantization condition (resulting from the restrictions on the winding numbers on the quantum mechanical phase which describes the superconducting islands). An immediate realization of this effect is the SQUID configuration, formed by two junctions, as shown in the figure, and widely used as a very sensitive magnetic detector [63, 49]. The fact that the coupling is intrinsic –hence, not directly accessible to direct external tuning–makes the search for optimized configurations which favor coherent oscillation considerably more difficult.

The initial effort was directed towards *one-dimensional* arrays with mixed experimental results [36]. The series array presents interesting dynamical properties as it can be classified as an almost integrable system [97]. It is also related to one of the classic examples in the theory of coupled oscillators, the Kuramoto model [45, 98]. More recently, one-dimensional parallel arrays have been the object of attention as realizations of a discrete sine-Gordon system, a mathematically challenging problem [96, 94, 99]. In addition, arrays formed as a stack of inductively coupled one-dimensional parallel arrays are being investigated [20, 87] in order to assess their technological properties as an intermediate between the pure 1-D case and two-dimensional systems.

There have been strong indications that *two-dimensional* arrays, both in the square and the triangular geometries [106], present some of the desired technological char-

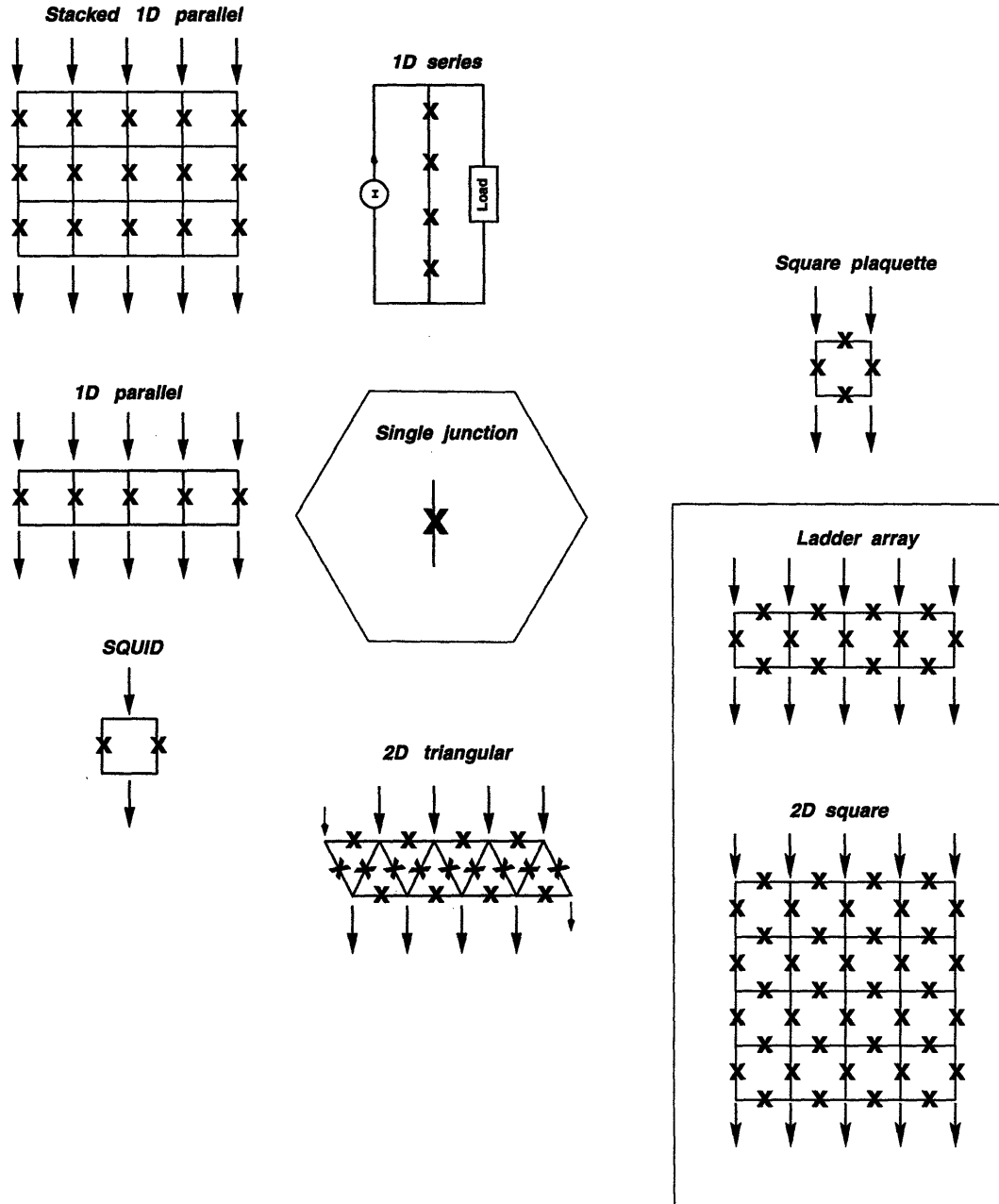


Figure 1-1: Arrays of Josephson junctions and some of their geometries. For a review of one-dimensional series arrays see [97]. Recent work on one-dimensional parallel arrays is presented in [99], and on-going research on stacked 1D parallel (also called two-dimensional shorted arrays), in [20, 87]. The work presented in this thesis deals with the ladder array (Chapter 2) and two-dimensional square arrays (Chapter 3). A summary of the extensive literature on ladder and two-dimensional arrays is presented in the introductions to both chapters.

acteristics [9], i.e. a tendency to phase-lock due to intrinsic coupling intra- and inter-rows [101]; and stability against disorder [62]. These make them the most promising candidates for practical applications. However, the precise mechanism for phase-locking and the dependence on the design parameters is still not well understood. As seen in Figure 1-1, two-dimensional arrays are characterized by the presence of horizontal junctions in the links perpendicular to current injection. It is important to clarify the role of the horizontal junctions in the observed differences with one-dimensional arrays (where they are not present). Numerical simulations show that, to zeroth order, the currents through the horizontal links (and, hence, the phases of the horizontal junctions) are almost always, and in all dynamical regimes, close to zero. In other words, the relevant dynamical behavior is restricted to the junctions in the vertical links of the array. Thus, to this order of the approximation, the two-dimensional array would behave as a juxtaposition of one-dimensional arrays.

The aim of this thesis is to understand where some of the differences between one-dimensional and two-dimensional systems arise. It will become apparent that the presence of horizontal junctions introduces degrees of freedom in the system which enable the appearance of full two-dimensional behavior. This is explicitly shown by considering the simplest case where horizontal junctions are present, the *ladder array* [41, 13, 34, 71]. Although this geometry is quite peculiar, due to the strong constraints introduced by the edges, there are remarkable coincidences with the dynamical behavior of two-dimensional arrays. The obvious advantage of this system is the reduced dimensionality which allows for analytical treatment of the problem. The physical pictures deduced from this system will be used to characterize the 2-D behavior.

For instance, one our conclusions is that, although valid in certain limits, the approximation in which horizontal junctions are basically neglected constitutes an oversimplification. The first effect of the presence of the horizontal junctions is the appearance of an implicit small self-inductance on each cell, even if the inductances of the currents, i.e. self-fields, are neglected. In other words, consecutive vertical junctions are coupled *via* the horizontal ones. This is in contrast with the one-

dimensional parallel case, where the junctions are coupled through the inclusion of self-inductances in the problem. This effect follows from the physical consideration that librating junctions act effectively as inductors with a Josephson inductance L_J [63]. However, the effect is more subtle: the existence of horizontal junctions modifies the governing equations and, thus, the linearized equations which establish the eigenmodes of the ladder. Hence, these are different to the modes of the corresponding one-dimensional arrays. This explains the differences whenever resonances with the characteristic frequencies of the array are responsible for instabilities or steps. We will also show that the *characteristic decay length* of all perturbations into the array, like the ones caused by edges or by vortices, is also modified by the presence of the horizontal links. Even more revealing of the important role these junctions play is their active, non-negligible participation in two-dimensional modes extended to strongly coupled horizontal and vertical junctions. The understanding gained from the analysis of the ladder is then extended to two-dimensional square arrays. We conclude that the methods and some of the solutions are indeed relevant references for qualitative and quantitative predictions in 2-D arrays.

1.2 Overview of the thesis

To conclude this introduction, we give now a schematic overview of the calculations and results presented in this thesis. Chapter 2 includes studies on the ladder array. After the equations and the numerical methods are developed, the three dynamical regimes are described. Two of them are the array equivalent of the single junction's, i.e. uniformly spatially extended superconducting and whirling solutions. The third regime, which we do not address in detail, is the non-superconducting *flux-flow* region which can be described in terms of propagating solitonic or kink-like solutions fairly localized in space-time.

Section 2.3 concentrates on obtaining approximations to the superconducting solutions which appear in the *dynamical* simulations. In the case of the ladder, only two types of solutions appear: a superconducting solution with no vortices for most values of f , and a configuration which resembles the fully-frustrated solution near $f = 1/2$. After finding the solutions of both types which satisfy the governing equations, we introduce the effect of the edges by obtaining exponential corrections from the linearized equations of the array. These approximate solutions account well for the f dependence of the depinning (critical) current of the ladder. We conclude that, in essence, the depinning of the ladder is edge-dominated almost over the complete range of f . This is a result of the strict geometric constraints in the ladder. It is easily understood that other perturbations of the no-vortex solution will decay exponentially also. Thus, we extend this method to obtain an approximation for the one-vortex solution and to study the dependence of its depinning on the field. The obtained approximation for the vortex in the ladder is favorably compared to the continuum sine-Gordon solution commonly used to describe the one-dimensional vortex, thereby highlighting the differences between both arrays.

In Section 2.4 we deal with the whirling, or ohmic, branch of the ladder array. After obtaining an approximate solution, and including the effect of the edges, the repinning transition is analyzed. There are two main conclusions. First, the repinning is not caused by the homoclinic bifurcation of the individual junctions of the array. It

is due to parametric instabilities, similar to the ones observed in the 1-D parallel array [96], which result from the resonance of the whirling frequency with the characteristic frequencies of the array. The general features of the transition (e.g. no steps are observable) are well explained within this framework. Second, these resonances, by exciting specific modes of the two-dimensional lattice, can produce peculiar dynamical commensurate states which are fully two-dimensional in nature, i.e. it cannot be easily reduced to an “effective” one-dimensional mode.

A novel state of these characteristics is observed at the instability of the whirling branch for $f = 0$. This solution can be fully described in a subspace of drastically reduced dimensionality (two) as a mode where vertical junctions whirl subharmonically and horizontal junctions present a standing wave structure with non-negligible oscillations.

Two-dimensional square arrays are investigated in Chapter 3 in connection with the ladder. For instance, the edge-dominated depinning bifurcation typical of the ladder is only important for small values of f in the case of two-dimensional arrays. That is the region where the no-vortex configuration is the only dynamically stable solution and can explain the observed decay of $I_c(f)$ at low field [12]. In contrast, the whirling solution is very similar to the ladder’s and the repinning picture remains unchanged. To complete the study of the dynamical regimes, we consider 2-D arrays in two limits: under- and overdamped. Underdamped arrays are optimal to explore the structure of row-switching states, where whirling solutions are only found in certain rows of the array [92, 47]. We show that these states can be described in terms of solutions obtained for the ladder and, in doing this, some of the critical currents at which row-switching events occur can be predicted. On the other hand, overdamped arrays do not undergo row-switching due to the null inertia of the pendula. Thus, this is the limit where the flux-flow region unfolds fully. Besides alternation of periodic and aperiodic states, we find other remarkable features in this region. A sequence of row-activation is found at small values of f . This is similar to phenomena reportedly observed in discrete and continuous systems with randomness [16, 74], but appears here in a controlled fashion in the absence of any randomness. Once the flux

moves across the complete array, another transition takes place where the flux-lattice becomes rigid and does not undergo any further internal relative displacements.

Chapter 2

Ladder array of Josephson junctions

2.1 Background

We study first a ladder array of capacitive Josephson junctions at zero temperature, in the classical limit (i.e. we neglect Coulomb charging effects). More specifically, we consider the case of perpendicular current injection I in the presence of an applied magnetic field, or *frustration*, f . This is the simplest example of a device with junctions in both its horizontal and vertical branches. In fact, the strong geometric constraints (imposed by the existence of just one row in the y -direction), together with the intrinsic quantum and electromagnetic constraints of the problem, make the system analytically tractable. In spite of that, the general behavior of the system captures the complexity of the observations for fully two-dimensional arrays. Thus, the detailed results of this chapter, analytical in many cases, will serve as building blocks for the understanding of the general behavior in 2-D. The dynamical regimes in the ladder correspond closely to those in two-dimensional arrays and provide a simple physical interpretation. Moreover, techniques and observed solutions for the ladder are the foundation of some quantitative understanding of the I - V characteristics of the two-dimensional case.

The idea of studying basic units to extrapolate their behavior to the global array

has been exploited in different contexts [75, 60, 61] both to simplify the numerical simulations and to obtain simpler and clearer physical pictures. Indeed, this is the driving force behind recent theoretical and experimental studies of one-dimensional parallel arrays [96, 94, 99] and inductively coupled arrays [20], and has been specifically applied for a ladder and double ladder of overdamped junctions by Filatrella and Wiesenfeld [24] to study the role of the magnetic field in the coupling between rows. Also, Yu *et al.* studied the ac-dc response of ladders and single plaquettes [103].

However, it has been the analysis of superconducting solutions and of ground states which has centered most of the research on ladders. Static solutions of ladder arrays of Josephson junctions were first studied in depth by Kardar [40] who established the connection of this system and the Frenkel-Kontorova model with the discrete sine-Gordon equation under certain approximations. He also pointed out the duality of the system with the Coulomb gas, whose ground state for $T = 0$ and $I = 0$ presents a complicated dependence (devil's staircase) on the frustration. In a later contribution, he observed that these ladders possess a thermodynamic critical magnetic field $f_{c1}(I)$ below which the Meissner-like no-vortex solution is the ground state of the system—a behavior which resembles that of Type-II superconductors [41]. He estimated the value of the critical field for an isotropic ladder as

$$f_{c1}(I = 0) = \frac{2\sqrt{2}}{\pi^2} \simeq 0.29$$

which increases as the current is increased. Benedict [5] confirmed the exclusion of vortices below f_{c1} by performing a numerical search of the ground states with a gradient descent method. He also concluded that, in the absence of an external current, the ground states for $f > f_{c1}$ contain vortices and obtained the ground states for commensurate frustrations $f = 1/2$ and $f = 1/3$.

In the very last stages of the writing of this thesis, it was pointed to me by Prof. M. Kardar that this physical picture has been recently substantiated through a statistical mechanics transfer matrix method for $I = 0$ [13]. Among other results, Denniston

and Tang estimate the critical field f_{c1} and give a schematic procedure to obtain the critical current for the depinning of the vortex. This static method arrives at some of our conclusions and expressions with a more complicated formulation arising from a different approach to the problem. Moreover, the effect of the current is not taken into account in a unified manner.

Under this renewed interest in ladder arrays, two other numerical studies dealing with superconducting states of the ladder have also appeared recently. The first one, by Mazo *et al.* [55], explores the complicated landscape of ground states for $I = 0$ as the frustration is varied and introduces a Langevin term to estimate how they relax to equilibrium when a small temperature is present. On the other hand, Hwang *et al.* [34] are much closer to our own work. They present numerical I - V characteristics from dynamical simulations of overdamped ladders in two distinct geometries: a ring and an open-ended array with parallel current injection. They conclude that the ring presents vortex exclusion for a field $f_{c1\perp} < f_{c1}$ and there is no such vortex exclusion in the case of the open-ended array. In Section 2.3, we will show how to interpret these results from a dynamical point of view.

The body of numerical and analytical work for the non-superconducting regimes of the ladder is much smaller. For the ohmic regime we do not know of any analytical study for underdamped ladders as the one we will undertake in this chapter. Our work is an extension of the concepts presented in [96, 99] for one-dimensional parallel arrays and includes new features, applicable to fully two-dimensional arrays, which will be presented elsewhere [95].

The flux-flow regime, in which the dynamics is determined by the propagation of “kinks”, or vortices, has been the object of more attention in the literature. The methods and results in this area are largely based on the theory developed for the solitonic solutions of the conservative undriven *continuum* sine-Gordon equation in a periodic domain [18]. It was shown that even in the presence of damping and driving current, similar solitonic travelling kink solutions exist and can become attractors [51, 11]. Moreover, evidence for switching phenomena has also been provided in the continuum case [25]. More difficulties are found when travelling kinks in *discrete*

lattices are to be described (see [19] for a short review on solitonic-like solutions in discrete systems and [76] for a novel quasi-sine-Gordon discrete system which supports kink travelling waves).

From a more operational point of view, Peyrard and Kruskal [65] showed that the preferred velocities of propagation of kinks for a discrete sine-Gordon system correspond to resonances with the eigenfrequencies of the lattice and are quite independent of the actual shape of the kink. At those velocities the kink propagates in a quasi-stationary manner with almost no loss of energy. The phase-locking of the propagating vortex and the radiation in its wake to form a travelling-wave configuration was exploited by Ustinov *et al.* [86] to predict a series of steps in the low-voltage region (flux-flow) of the I - V characteristic of a one-dimensional parallel array. Since this array can be modelled with the discrete sine-Gordon equation when only self-inductances are considered, they obtained a formula for the resonant voltages at which the velocity of propagation of the kink resonates with the characteristic frequencies of the lattice. A more mathematically rigorous derivation of this idea was carried out in [94, 99] and checked experimentally on a 1-D parallel array in the ring geometry. Recently, in the “wake” of this work, Ryu *et al.* [71] have shown that, under certain approximations, a continuum version of the ladder array can be reduced to a sine-Gordon equation with an effective coupling parameter. Thus, they identify the ladder array with a one-dimensional parallel array with an effective inductance produced by the presence of the horizontal junctions.

We will emphasize in the rest of the chapter that, although this can be a good approximation under certain constraints, it oversimplifies the problem since the presence of the horizontal junctions introduces true two-dimensional characteristics in the system. This can explain the similarities between the dynamical regimes of the ladder array and of two-dimensional systems, despite the singular constraints of the ladder configuration.

2.2 Introduction: model and methods

We now give a general introduction to the features of the underdamped square ladder array with perpendicular current injection. We first describe the physical basis of the device, establish the mathematical formulation of the physical principles involved, and deduce the model equations for the system. In the second subsection, we introduce the I - V characteristics, which constitute the experimental and numerical tools used to characterize the system. We conclude by summarizing the main properties and regimes of the I - V curves. The description and characterization of this behavior constitutes the focus of the rest of the chapter.

2.2.1 Physical description and model equations

As an analytically tractable quasi-two-dimensional system, we choose to study an open ended $N \times 1$ square ladder array with perpendicular current injection. The experimental array consists of two rows of $(N + 1)$ superconducting islands weakly linked through Josephson junctions. There are leads on every island of the top and bottom rows, which inject a uniform dc current to the top and uniformly extract it from the bottom. In addition, an external magnetic field \mathbf{B}_{ext} may be applied perpendicularly to the plane of the array. A cell of this simplest example of a two dimensional square array is represented in Figure 2-1; the complete array, in Figure 2-3.

The mathematical formulation of the problem results from the quantum mechanical description of Josephson junctions, and of several simplifications which we now discuss.

Within the macroscopic quantum model approximation [63], the state of each superconducting island is described by a macroscopic complex quantum mechanical wavefunction Ψ with its corresponding magnitude r and phase Θ . When the electronic density over the array is constant, the magnitudes can be taken as constant so that our problem is completely defined by the $2N + 1$ *node* variables: $\{\Theta_j^{\text{top}}, \Theta_j^{\text{bot}}\}$ with $j = 1, \dots, N + 1$ (i.e. the phases of the islands except for one which is grounded).

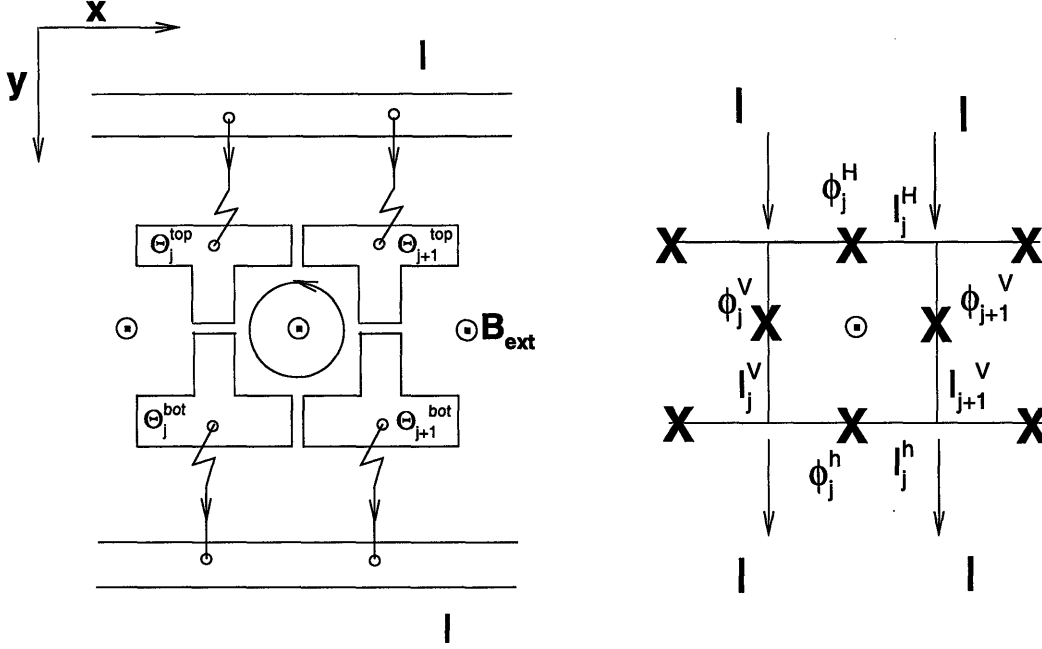


Figure 2-1: Equivalent representations with node (left) and branch (right) variables of the j^{th} cell in the array.

We will find more convenient to work with *branch* variables associated with the Josephson junctions. Each branch, or junction, is described by a gauge invariant phase difference ϕ which, for the junction between generic islands l and m , is given by

$$\phi_{l,m} = \Theta_l - \Theta_m - \frac{2\pi}{\Phi_0} \int_l^m \mathbf{A} \cdot d\mathbf{l} \quad (2.1)$$

where Φ_0 is the quantum of magnetic flux and \mathbf{A} is the vector potential of the total magnetic field \mathbf{B} .

Our first simplification appears here. The total \mathbf{B} is the sum of two contributions: the externally applied \mathbf{B}_{ext} and the induced magnetic field \mathbf{B}_{ind} . The latter is produced by the circulating electric currents in the array and can be obtained from them through the inductance matrix. In our calculations, we neglect these self-field effects. In other words, we take the inductances, and \mathbf{B}_{ind} , to be zero. This approximation reduces considerably the complexity of the system and we will keep it throughout this thesis. More realistic calculations, in which self-inductances – or even the complete inductance matrix – are considered, yield qualitatively similar regimes although

present characteristics of their own [67, 66, 85]. However, the present system exhibits the relevant dynamical behaviors with considerably lower computational cost and, in addition, allows analytical treatment. Moreover, it is physically realizable in arrays of aluminum junctions in which, as explained below, self-fields are negligible.

Since the externally applied magnetic field is constant and perpendicular to the xy -plane in which the array is contained, the total \mathbf{B} becomes then

$$\mathbf{B} = \mathbf{B}_{ext} = -\Phi \hat{\mathbf{z}}$$

where Φ is the flux of the applied magnetic field. In what follows, both the area of the cell and its length are taken to be unity.

Next, we eliminate the ambiguity in the vector potential \mathbf{A} by choosing the gauge

$$\mathbf{A} = \Phi y \hat{\mathbf{x}}$$

which obviously fulfils the definition $\nabla \times \mathbf{A} = \mathbf{B}$. Substituting this \mathbf{A} in (2.1), we obtain the gauge invariant phase differences for our array

$$\begin{aligned} \phi_j^H &= \Theta_j^{top} - \Theta_{j+1}^{top} - 2\pi f & j = 1, \dots, N \\ \phi_j^V &= \Theta_j^{top} - \Theta_j^{bot} & j = 1, \dots, N + 1 \\ \phi_j^h &= \Theta_j^{bot} - \Theta_{j+1}^{bot} - 4\pi f & j = 1, \dots, N \end{aligned}$$

where we have defined the frustration $f = \Phi/\Phi_0$ as a parametrization of the external magnetic field in units of the quantum of magnetic flux.

The first physical constraint, the fluxoid quantization, appears by requiring that the quantum mechanical phase Θ be not multivalued, i.e. after integrating around a closed path, the phase must differ by a multiple of 2π

$$\oint_C \nabla \Theta \cdot d\mathbf{l} = 2\pi n \quad n \in \mathcal{Z}.$$

Consequently, the counterclockwise closed path around cell j shown in Figure 2-1

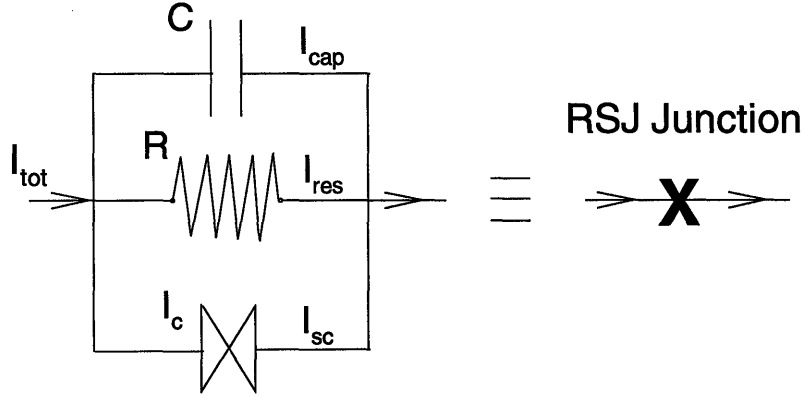


Figure 2-2: RSJ model

yields our first model equation

$$\phi_j^V + \phi_j^h - \phi_{j+1}^V - \phi_j^H = 2\pi(n_j - f). \quad (2.2)$$

This description in terms of the *branch* gauge invariant phase difference is suggested by the two fundamental quantum mechanical results for the dc single Josephson junction:

1. The supercurrent that goes through the junction is related to ϕ through

$$I_{sc} = I_c \sin \phi \quad (2.3)$$

where $I_c(T)$ is the material and temperature dependent critical current.

2. When driven with a dc current $I < I_c$, the junction remains superconducting and $I = I_{sc}$. However, at $I \geq I_c$ the maximum value for the supercurrent is exceeded and part of the current has to flow through non superconducting channels where a finite voltage appears. This voltage is given as well in terms of ϕ by

$$V = \frac{\Phi_0}{2\pi} \frac{d\phi}{dt}. \quad (2.4)$$

This introduces our second simplification: the adoption of the standard Resis-

tively Shunted Junction (RSJ) model with constant resistance. Thus, we mimic the junction's behavior with an equivalent circuit element consisting of three branches in parallel (see Figure 2-2):

- a superconducting element with the Josephson constitutive law mentioned above

$$I_{sc} = I_c \sin \phi$$
- a resistive element R where the voltage aforementioned obeys an ohmic law

$$I_{res} = V/R$$
- a capacitive element C introduced to account for the capacitor-like geometry of the Josephson junctions. For this branch, $I_{cap} = CdV/dt$

Using equations (2.3) and (2.4), we conclude that the total current entering the junction is

$$I_{tot} = I_c \sin \phi + \frac{\Phi_0}{2\pi R} \frac{d\phi}{dt} + \frac{C\Phi_0}{2\pi} \frac{d^2\phi}{dt^2}. \quad (2.5)$$

Now renormalize time

$$\dot{\phi} = \frac{d\phi}{d\tau} \quad \tau = \sqrt{\frac{2\pi I_c}{C\Phi_0}} t = \omega_p t \quad (2.6)$$

and redefine variables

$$I = \frac{I_{tot}}{I_c} \quad \beta = \frac{CR^2 I_c 2\pi}{\Phi_0}, \quad (2.7)$$

where β is the McCumber parameter, ω_p is the plasma frequency and I is normalized to units of I_c .

Thus, we can recast (2.5) in the standard form

$$I = \ddot{\phi} + \frac{1}{\sqrt{\beta}} \dot{\phi} + \sin \phi \equiv \mathcal{D}(\phi) + \sin \phi \equiv \mathcal{N}(\phi). \quad (2.8)$$

This is the main result of the RSJ model: it strictly maps the behavior of a Josephson junction onto that of a driven damped nonlinear pendulum with “torque” I and damping $\Gamma = 1/\sqrt{\beta}$. For simplicity of notation we have defined linear (\mathcal{D}) and nonlinear (\mathcal{N}) operators.

The remaining physical constraints appear due to the geometry of the array and Kirchoff's law of current conservation. Firstly, conservation of current at two generic nodes in the top and bottom rows implies, respectively,

$$I_{j-1}^H + I = I_j^H + I_j^V \quad (2.9)$$

$$I_{j-1}^h + I_j^V = I + I_j^h \quad (2.10)$$

where we have used the notation and system of reference specified in Figures 2-1 and 2-3.

However, the *presence of edges* introduces boundary conditions

$$I = I_1^H + I_1^V \quad (2.11)$$

$$I_1^V = I + I_1^h \quad (2.12)$$

$$I_N^H + I = I_{N+1}^V \quad (2.13)$$

$$I_{N+1}^V + I_N^h = I, \quad (2.14)$$

that is, the currents have to *return* from the ends. Thus, these equations together with (2.9)–(2.10), require necessarily that the currents in top and bottom rows be equal with opposite signs, i.e.

$$I_j^H = -I_j^h, \quad \forall j. \quad (2.15)$$

This particular constraint makes the $N+1$ equations (2.10) redundant, and effectively reduces the problem's dimensionality by $N+1$.

The above “returning current” restriction (2.15) has further implications. There are different configurations of phases $\{\phi_j^H, \phi_j^h\}$ which fulfill that condition. However, only one of them, i.e. $\phi_j^H = -\phi_j^h$, has been observed in our dynamical simulations. We justify now that this is indeed an attracting solution for the system. To that end,

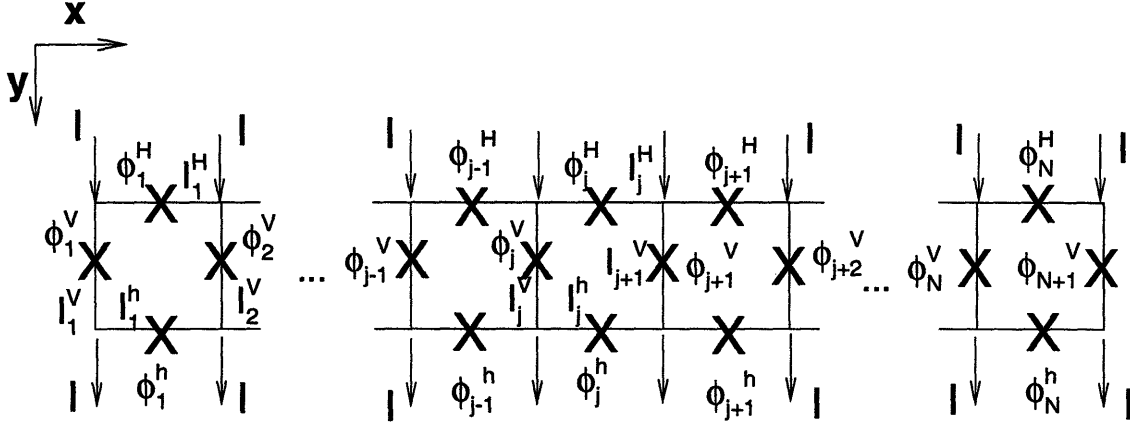


Figure 2-3: Diagram of the ladder array and notation for branch variables.

we perform a standard linear stability analysis on the system

$$\ddot{F} + \frac{1}{\sqrt{\beta}}\dot{F} + \sin F \cos G = 0 \quad (2.16)$$

with

$$F = \frac{\phi_j^H + \phi_j^h}{2} \quad G = \frac{\phi_j^H - \phi_j^h}{2}$$

which has been obtained from (2.15) and (2.8). Note that the equation is invariant under the transformation $F \rightarrow F + \pi, G \rightarrow G + \pi$.

The linear stability analysis [78] of this second order system yields the following fixed points and corresponding stabilities:

1. $F^* = 0 \Rightarrow \phi_j^h = -\phi_j^H \begin{cases} \cos G^* > 0 \Rightarrow |\phi_j^H| < \pi/2 : \text{Stable fixed point.} \\ \cos G^* < 0 \Rightarrow |\phi_j^H| > \pi/2 : \text{Saddle point.} \end{cases}$
2. $G^* = \pi/2 \Rightarrow \phi_j^H - \phi_j^h = \pi : \text{Line of neutrally stable fixed points.}$

where all the phases are defined $\phi_j^H \bmod 2\pi$. The same conclusion is obtained with global techniques by studying the Lyapunov function

$$V(F, \dot{F}) = \frac{\dot{F}^2}{2} + |\cos G| \sin^2 \frac{F}{2}$$

which has a minimum at $F = \dot{F} = 0$ and constantly decreases along any trajectory with rate $\dot{V} = -\dot{F}^2/\sqrt{\beta}$. This does not preclude the existence of running solutions

for which F is not a constant.

In summary, we confirm that the condition (2.15) is operationally equivalent to

$$\phi_j^H = -\phi_j^h, \quad \forall j. \quad (2.17)$$

This is a stable fixed point of the system when $|\phi_j^H| < \pi/2$ and becomes a saddle for larger values of the vertical phases.

This solution has been consistently observed in the simulations of the ladder array represented in Figure 2-3. Therefore, the system of governing equations in this case is constituted by (2.2), (2.8) and (2.9), together with the constraint introduced by returning currents (2.17). We can write it compactly as:

$$\mathbf{f}(\vec{\phi}) = \mathbf{0} \begin{cases} f_j(\vec{\phi}) = \mathcal{N}(\phi_{j-1}^H) - \mathcal{N}(\phi_j^H) - \mathcal{N}(\phi_j^V) + I = 0 & j = 1, \dots, N+1 \\ f_{N+1+j}(\vec{\phi}) = \phi_j^V - \phi_{j+1}^V - 2\phi_j^H - 2\pi(n_j - f) = 0 & j = 1, \dots, N \end{cases} \quad (2.18)$$

where we have defined artificial phases at the ends of the array

$$\begin{aligned} \phi_0^H &= \phi_{N+1}^H = 0 \\ \phi_{N+2}^V &= \phi_{N+1}^V + 2\pi f \\ \phi_0^V &= \phi_1^V - 2\pi f \end{aligned} \quad (2.19)$$

to account for the boundary conditions (2.11) and (2.13).

One third global simplification is the *elimination of the temperature* as a variable, i.e. all our analyses and simulations are carried out at $T = 0$. Thus, our numerical integration of the system of governing equations (2.18) is purely deterministic and does not include a stochastic Langevin term. Likewise, we do not deal with the analytical study of the dynamics of states close to equilibrium [55].

In summary, the ladder array is modelled as an open-ended, frustrated square lattice of coupled damped nonlinear pendula under external drive. We concentrate on the effect of the intrinsic coupling due to the geometric and physical constraints,

and do not consider self-field effects. As will be shown later, the system still presents most of the interesting behavior and regimes of two dimensional $N \times M$ square arrays despite the simplifications introduced in the model equations.

2.2.2 Experimental I - V characteristics and numerical simulations

The standard experimental tool to study the dc properties of a junction array is the measurement of the I - V characteristics, i.e. the dependence of the dc voltage, both time and spatially averaged, on the injected current I . The dc voltage is measured as the current is swept up from $I = 0$ to $I_{max} \gg 1$ (direct path), and back to the origin (return path). Hysteretic effects, i.e. direct and return paths not equal, are observed under certain conditions. The experimental parameters are of three types: applied magnetic field, temperature, and physical characteristics of the array (material, geometry, dimensions, number of junctions).

Experimentally, different values for the inductance and the McCumber parameter β are achieved by varying the temperature. The inductance is inversely proportional to the perpendicular penetration depth

$$\lambda_{\perp} = \frac{\Phi_0}{2\pi I_c \mu_0 d} \quad (2.20)$$

where d is the length of the junction and μ_0 is the permeability of the vacuum. Neglecting field effects, as we do, is equivalent to working in the limit $\lambda_{\perp} \rightarrow \infty$. From their definitions (2.7) and (2.20) we observe that β and λ_{\perp} are directly and inversely proportional to I_c respectively. And it is precisely the critical current that depends on the temperature as given by the Ambegaokar-Baratoff formula [2]

$$I_c(T) = 0.86 \frac{\pi \Delta}{2eR} \tanh\left(\frac{\Delta}{2k_B T}\right)$$

with Δ the material dependent quasiparticle gap and k_B the Boltzmann constant. Thus, as T is increased, I_c is decreased, and λ_{\perp} (β) increases (decreases). Moreover, from equations (2.7) and (2.20) we obtain

$$\lambda_{\perp} \beta = \frac{CR^2}{\mu_0 d}$$

where the right hand side is a combination of geometric and material dependent measurable constants. Hence, it is possible to fabricate devices which cover the desired range of (β, λ_{\perp}) before we reach the critical temperature where the device ceases to be superconducting. The two most usual types of junctions, Nb – Al₂O_x – Nb and Al, correspond to two different ranges of parameters. For niobium junctions, with $R \in [10, 200]$, β remains large as we increase T and only small λ_{\perp} can be attained. On the other hand, aluminum junctions have larger $R \in [800, 1300]$ and, consequently, β can become small and λ_{\perp} , large. As self-field effects are least important in aluminum arrays, they provide the best realization of our idealized model: $T \rightarrow 0$, $\lambda_{\perp} \rightarrow \infty$ over a range of β .

We have simulated I – V characteristics of our system by numerically integrating the governing equations (2.18) for given β , f and number of junctions N [66]. Similarly to the experiment, we sweep the current up from $I = 0$ to I_{max} and back, at very small increments (typically $\Delta I \leq 0.01$). At each point of the I – V curve, the system of $2N+1$ second order coupled differential equations is integrated using an algorithm based on an Adams scheme [66]. First, the system evolves from a given initial condition for a time t_{trans} to eliminate transients. Then, the phases and derivative of the phases of all the junctions over a time t_{av} are calculated. From equations (2.4), (2.6) and (2.7), the potential across junction j is

$$V_j(t) = \frac{I_c R}{\sqrt{\beta}} \dot{\phi}_j(t),$$

and the measurable *spatially and time averaged* voltage $\langle V \rangle$ is

$$\langle V \rangle = I_c R \frac{\overline{\langle \dot{\phi}_j(t) \rangle}}{\sqrt{\beta}}, \quad (2.21)$$

where $\langle \phi \rangle$ and $\bar{\phi}$ represent spatial and time averages respectively. Similarly, $\langle I \rangle = \langle \bar{I} \rangle = I$. Hence, the I – V characteristics, $\langle V \rangle / I_c R$ vs. I graphs, can be easily obtained from our simulations.

Let us briefly describe the typical I – V curve and the critical parameters which de-

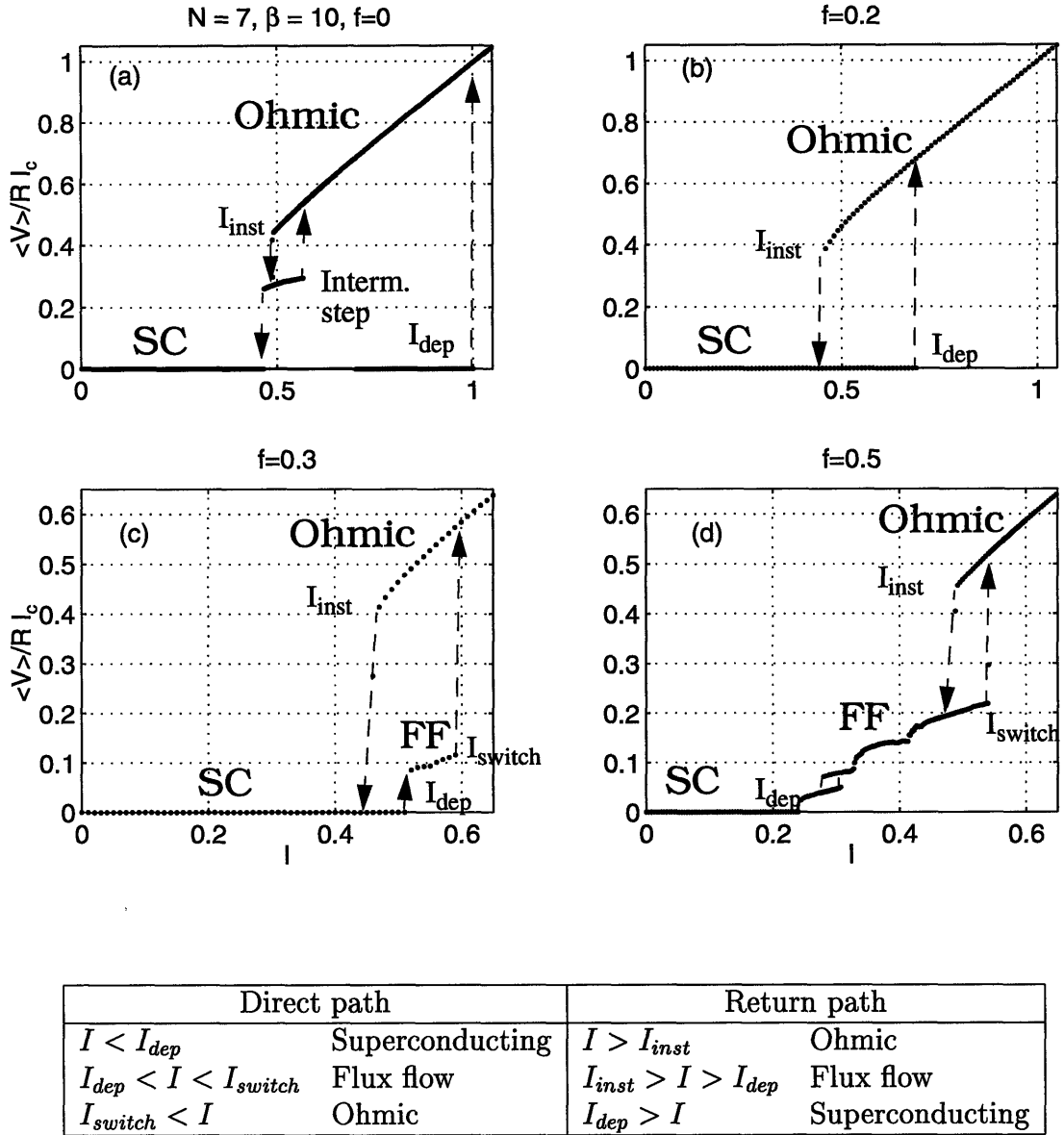


Figure 2-4: I - V characteristics of a 7×1 ladder with $\beta = 10$ and varying magnetic field f and table of characteristic currents.

fine it. As for the direct path up, the system begins and remains on a superconducting solution with zero voltage until it reaches a critical depinning current I_{dep} when it jumps to a non superconducting solution. At high currents, $I \rightarrow \infty$, the behavior is ohmic, i.e. the average voltage per junction depends linearly on the characteristic resistance of the junction $\langle V \rangle = IR$. However, the system does not always jump directly from the superconducting to the ohmic branch. For a range of f , it goes first to an intermediate flux flow regime and eventually switches to the ohmic branch at a certain I_{switch} . The flux flow regime is usually characterized as a pseudo-ohmic (quasi-linear) branch where $\langle V \rangle \simeq IR_{ff}$ with $R_{ff} \ll R$ roughly proportional to f , in the limit of f small.

The return path follows the ohmic branch until it becomes unstable at I_{inst} . If the junctions are overdamped ($\beta \rightarrow 0$) the direct and return paths are the same, i.e. $I_{inst} = I_{switch}$. If β is sufficiently large, there is hysteretic behavior and $I_{inst} < I_{switch}$. When the ohmic branch goes unstable, the system has two options: if $I_{inst} < I_{dep}$, it directly jumps back to the superconducting branch; if $I_{inst} > I_{dep}$, it first goes to the flux flow regime and then, at $I = I_{dep}$, to the original superconducting solution. Representative behaviors are shown in Figures 2-4 and 2-5, where numerical I - V characteristics for different sets of parameters $\{N, f, \beta\}$ are presented, and in Table 2.1, where some numerical critical currents for the ladder are listed.

These data exemplify the following features:

- I_{dep} only depends on f , with almost no β or N dependence. As f is increased, I_{dep} decreases. We will address the issue of depinning of the array in Section 2.3.
- The instability of the ohmic branch occurs at a value $\omega_{inst} \simeq I_{inst}\sqrt{\beta}$ for the frequency of refeeding pendulum. This value is independent of β and very weakly dependent on f and N . The instability of the ohmic branch is the object of Section 2.4.
- The flux flow region is only dynamically accessible for $f > f_{ff}(\beta)$. It is not observable if f is too small, as in Figure 2-4 (a) and (b), or for large β , as in Figure 2-5 (c) and (d).

N	β	f	I_{dep}	I_{switch}	I_{inst}
7	10	0	1.000	1.000	0.491
		1/7	0.796	0.796	0.472
		0.15	0.784	0.784	0.472
		0.2	0.70	0.70	0.46
		0.3	0.51	0.60	0.47
		0.35	0.43	0.56	0.47
		0.4	0.35	0.54	0.484
		0.5	0.24	0.54	0.492
25	10	0	1.000	1.000	0.492
		0.05	0.944	0.944	0.492
		0.1	0.868	0.868	0.484
		0.2	0.692	0.692	0.468
		0.25	0.602	0.630	0.478
		0.3	0.51	0.592	0.472
7	100	0.1	0.87	0.87	0.15
		0.3	0.51	0.52	0.16
		0.5	0.24	0.24	0.17

Table 2.1: Ladder arrays: Values of critical currents for varying N, β, f

- Despite the standard description of the flux flow regime as being quasilinear, there is, for the ladder, some visible substructure in this region, specially when f is large, e.g. Figure 2-4 (d).
- In general, there is a very weak dependence of the I - V curves with N . The only observable changes correspond to slight variations in I_{inst} and the smearing of the substructure and loss of small hysteretic steps in the flux flow region — compare Figure 2-4 (d) and Figure 2-5 (b). The rest of the parameters are virtually independent of the dimension of the array.
- A new step appears on the return path when $f = 0$ and β is moderately large, as in Figure 2-4 (a). It corresponds to a new intermediate state, different to flux-flow, which will be fully characterized in Section 2.4.

Our aim is the explanation of these observations using both numerical and analytical methods. We will focus on reexamining the simplified interpretation which the doubly averaged I - V characteristics provide, under a more complete dynamical

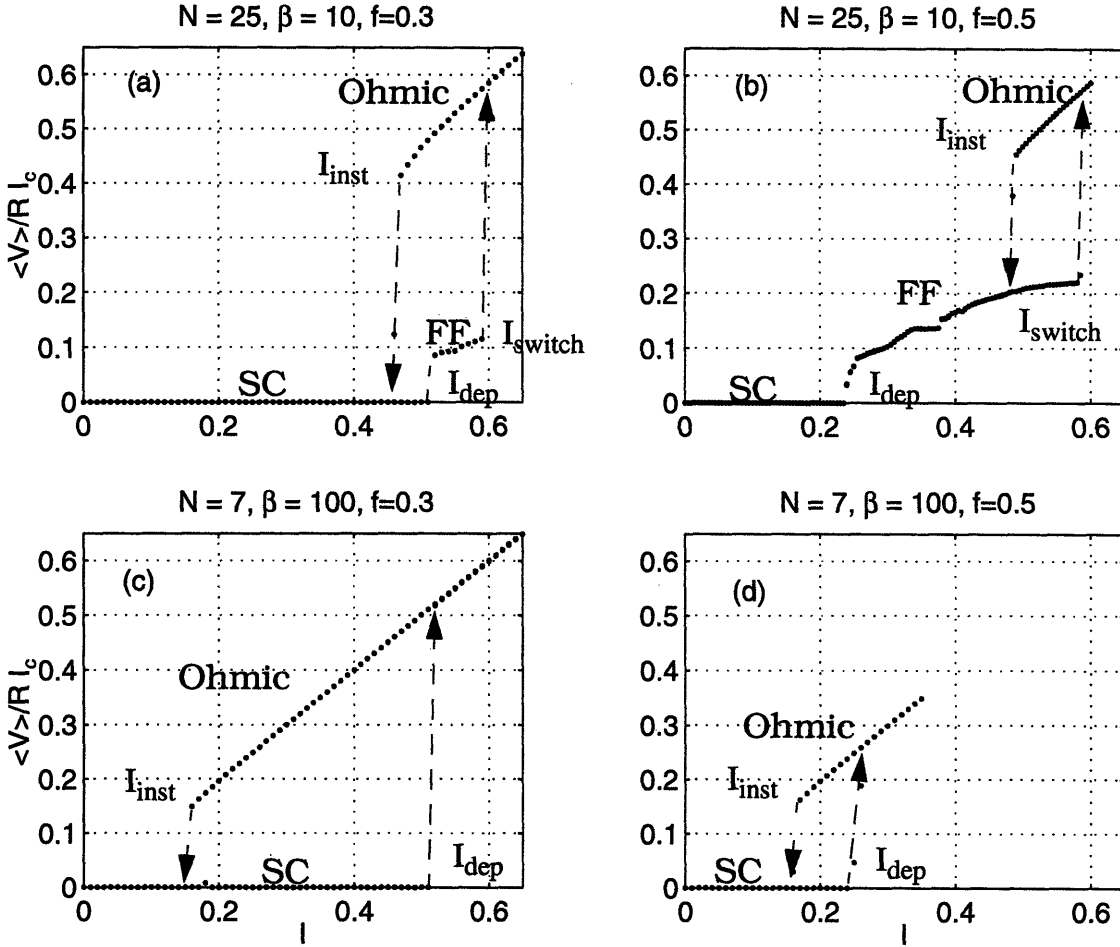


Figure 2-5: Dependence of the I - V characteristics of the ladder array on the number of junctions N and on the McCumber parameter β : (a) and (b) correspond to a 25×1 ladder with $\beta = 10$; (c) and (d) are for a 7×1 device with $\beta = 100$. Compare to the corresponding characteristics for 7×1 and $\beta = 10$ in Figure 2-4(c)-(d).

description of the spatio-temporal solutions of the system. Our scheme is based on three steps:

1. Study the numerical spatio-temporal solutions to the governing equations (2.18) for the different regions of the I - V characteristics.
2. When possible, find analytical approximations to the numerical solutions and check their validity.
3. Interpret the observables of the I - V curves in terms of the assumed solutions.

The following sections of this chapter are organized as follows: we first study the superconducting solutions in connection with the question of depinning. Secondly, we concentrate on the ohmic branch in the return path with emphasis on repinning and zero field steps. The third regime, the flux-flow region, is not addressed in this thesis. Some studies on the propagation of vortices in a ladder have appeared very recently in the literature [71]. Their numerical findings are similar to our results (not included here) concerning the existence of travelling wave solutions which include a modulation superimposed on a kink-like function.

2.3 Superconducting solutions

A numerical and physical description of the three characteristic dynamic regimes of the ladder array –superconducting, flux flow, whirling– was introduced in Section 2.2.2. However, a closer mathematical characterization of those regimes needs to be introduced. We begin here by considering the superconducting branch, which corresponds to time independent solutions, or fixed points, of the system. The depinning current, at which a finite dc voltage appears across the array, corresponds to these superconducting solutions going unstable or ceasing to exist. We divide the section in three parts. Firstly, we describe the superconducting solutions *observed* in our numerical simulations and obtain approximate analytical solutions which take into account the presence of open edges in the array. Secondly, we investigate the depinning transition in ladder arrays through the analysis of the stability of the fixed solutions. Finally, we discuss in the third subsection how the presence of vortices in the array modifies those conclusions. In particular, we describe the solution with one vortex, obtain an approximate solution, and find a dynamical criterion for the depinning of the single vortex in the ladder and its expulsion from the ladder. In all of this, we study how the observed behaviors depend on both the parametrized magnetic field, or frustration $f \in [0, 1/2]$ and the number of junctions N .

2.3.1 Observed and approximate superconducting solutions

As the current is increased from zero, the ladder array remains superconducting until a critical current I_{dep} , the depinning current, is reached. For $I > I_{dep}$, the system ceases to be superconducting and a finite dc voltage $\langle V \rangle$ appears. Here we deal with the superconducting spatio-temporal solutions which are observed when we numerically calculate the $I - V$ characteristics. Remember that these are always generated from an initial condition with all phases and time derivatives of phases equal to zero at $I = 0$. Specifically, we investigate the fixed points of the system, i.e. the solutions with $\dot{\phi} = \ddot{\phi} = 0$ for all the junctions. From the governing equations (2.18) and the definition (2.21) of the spatially and time averaged voltage $\langle V \rangle$, it is clear that

any fixed point of the system is a solution with $\langle V \rangle = 0$. Although it is possible in principle that a non-static solution with strict symmetry constraints might have zero $\langle V \rangle$, the restrictions involved make it very unlikely. We have never observed such a solution.

The superconducting solutions which appear in all our simulations (for varying β and N) are always time independent fixed points, i.e. static solutions, of two kinds:

- Solution A: Given in Figure 2-6 (a) and (b). Appears for a wide range of values of f and is characterized by a constant value of all the phases far from the edges. We denote it as the *no-vortex solution*, as explained below.
- Solution B: See Figure 2-6 (c) and (d). For values of f close to $1/2$, the observed solution presents, far from the edges, an oscillatory pattern in space with wavelength equal to two cell lengths. This is named the *half-filled solution* or fully frustrated solution.

It is also noticeable from Figure 2-6 that the solutions change as the edges are approached. In the following, we deduce analytical expressions for both solutions (A and B) compatible with the governing equations and we include the effect of the edges. We emphasize that these are *not* the only static solutions of the system but the ones numerically observed in our simulations. In Section 2.3.3 below we will argue, however, that solutions A and B are indeed the relevant ones to explain the depinning behavior of the array.

For a time independent solution, the governing equations (2.18) are simplified to give

$$I + \sin \phi_{j-1}^H = \sin \phi_j^H + \sin \phi_j^V, \quad j = 1, \dots, N+1 \quad (2.22)$$

$$\phi_j^V - \phi_{j+1}^V - 2\phi_j^H = 2\pi(n_j - f), \quad j = 1, \dots, N \quad (2.23)$$

where we have defined the artificial phases $\phi_0^H = \phi_{N+1}^H = 0$ and the vertical phases are restricted $\phi_j^H < \pi/2 \forall j$. Moreover, the set of integers $\{n_j\}$ can be set to zero with no loss of generality if the phases are considered as continuous variables. Only when

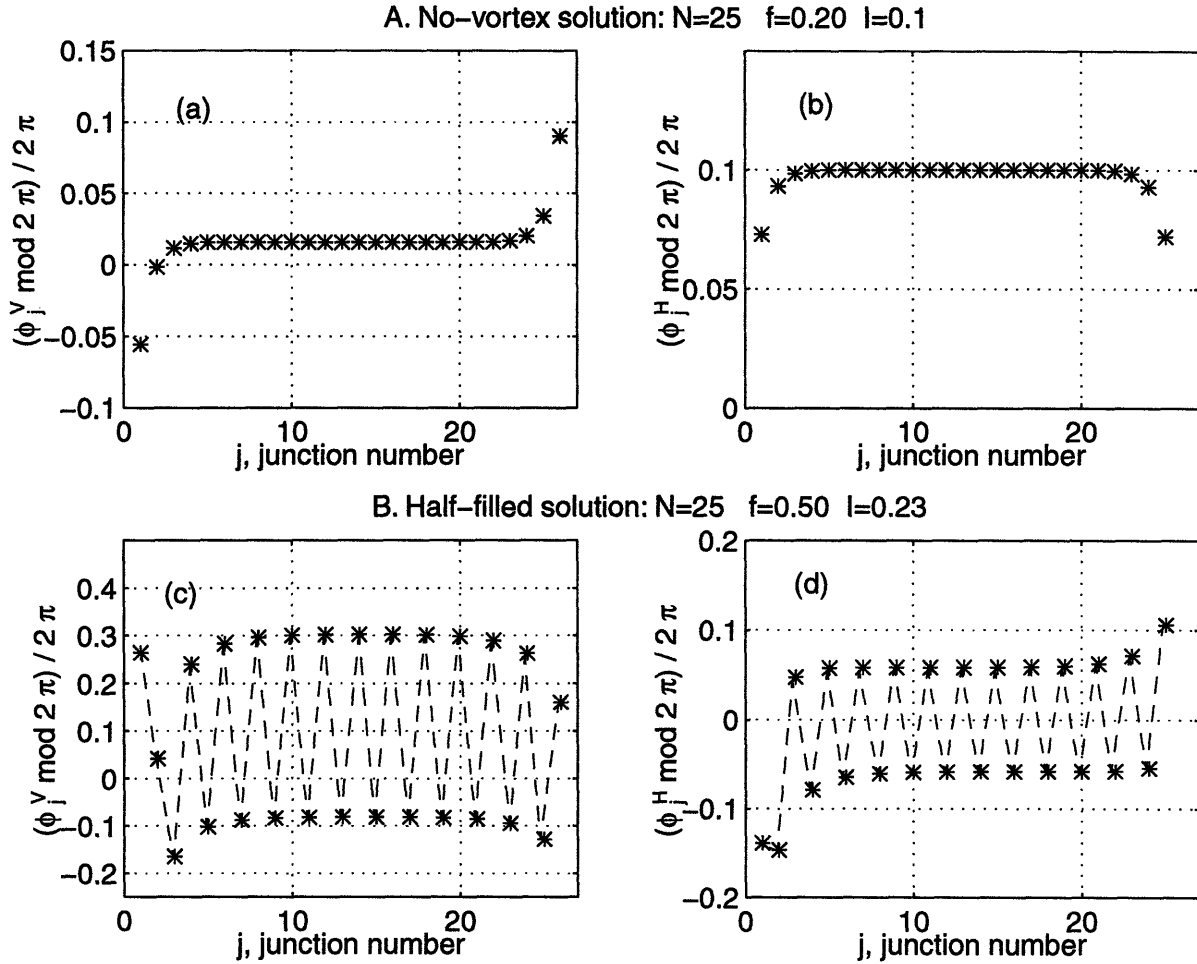


Figure 2-6: Numerical solution for the superconducting branch for a 25×1 ladder array with $\beta = 10$. (a) and (b) correspond to the vertical and horizontal junctions of the *no-vortex solution* (Solution A), obtained when f is small. When $f \simeq 0.5$, the *half-filled solution* (Solution B) is observed, as in (c) and (d). This fully frustrated solution is characterized by an oscillatory pattern with wavelength of two cell lengths. The dashed line is given as a guide to the eye.

the phases are restricted to the interval $[-\pi, \pi)$, these numbers are associated with the presence of topological vortices in the cells.

The external parameters in these equations are f, I and N . It is important to realize that β , the other parameter of our arrays, does not affect the existence of superconducting solutions, as it is not present in the equations. Thus, the independence of the depinning behavior on β observed in the simulated $I - V$ curves discussed in Section 2.2.2) is justified. We find now analytical solutions for this system with the features of the two numerical solutions described above.

A. No-vortex solution

Let us begin by obtaining an expression for the no-vortex solution valid far away from the edges and studying its linear stability. The features of solution A (Figure 2-6) in the middle of the array can be summarized as

$$\phi_j^{V\dagger} = \phi_{j+1}^{V\dagger}, \quad \phi_j^{H\dagger} = \phi_{j+1}^{H\dagger}, \quad n_j = n_{j+1}.$$

Substituting these restrictions in the governing equations (2.22)-(2.23), we obtain the analytical expression for this solution when the effect of the edges is neglected:

$$\phi_j^{V\dagger} = \phi^{V\dagger} = \begin{cases} \arcsin(I) \\ \pi - \arcsin(I) \end{cases}, \quad \phi_j^{H\dagger} = \phi^{H\dagger} = \pi f, \quad \forall j \quad (2.24)$$

where $f \in [0, \pi/2]$. This solution does not exist if $I > 1$ and implies moreover that $n_j = 0, \forall j$. This means there are no topological vortices in the array, which makes clear why we called this the *no-vortex superconducting solution*. Note that the other possible solution $\phi^{H\dagger} = \pi f - \pi$ is unstable for the assumed solution $\phi_j^H = -\phi_j^h$ (see Section 2.2.1, page 33).

We digress now briefly to introduce a general method to study the stability of solutions for the governing equations (2.18), i.e. the *general linear stability analysis* of a given basic solution for our ladder array. It is performed as follows: add a

small perturbation to a given basic solution; obtain the dynamic equations for the perturbation from the *linearized* governing equations of the system; deduce from the dynamics of the perturbation equations what the stability of the solution will be. The results from this development will be used throughout the chapter.

Given an unspecified solution $\{\phi_j^{V*}, \phi_j^{H*}\}$, which fulfills the governing equations (2.18),

$$\mathbf{f}(\phi_j^{V*}, \phi_j^{H*}) = \mathbf{0},$$

consider a solution with small perturbations u_j, v_j

$$\phi_j^V = \phi_j^{V*} + u_j \quad \phi_j^H = \phi_j^{H*} + v_j.$$

Firstly, from (2.19), the boundary conditions for the perturbations are

$$v_0 = v_{N+1} = 0, \quad u_0 = u_1, \quad u_{N+2} = u_{N+1}. \quad (2.25)$$

Secondly, linearize the governing equations (2.18) around the given solution to obtain the dynamical equations for the perturbations

$$\begin{aligned} (\mathcal{D} + \cos \phi_j^{H*})(v_{j-1} - v_j) &= (\mathcal{D} + \cos \phi_j^{V*})u_j \\ u_j - u_{j+1} &= 2v_{j+1}. \end{aligned} \quad (2.26)$$

Combine these two expressions to eliminate v_j and obtain the dynamical equations for the perturbation in the vertical junctions u_j

$$\mathcal{D} \left(\frac{1}{2} \nabla^2 u_j - u_j \right) - \cos \phi_j^{V*} u_j + \cos \phi_j^{H*} \left(\frac{1}{2} \nabla^2 u_j \right) = 0 \quad (2.27)$$

for $j = 1, \dots, N + 1$. Notice that the discrete Laplacian, $\nabla^2 u_j = u_{j+1} - 2u_j + u_{j-1}$, represents a spatial diffusive coupling. A similar term was obtained in one dimensional parallel arrays when inductances are considered [96]. Its appearance here, however, is solely due to the intrinsic coupling that the governing equations introduce. The vertical junctions are coupled *through* the existence of the horizontal ones, even when

inductances are neglected.

We proceed now to obtain the *modal* equations for the perturbations in momentum space by introducing the following pair of Fourier transforms

$$\begin{aligned} u_j &= \frac{\tilde{u}_0}{2} + \sum_{m=1}^N \tilde{u}_m \cos \left[\frac{m\pi}{N+1} (j - 1/2) \right] \equiv \sum_{m=0}^{\prime N} \tilde{u}_m \cos \left[\frac{m\pi}{N+1} (j - 1/2) \right] \\ \tilde{u}_m &= \frac{2}{N+1} \sum_{j=1}^{N+1} u_j \cos \left[\frac{m\pi}{N+1} (j - 1/2) \right] \end{aligned}$$

which satisfy the boundary conditions (2.25). Note the usual definition of $\sum_{m=0}^{\prime N}$, where only the term \tilde{u}_0 is multiplied by 1/2. The use of Fourier series is appropriate since the Laplacian term becomes uncoupled in momentum space

$$\nabla^2 u_j = \sum_{m=1}^N \tilde{u}_m \left\{ -4 \sin^2 \frac{m\pi}{2(N+1)} \right\} \cos \left[\frac{m\pi}{N+1} (j - 1/2) \right].$$

Substituting the Fourier transforms in the spatial equations for the perturbations (2.27), and making use of the orthogonality property

$$\frac{2}{N+1} \sum_{j=1}^{N+1} \cos \left[\frac{m\pi}{N+1} (j - 1/2) \right] \cos \left[\frac{n\pi}{N+1} (j - 1/2) \right] = \delta(m - n),$$

we obtain our general result for the linearized modal equations of the perturbation around a solution $\{\phi_j^{V*}, \phi_j^{H*}\}$ in a square ladder array:

$$\ddot{\tilde{u}}_m + \frac{1}{\sqrt{\beta}} \dot{\tilde{u}}_m + \frac{1}{a_m} \sum_{n=0}^{\prime N} \tilde{u}_n (h_{nm} + v_{nm}) = 0 \quad m = 0, \dots, N \quad (2.28)$$

with

$$\begin{aligned} a_m &= 1 + 2 \sin^2 \left[\frac{m\pi}{2(N+1)} \right] \\ h_{nm} &= \frac{2}{N+1} (a_m - 1) \sum_{j=1}^{N+1} \cos \phi_j^{H*} \cos \left[\frac{n\pi}{N+1} (j - 1/2) \right] \cos \left[\frac{m\pi}{N+1} (j - 1/2) \right] \\ v_{nm} &= \frac{2}{N+1} \sum_{j=1}^{N+1} \cos \phi_j^{V*} \cos \left[\frac{n\pi}{N+1} (j - 1/2) \right] \cos \left[\frac{m\pi}{N+1} (j - 1/2) \right] \end{aligned} \quad (2.29)$$

It is interesting to note from this derivation that the eigenfrequencies of open-ended arrays correspond to the observable frequencies for rings with twice the number of junctions [99].

These expressions become considerably simplified for certain solutions, e.g. when the basic solution is uniform in space. If this is not the case, the stability analysis of the modal equations (2.28) has to be carried out numerically, usually with Floquet methods.

We return now to the study of the stability of the superconducting no-vortex solution $\{\phi_j^{V\dagger}, \phi_j^{H\dagger}\}$ using the general linear stability analysis we just developed. Substituting (2.24) in the general modal equation for the perturbation (2.28) we get

$$\ddot{\tilde{u}}_m + \frac{1}{\sqrt{\beta}} \dot{\tilde{u}}_m + \frac{1}{a_m} \{(a_m - 1) \cos \pi f + \cos \phi^{V\dagger}\} \tilde{u}_m = 0 \quad m = 0, \dots, N \quad (2.30)$$

where $a_m = 1 + 2 \sin^2 \left[\frac{m\pi}{2(N+1)} \right]$.

We begin the stability analysis of the dynamical equations of the perturbation (2.30) by rewriting it as a system of first order differential equations:

$$\begin{aligned} \dot{\tilde{u}}_m &= \tilde{p}_m \\ \dot{\tilde{p}}_m &= -\frac{1}{\sqrt{\beta}} \tilde{p}_m - b_m \tilde{u}_m \end{aligned}$$

with the definition

$$b_m = \frac{1}{a_m} \{(a_m - 1) \cos \pi f + \cos \phi^{V\dagger}\}.$$

The only fixed point corresponds to the null perturbation $u_m = \dot{u}_m = \ddot{u}_m = 0, \forall m$. The Jacobian matrix of the system J_m is obtained by linearizing around that fixed point

$$J_m = \begin{pmatrix} 0 & 1 \\ -b_m & -1/\sqrt{\beta} \end{pmatrix}.$$

Since its trace is always negative, the fixed points will be of one of two types: a saddle point if the determinant $|J_m|$ is negative; or a stable point (spiral or node) if

$|J_m| > 0$, where the sign of the determinant is given by the sign of b_m . $|J_m|$ is always positive for $\phi^{V\dagger} = \arcsin(I)$, $\forall m, I$; i.e. this fixed point is a stable node or spiral for all $I < 1$. On the other hand, when $\phi^{V\dagger} = \pi - \arcsin(I)$, $|J_0| < 0$, $\forall I < 1$. Therefore, this is a saddle point for the $m = 0$ mode and the total perturbation is no longer linearly stable. In summary, when the effect of the open ends is not taken into account, the only stable no-vortex superconducting solution far from the edges is

$$\phi^{V\dagger} = \arcsin I, \quad \phi^{H\dagger} = \pi f, \quad (2.31)$$

where $I < 1$ and all the angles are restricted to the first quadrant. It becomes unstable at $I = 1$ through a saddle-node bifurcation in strict analogy to the single junction.

It is clear from Figure 2-6 (a) and (b) that this is indeed a very good approximation to Solution A in the center of the array. However, as we approach the edges, the approximation becomes increasingly worse. To take into account the effect of the ends, consider a solution

$$\phi_j^{V\dagger} = \phi^{V\dagger} + A_j, \quad \phi_j^{H\dagger} = \phi^{H\dagger} - B_j \quad (2.32)$$

where $\{A_j, B_j\}$ are corrections due to the edges. For this solution to obey the governing equations (2.22)- (2.23), the corrections have to fulfill

$$A_j - A_{j+1} + 2B_j = 0 \quad (2.33)$$

$$I + \sin(\pi f - B_{j-1}) = \sin(\pi f - B_j) + \sin(\arcsin(I) + A_j) \quad (2.34)$$

Far from the edges the corrections are seen to be small. Thus, we linearize the last equation and eliminate B_j and B_{j-1} in the resulting system to obtain a second order difference equation for A_j

$$A_{j+1} - 2\alpha A_j + A_{j-1} = 0 \quad (2.35)$$

with

$$\alpha = 1 + \frac{\sqrt{1 - I^2}}{\cos \pi f} \quad (2.36)$$

and

$$B_j = \frac{A_{j+1} - A_j}{2}. \quad (2.37)$$

The general solution for the difference equation is

$$A_j = Pr^{j-(N+1)} + Qr^{1-j} \quad (2.38)$$

where

$$r = \alpha + \sqrt{\alpha^2 - 1}. \quad (2.39)$$

In conclusion, the correction from the edges can be approximated by a perturbation which decays exponentially from both ends with a characteristic length

$$\lambda = 1/\ln r$$

dependent on I and f as given in (2.36) and (2.39). $\lambda(I, f)$ is a measure of how small perturbations decay inside of an array with the no-vortex superconducting solution.

The last step in our calculation of the edge-corrected solution is the determination of the constants P, Q of equation (2.38) from the boundary conditions

$$\begin{cases} I = \sin(\pi f - B_1) + \sin(\arcsin I + A_1) \\ I + \sin(\pi f - B_N) = \sin(\arcsin I + A_{N+1}), \end{cases} \quad (2.40)$$

which are obtained from current conservation at nodes 1 and $N+1$ respectively. Since the value of the corrections $\{A_j, B_j\}$ becomes larger close to the edges, we improve our numerical solution by solving the boundary equations (2.40) numerically without linearization. Hence, we substitute (2.37) and (2.38) in (2.40) to obtain a system of two nonlinear algebraic equations for the two unknowns P, Q . We can further simplify the solution when we consider the approximation $\lambda \ll N + 1$. In this case, the effect

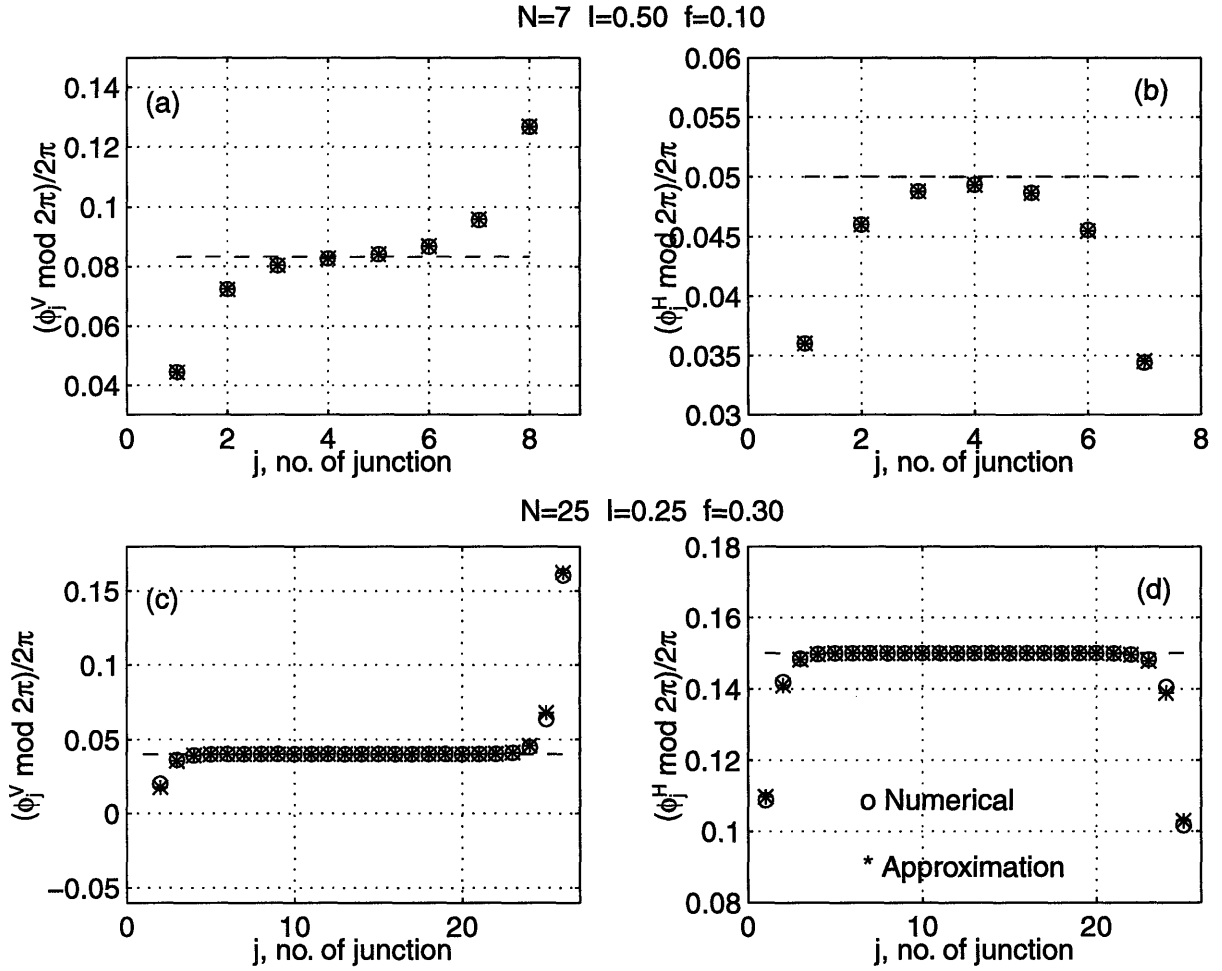


Figure 2-7: No-vortex superconducting solution. Phases of the vertical (a) and horizontal (b) junctions for a 7×1 array with $I = 0.50$ and $f = 0.10$. The asterisks correspond to the numerically observed solution, and the circles to the obtained *approximate* solution $\{\phi_j^{V\dagger}, \phi_j^{H\dagger}\}$. Figures (c) and (d): same as above for $N = 25$, $I = 0.25$ and $f = 0.30$. Note that the approximation is very good even when the array is small. The discontinuous lines correspond to the no-edge solution $\{\phi_j^{V\dagger}, \phi_j^{H\dagger}\}$.

from one end is negligible on the other extreme and the equations become uncoupled

$$I + \sin\left(\pi f - \frac{P}{2}\left(1 - \frac{1}{r}\right)\right) = \sin(\arcsin I + P) \quad (2.41)$$

$$I = \sin\left(\pi f + \frac{Q}{2}\left(1 - \frac{1}{r}\right)\right) + \sin(\arcsin I + Q). \quad (2.42)$$

In that case, P and Q can be obtained independently by solving the corresponding transcendental equation from each boundary condition.

In Figure 2-7 we compare the calculated and observed solutions and find very good agreement. The approximation accounts well for the effect of the open ends both for long ($N = 25$) and short ($N = 7$) arrays. The prediction that the decay of the perturbation from the edges can be parametrized by the characteristic length $\lambda(I, f)$ is also checked satisfactorily in Figure 2-8. Moreover, the corrections A_j and B_j grow as both the field and the current are increased. In addition, our approximation captures other features of the solution like the spatial asymmetry of the *correction* produced by the presence of a non-zero current I , as readily seen in Figure 2-7 by comparing the rightmost and leftmost phases in those examples. It is also observable from the figure that the largest absolute value of the phase is attained as we approach the right end of the ladder. This suggests that it will be the junctions from the right edge which will become unstable first, jumping to a non-static, non-superconducting solution. Thus, when the static solutions cease to be stable, the “natural” direction for the vortices to displace in the array will be from right to left. This is expected from elementary electromagnetism, since the existence of a current produces a force on the vortex, and, thus, introduces a preferred direction for the propagation of vortices in the array.

Similarly, the expected symmetry of the solution under changes of f is easily checked. The governing equations (2.18) are obviously periodic in f , that is, they are invariant under the change $f \rightarrow 1 + f$. Moreover, the observables of the system, like the $I - V$ characteristics, do not change when the transformation $f \rightarrow 1 - f$ is performed. Thus, the restriction in the study of f to the interval $f \in [0, 1/2]$ is justified. It is interesting to note, through a calculation not shown here, that the

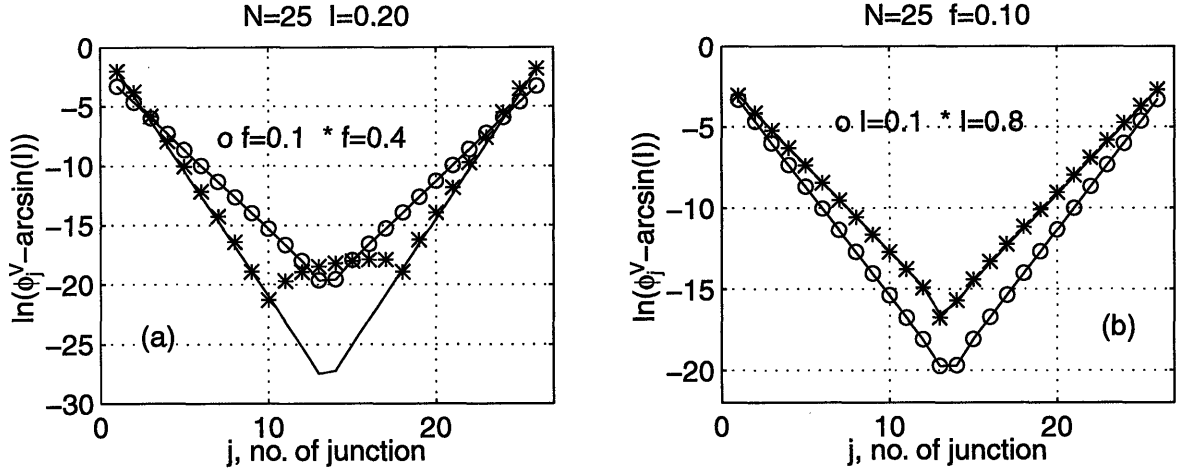


Figure 2-8: Exponential decay of the correction from the edges with varying: (a) magnetic field, f ; and (b) current, I . The solid lines are the predicted values $\pm \ln r$ from equations (2.36) and (2.39).

approximate no-vortex superconducting solutions for $1 - f$, $\{\varphi_j^{V\dagger}, \varphi_j^{H\dagger}\}$, and for f , $\{\phi_j^{V\dagger}, \phi_j^{H\dagger}\}$, are related by the transformation

$$\varphi_j^{V\dagger} = \phi_{(N+2)-j}^V, \quad \varphi_j^{H\dagger} = \phi_{(N+1)-j}^H - 2\pi f$$

. In physical terms: the phase of the vertical junctions for $1 - f$ are a specular reflection, with respect to the center of the array, of the vertical phases for the case with frustration f . This implies that the depinning current will indeed be the same, but the direction of propagation of the vortices will be the opposite: they enter the array from the left and propagate to the right, as can be checked numerically.

We conclude by evaluating the validity of the obtained approximate no-vortex solution. Since the value of the correction becomes larger as f and I are increased, the approximation becomes worse in the limits $f \rightarrow 1/2, I \rightarrow 1$, as shown in Figure 2-9. In fact, $f = 1/2$ is a singular limit for the approximation. Therefore, the approximation is best when f and I are small. This establishes some limits on the applicability of this approximate solution to predict the depinning current, as will be investigated in Section 2.3.2.

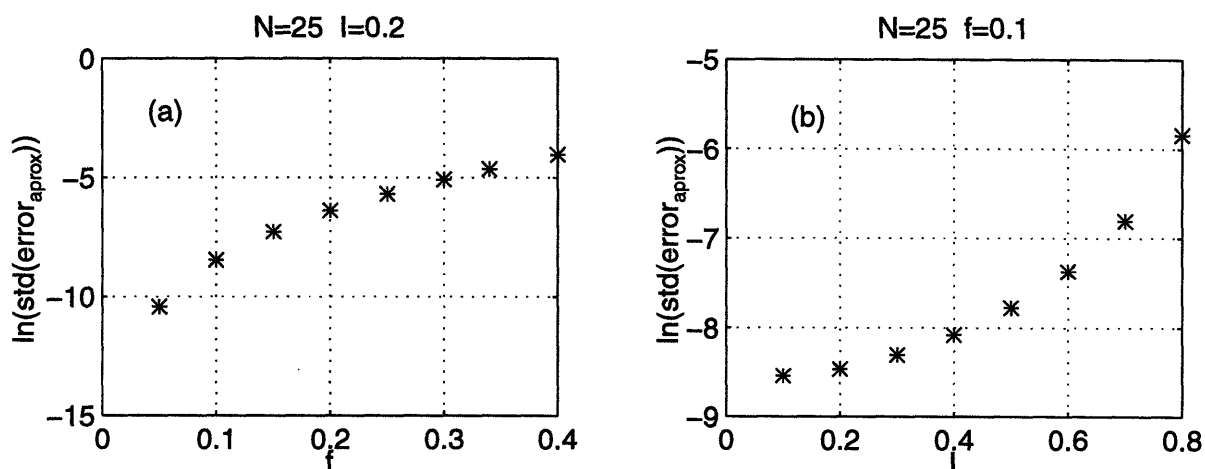


Figure 2-9: Variation of the error of the solution with (a) f and (b) I . As f and I are increased, both the effect of the edges and the error of the approximation get larger.

B. Half-filled solution

The other relevant superconducting solution, the half-filled solution B, appears in our simulations when $f \rightarrow 1/2$, as shown in Figure 2-6 (c) and (d). Following the same scheme as for the no-vortex solution, we begin by obtaining an approximation with the desired characteristics for the junctions far from the edges. The most prominent feature of the observed solution in the middle of the array is its oscillation in space with wavelength equal to two cells. Thus, we assume a superconducting solution for the governing equations of the form

$$\begin{cases} \phi_j^{V^\dagger} = 2\pi[a + (-1)^j b] \\ \phi_j^{H^\dagger} = 2\pi[c + (-1)^j d] \end{cases} \quad (2.43)$$

where a, b, c, d are constants to be determined from the equations.

Substitution of the assumed solution in (2.23) yields two equations for the unknowns c and d

$$c = f/2 - 1/4 \quad (2.44)$$

$$d = b \pm 1/4. \quad (2.45)$$

To obtain this solution, it is necessary to assume an alternating sequence of zeros and ones for the set of integers $\{n_j\}$ in the equations from the fluxoid quantization (2.23)

$$\phi_j^V - \phi_{j+1}^V - 2\phi_j^H = 2\pi(n_j - f), \quad j = 1, \dots, N.$$

This assumption is grounded on the numerics and has the following physical interpretation: A vortex exists in cell j when, after restricting all phases to the interval $[-\pi, \pi)$, $n_j = 1$ in this equation. On the other hand, when $n_j=0$, there is no vortex in the cell. Thus, an alternating sequence $n_j = [1 + (-1)^j]/2$ corresponds to solutions with a topological vortex in every other cell, hence the notation *superconducting half-filled solution* employed here. In expression (2.45), the plus sign corresponds to the solution with $\{n_{\text{odd}} = 1, n_{\text{even}} = 0\}$, and the minus sign to $\{n_{\text{odd}} = 0, n_{\text{even}} = 1\}$. Although these two solutions are degenerate for an infinitely long array, or when periodic boundary conditions are imposed, this is not always the case when the array is open and finite. Note, for example, that if the number of cells is odd, the array contains one vortex more for the first solution than for the second.

The solution for the no-edge approximation is completed by obtaining the relations for a and b in (2.43). Using the spatial periodicity of the numerically observed solution to substitute $\phi_{j+2}^{H\dagger} = \phi_j^{H\dagger}$ in equation (2.22), we obtain

$$\begin{aligned} \sin \phi_{j+1}^{V\dagger} + \sin \phi_{j+2}^{V\dagger} &= 2I \\ \sin \phi_{j+1}^{V\dagger} - \sin \phi_{j+2}^{V\dagger} &= \sin \phi_j^{H\dagger} - 2 \sin \phi_{j+1}^{H\dagger} + \sin \phi_{j+2}^{H\dagger} \end{aligned}$$

which, together with the expressions for c and d , give the last two equations for the unknowns

$$\begin{aligned} \sin 2\pi a \cos 2\pi b &= I \\ \sin 2\pi b \cos 2\pi a - 2 \sin \pi f \cos 2\pi b &= 0. \end{aligned}$$

From these we can solve explicitly for a and b in terms of the parameters of the

problem f and I

$$a = \frac{1}{2\pi} \arcsin \sqrt{L/2} \quad (2.46)$$

$$b = \frac{1}{2\pi} \arccos \sqrt{2I^2/L} \quad (2.47)$$

where

$$L = L(I, f) = (1 + I^2) \pm \sqrt{(1 - I^2)^2 - 16I^2 \sin^2 \pi f}.$$

Moreover, this last equation defines an existence criterion for this particular solution, given by the positiveness of the expression inside the square root. Hence, the half-filled solution does *not* exist if

$$I > I_{hf} = \sqrt{4 \sin^2 \pi f + 1} - 2 \sin \pi f. \quad (2.48)$$

This criterion of existence will be meaningful when we investigate the depinning transition in Section 2.3.2.

This concludes the analytical approximation for the half-filled solution far from the edges or, in other words, when the array is infinite or edge effects are neglected. In Figure 2-10, this no-edge, half-filled approximate solution is shown and compared with the full numerical solutions with very good agreement except for the region near the ends.

It is worth pausing at this point and checking the consistency of our result with those available in the literature. Most of the previous studies on ladder arrays have focused on the case where a magnetic field is present but there is no external driving current, i.e. $f > 0$, $I = 0$. The main interest therein lies in the characterization of the ground state, the complicated landscape of solutions at zero temperature, and of the low-lying excitations around $T = 0$ [5, 40, 41, 55]. A check for our solution (2.43) is provided in [5] where the ground state for $f = 1/2$ is calculated for $I = 0$. It is immediate to verify that the particularization of (2.43)-(2.47) for $I = 0$ yields the

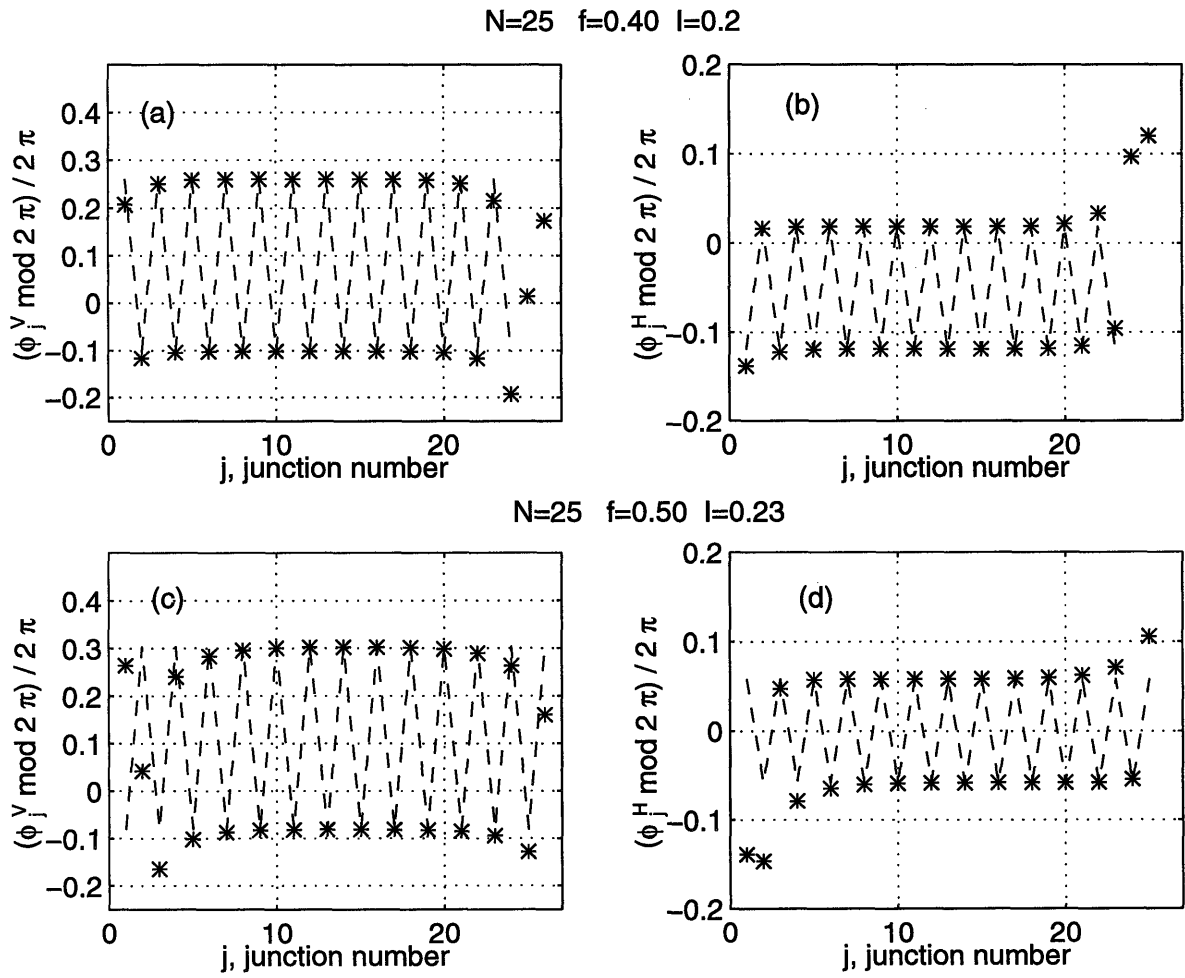


Figure 2-10: Asterisks represent superconducting solutions numerically observed when $f \simeq 1/2$. The discontinuous line, which corresponds to the analytical approximation $\{\phi_j^{V\dagger}, \phi_j^{H\dagger}\}$ neglecting the effect of the edges, is seen to be valid except for a small region close to the ends.

same solution obtained there:

$$\phi_j^{V\dagger} = (-1)^j \arctan(2), \quad \phi_j^{H\dagger} = (-1)^{j+1} \arctan(1/2).$$

There is another possible configuration

$$\phi_j^{V\dagger} = \frac{\pi}{2} [1 + (-1)^j], \quad \phi_j^{H\dagger} = 0$$

which is unstable and is not the ground state of the system. Similarly, we observe that our half-filled approximate solution exists for all fields when $I = 0$, i.e. there is no critical field at which it ceases to exist.

Going back to our development, we analyze now the corrections that the edges introduce in the solution. Following a similar scheme to the one developed for the no-vortex solution above, we represent the effect of the edges as corrections superimposed on the no-edge half-filled solution $\{\phi_j^{V\dagger}, \phi_j^{H\dagger}\}$:

$$\left\{ \begin{array}{l} \phi_{2i-1}^{V\dagger} = \phi_{2i-1}^{V\dagger} + C_i \\ \phi_{2i}^{V\dagger} = \phi_{2i}^{V\dagger} + D_i \end{array} \right\}, \quad \left\{ \begin{array}{l} \phi_{2i-1}^{H\dagger} = \phi_{2i-1}^{H\dagger} - E_i \\ \phi_{2i}^{H\dagger} = \phi_{2i}^{H\dagger} - F_i \end{array} \right\}, \quad i = 1, \dots, \text{ceil}(N/2), \quad (2.49)$$

with an added $\phi_{N+1}^{V\dagger}$ when N is even and with $\phi_{N+1}^{H\dagger} = 0$ when N is odd. Note that we use a double cell to simplify our calculations as suggested by the spatial periodicity of the solution.

When far away from the ends, the corrections are small. Thus, linearizing the governing equations (2.22)- (2.23) around the basic solution (2.43) we obtain:

$$C_i - D_i + 2E_i = 0 \quad (2.50)$$

$$D_i - C_{i+1} + 2F_i = 0 \quad (2.51)$$

$$-E_i \cos \phi_{\text{odd}}^{H\dagger} = -F_i \cos \phi_{\text{even}}^{H\dagger} + D_i \cos \phi_{\text{even}}^{V\dagger} \quad (2.52)$$

$$-F_i \cos \phi_{\text{even}}^{H\dagger} = -E_{i+1} \cos \phi_{\text{odd}}^{H\dagger} + C_{i+1} \cos \phi_{\text{odd}}^{V\dagger}. \quad (2.53)$$

By eliminating E_i and F_i we get: first an expression for D_i ,

$$D_i \left(2 \cos \phi_{even}^{V \dagger} + \cos \phi_{odd}^{H \dagger} + \cos \phi_{even}^{H \dagger} \right) = C_i \cos \phi_{odd}^{H \dagger} + C_{i+1} \cos \phi_{even}^{V \dagger}, \quad (2.54)$$

and finally a second order difference equation for C_i ,

$$C_{i+2} + 2\gamma C_{i+1} + C_i = 0, \quad (2.55)$$

where

$$\gamma = \frac{\sin^2 \pi f + \cos 2\pi f \cos^2 2\pi b - 2 \left[(\sin^2 \pi f - \sin^2 2\pi a) \sin^2 2\pi b + \cos^2 2\pi a \right]}{\sin^2 \pi f - \cos^2 2\pi b}. \quad (2.56)$$

This difference equation has a general solution

$$C_i = Pr^i + Qr^{-i}. \quad (2.57)$$

with

$$r = -\gamma + \sqrt{\gamma^2 - 1} \quad (2.58)$$

which characterizes the penetration depth for the perturbation to die off from the edges. P and Q have to be calculated numerically using the boundary conditions from nodes 1 and $N + 1$. Similarly, from (2.54), the spatial dependence of D_i will be

$$D_i = Rr^i + Sr^{-i}. \quad (2.59)$$

Note that in both equations, i is the number of the double cell.

In Figure 2-11 we check the accuracy of this expression by comparing the calculated penetration depth with data from numerical simulations. To this end, we represent the deviation of the numerical solutions from the no-edge solution $\phi_j^{V \dagger}$

$$C_i^{num} = \phi_{2i-1}^V - \phi_{2i-1}^{V \dagger}, \quad D_i^{num} = \phi_{2i}^V - \phi_{2i}^{V \dagger}$$

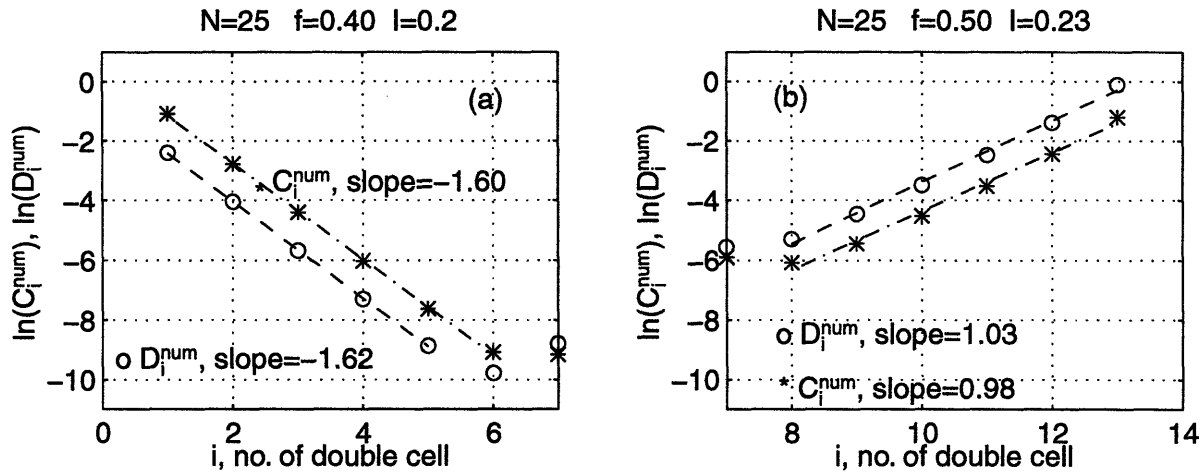


Figure 2-11: Half-filled solution with the same parameters as in Figure 2-10. We represent $\ln(C_i^{num})$ and $\ln(D_i^{num})$ (see text) vs. the number of double cell, i . The slopes of the lines correspond to $\pm \ln r$. Good agreement is observed with the predicted values (2.58) of $\ln r$: 1.61 for (a); and 0.98 for (b).

versus the number of the double cell. We expect from (2.57)-(2.59) an exponential dependence close to the edges characterized by a characteristic length $\lambda = 1/\ln r$. This is verified in the figure where the exponential dependence is indeed observed, and the numerical values for r are seen to agree well with the prediction (2.58). We also observe that the characteristic penetration depth for this solution is never large. Therefore, the effect of the edges on the properties of the half-filled solution is not critical and we will be able to effectively neglect them.

In summary, we have studied and introduced analytical approximations to the two superconducting solutions of the ladder array which appear in our numerical simulations when beginning from a wide spectrum of random initial conditions. Although these are not the only solutions for the system, they exemplify the two extreme cases of the no-vortex and half-filled array solutions. Moreover, we have introduced a general method to take into account the effect of the edges for a given solution. The effect that these corrections have on observables of the system will be explored in the following sections.

2.3.2 Instability of the superconducting solutions and depinning

In this section, we concentrate on the depinning transition of the ladder array from a dynamical point of view. As we increase the driving current I at zero temperature, a critical current is reached for which a measurable average voltage appears. This is the depinning current I_{dep} for which the array ceases to be superconducting. Our main aim is to connect I_{dep} with the stability of the superconducting solutions of the array calculated in the previous section. We emphasize the difference between this *global* depinning of the array, also denoted *critical current* in the literature, and the depinning of the single vortex which we also study in Section 2.3.3.

In page 46, we developed a general linear stability analysis for any given solution of the system. In the preceding section, we used it to study the stability of the no-vortex solution *without* edges and concluded that it becomes unstable at $I = 1$ through a saddle-node bifurcation (Section 2.3.1, page 49). However, the inclusion of the edges introduces an exponential spatial dependence ($r^{\pm j}$) in the solutions which does not uncouple when performing the Fourier Transform to momentum space. Thus, the analysis of the modal equations (2.28) would have to be done numerically with Floquet methods.

We choose instead to study the stability of the system directly from the system of governing equations (2.22)-(2.23) by analyzing its Jacobian matrix. For any fixed point, the Jacobian matrix contains the information about its linear stability. In particular, for a system with M variables and equations, the M eigenvectors and eigenvalues of the Jacobian matrix constitute the set of characteristic directions and exponents which measure the linear growth of a small perturbation in the system. Thus, when all the eigenvalues of the Jacobian are negative, the system is stable in all eigendirections under the addition of a small perturbation. When one eigenvalue is positive, the system is unstable in that direction and the perturbation will grow exponentially. When we go from a situation where all eigenvalues are negative (stable point) to one in which one or more become positive (saddle point), the system

undergoes a bifurcation in its M dimensional phase space. We begin by identifying that the depinning transition corresponds to another saddle-node bifurcation, as for the case where edges were not considered.

In the following, we look for specific static solutions of the system: those whose Jacobian is zero. From the implicit function theorem [39] it can be shown that those are the points where *zero-eigenvalue bifurcations* (transcritical, pitchfork, saddle-node) occur [78]. This constraint on the Jacobian adds one extra equation and one extra variable to the original system, as discussed below.

The original system of $2N + 1$ variables

$$\vec{x} = (x_1, \dots, x_{2N+1}) \equiv (\phi_1^V, \dots, \phi_{N+1}^V, \phi_1^H, \dots, \phi_N^H)$$

and $2N + 1$ equations for the superconducting branch (2.22)-(2.23) can be written as

$$\begin{cases} F_i(\vec{x}) = I + \sin \phi_{j-1}^H - \sin \phi_j^H - \sin \phi_j^V = 0, & i = 1, \dots, N + 1 \\ F_{N+1+i}(\vec{x}) = \sin [\phi_i^V - \phi_{i+1}^V - \phi_i^H + 2\pi f] - \sin \phi_i^H = 0, & i = 1, \dots, N \end{cases} \quad (2.60)$$

where we have used the constraint of the current returning at the edges, $I_j^H = -I_j^h$, and the definitions, $\phi_0^H = \phi_{N+1}^H = 0$. Until now, we have dealt with the problem of obtaining and analyzing solutions to this system

$$\vec{F}(\vec{x}) = \mathbf{0}$$

for a given pair of parameters $\{f, I\}$. Our aim now shifts towards finding, for a given f , the current $I^*(f)$ at which the Jacobian of certain solutions is zero.

The Jacobian matrix of the system, given by

$$J_{i,j} = \frac{\partial F_i}{\partial x_j},$$

is, in this case,

$$\begin{array}{l}
j = 2, \dots, N \\
j = 1, \dots, N
\end{array}
\begin{array}{l}
J_{1,1} = -\cos x_1, \quad J_{1,N+2} = -\cos x_{N+2} \\
\left\{ \begin{array}{l} J_{j,j} = -\cos x_j \\ J_{j,N+1+j} = -\cos x_{N+1+j} \\ J_{j,N+j} = \cos x_{N+j} \end{array} \right. \\
J_{N+1,N+1} = -\cos x_{N+1}, \quad J_{N+1,2N+1} = \cos x_{2N+1} \\
\left\{ \begin{array}{l} J_{N+1+j,N+1+j} = -\cos(x_j - x_{j+1} - x_{N+1+j} + 2\pi f) - \cos(x_{N+1+j}) \\ J_{N+1+j,j} = \cos(x_j - x_{j+1} - x_{N+1+j} + 2\pi f) \\ J_{N+1+j,j+1} = -\cos(x_j - x_{j+1} - x_{N+1+j} + 2\pi f) \end{array} \right.
\end{array}$$

with the rest of the elements equal to zero.

Consequently, we define an augmented algebraic system

$$\vec{\mathcal{F}}(\vec{\chi}) = \mathbf{0}$$

where we have added one variable –the current I – and one equation – the determinant of the Jacobian matrix equals zero– to (2.60):

$$\left\{ \begin{array}{l} \chi_j = x_j, \quad \mathcal{F}_j = F_j = 0, \quad j = 1, \dots, 2N + 1 \\ \chi_{2N+2} = I, \quad \mathcal{F}_{2N+2} = |J_{i,j}| = 0. \end{array} \right. \quad (2.61)$$

We solve this system to obtain configurations of phases (solutions of the system), and the current I^* at which the bifurcation condition is met:

$$\vec{\mathcal{F}}(\vec{x}^*, I^*) = 0. \quad (2.62)$$

There are, of course, multiple solutions for this algebraic system of equations. However, for each family of superconducting solutions, e.g. the set of no-vortex configurations, only one of them, \vec{x}^* with a certain current I^* has a null Jacobian.

We verify in Figure 2-12 that the configurations and critical currents so obtained for varying f are indeed equivalent to the solutions at depinning from *dynamical*

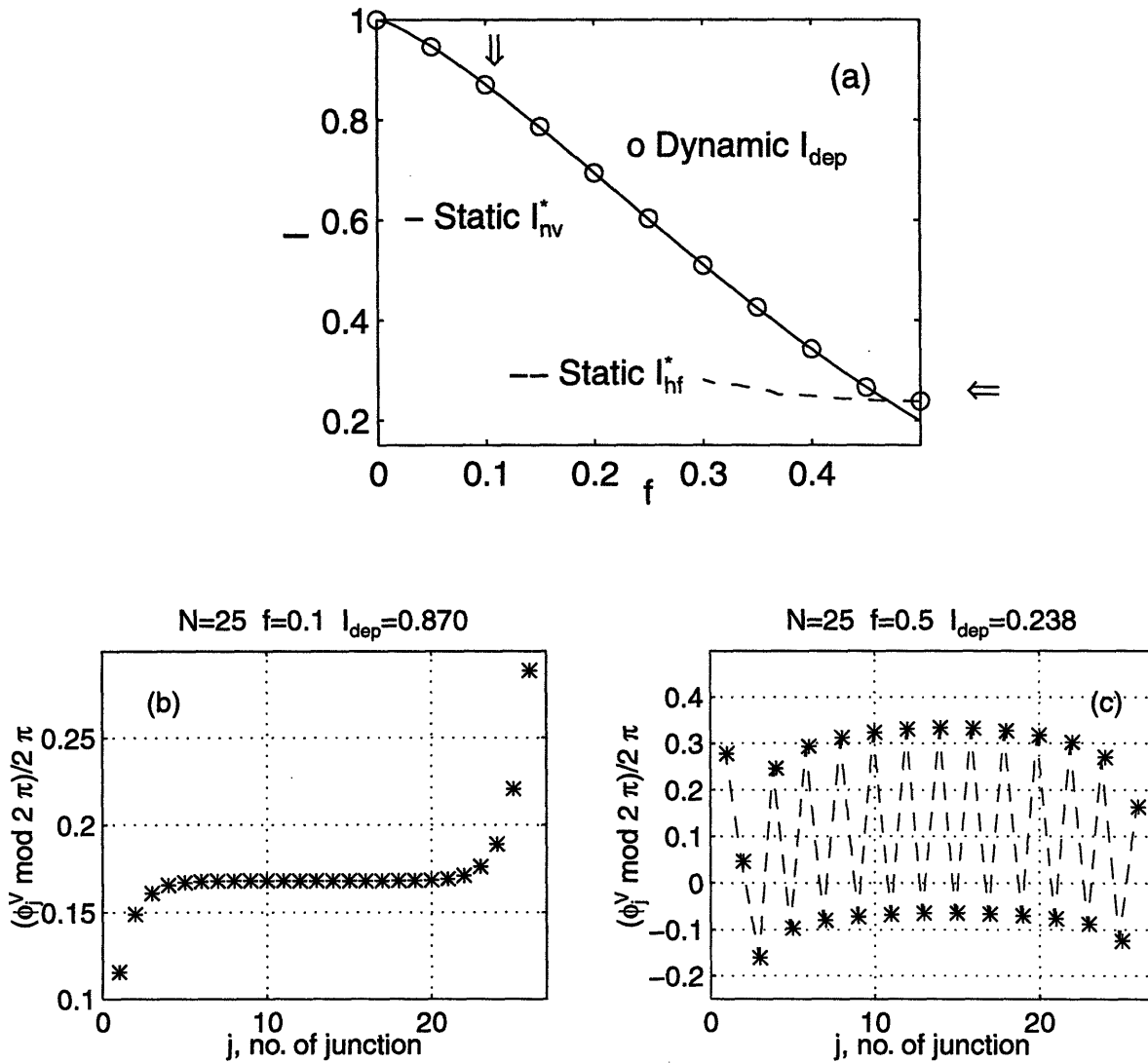


Figure 2-12: (a) Circles denote dynamical $I_{dep}(f)$ measured numerically by sweeping the current up from $I = 0$ for different values of f . Solid and dashed lines depict $I^*(f)$ for the no-vortex and half-filled solutions of the static system (2.62). The vertical phases of the configurations at $I^*(f)$ marked with the arrows are represented in (b) and (c). They correspond to the no-vortex and half-filled solutions respectively, as can be seen by comparing them with Figure 2-6. Therefore, we conclude that $I_{dep} = I^*$.

simulations -in which the current is swept up from zero. Moreover, the no-vortex configuration appears naturally for small f , while for $f \sim 1/2$ the half-filled is easily obtained from the solution of the augmented system. Energy arguments would have to be invoked to determine which of the possible solutions is the most stable for a given f . However, we are able to state that the depinning instability corresponds to the point where the Jacobian of the system is zero, and thus to a saddle-node bifurcation:

$$I_{dep} = I^*. \quad (2.63)$$

When f is not close to $1/2$, the no-vortex superconducting solution is the most stable and, thus, relevant for the depinning transition. At $f \rightarrow 1/2$, it is the half-filled solution ceasing to exist which causes the depinning. This constitutes a rigorous criterion for the depinning current. We emphasize that, by identifying this transition, we are able to predict numerically the depinning current —and the configuration of phases at depinning— for a given f , without “replicating” the experiment by performing a dynamical simulation.

Analytical approximations for I_{dep}

We proceed now towards a more simplified calculation for the depinning current $I_{dep}(f)$. As we stated above, both solutions (the no-vortex and the half-filled) have to be studied to explain the depinning behavior in different intervals of the frustration f .

At high field $f \rightarrow 1/2$, the half-filled is the relevant solution for the system. Thus, depinning occurs when this solution ceases to exist. We already obtained an analytical criterion (2.48) for the existence of the half-filled solution, which gives the depinning current as

$$I_{dep}(f \approx 1/2) = I_{hf}(f).$$

Although obtained without taking the boundaries into account, this expression is still a good approximation for the general case since edge effects are not important for the half-filled solution, as seen in Section 2.3.1. This is confirmed by the almost exact

agreement between the numerical I_{hf}^* depicted in Figure 2-12 and the analytical I_{hf} from (2.48) as shown in Figure 2-13. And we check that $I_{hf}(f = 1/2) = \sqrt{5} - 2 = 0.236$ is indeed very close to the observed $I_{dep}(f = 1/2) = 0.238$.

On the other hand, at small f we must investigate the no-vortex solution. Nothing similar to I_{hf} exists in this case, since the *approximate* no-vortex solution (2.32)-(2.38) exists for all $I < 1$, which is not the observed depinning current in the presence of magnetic field. Nevertheless, we attempt two simplifications: firstly, we obtain an augmented system, –equivalent to the one obtained for the full system (2.62)– for the approximate no-vortex solution, i.e. a *simplified* augmented system; secondly, we propose another mathematical condition based on a physically plausible criterion.

The augmented system (2.62) can be reduced using the simplified description provided by our approximation. Note that, for a given f , only three variables $\{P, Q, I\}$ – r is a function of I – suffice to describe the approximate solution (2.32), instead of the $2N + 1$ phases for the full solution. Thus, the simplified augmented system would be given by the equations (2.41)-(2.42) together with the condition that the determinant of the 2×2 Jacobian matrix be zero. This system can be further simplified since the equations are uncoupled and the only physically meaningful solution occurs when the eigenvalue from equation (2.41) becomes positive. Then, the augmented system from the approximate equation can be reduced to:

$$\mathcal{F}_1^\dagger = I + \sin\left(\pi f - \frac{P}{2}\left(1 - \frac{1}{r}\right)\right) - \sin(\arcsin I + P) = 0 \quad (2.64)$$

$$\mathcal{F}_2^\dagger = \frac{\partial \mathcal{F}_1^\dagger}{\partial P} = -\frac{r-1}{2r} \cos\left(\pi f - \frac{P}{2}\left(1 - \frac{1}{r}\right)\right) - \cos(\arcsin I + P) = 0 \quad (2.65)$$

where $r = r(f, I)$ is given by (2.39). This 2×2 system is solved numerically to obtain the approximate depinning current $I_{red}(f)$, such that

$$\vec{\mathcal{F}}^\dagger(P_{red}, I_{red}) = \mathbf{0} \quad (2.66)$$

which is the analogous expression to (2.62) for the reduced system from the approximate solution. The results of $I_{red}(f)$ are presented in Figure 2-13 with good overall

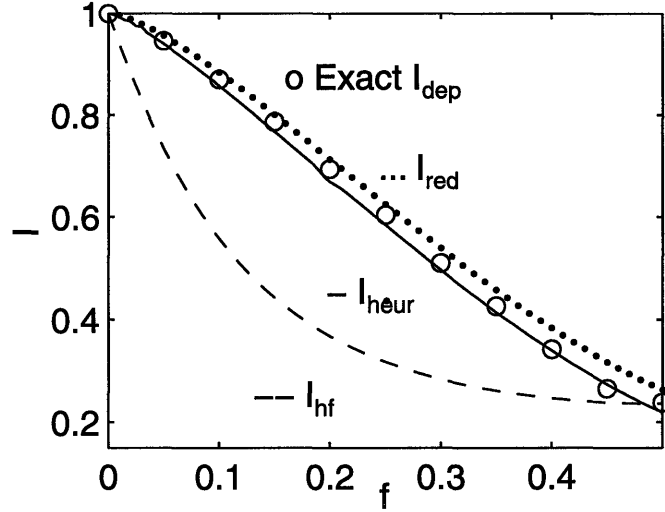


Figure 2-13: Analytical approximations for the depinning current. Circles represent the numerical $I_{dep}(f)$, as in Figure 2-12. The dashed line corresponds to the current I_{hf} at which the half-filled solution ceases to exist, as given in (2.48). Note it is equal to the numerical I^* for the half-filled solution (dashed line there also) in Figure 2-12. The other two graphs, I_{red} and I_{heur} , provide approximations to the point at which the no-vortex solution bifurcates (see text).

agreement. The predicted values get worse when f nears $1/2$, as expected from the fact that the approximate solution is less accurate in that limit –see Section 2.3.1.

We finish this section by proposing an alternative physical heuristic criterion which provides some insight on the mechanism of the depinning in the array in connection with the well understood depinning of the single junction. For a given I , the single junction has a superconducting solution $\phi = \arcsin I$ which ceases to exist at $I_{sj} = 1 \Rightarrow \phi_{sj} = \pi/2$ through a saddle-node bifurcation [78]. This is the solution for each of the junctions far from the edges in the no-vortex solution for the ladder (2.31); and that is precisely the stability criterion we found for that solution in Section 2.3.1, page 49. Although this is a very good approximation for the phases far from the boundaries, as we approach the ends, the correction A_j grows exponentially. Therefore, the maximum phase is that of the $N + 1$ vertical junction. We intuitively propose that the depinning of the complete array occurs when this end junction goes unstable, i.e.

$$\phi_{N+1}^V \dagger = \pi/2 \quad \Rightarrow \quad \arcsin I_{heur} + P(I_{heur}) = \pi/2, \quad (2.67)$$

This last expression is directly obtained from (2.38). Hence, equations (2.67) and (2.40) yield an implicit transcendental equation for $I_{heur}(f)$:

$$\arcsin(1 - I_{heur}) + \frac{r - 1}{2r} \arccos I_{heur} = \pi f \quad (2.68)$$

with $r = r(I_{heur})$ given by equations (2.39) and (2.36). The numerical solution of this equation for different values of f is also presented in Figure 2-13 and shows surprisingly good agreement with the exact results.

2.3.3 Other superconducting solutions with vortices

The analysis of the depinning transition developed in the preceding section is based on the particular solutions numerically observed in our dynamical simulations, which are always performed at zero temperature. In those, we used the initial condition that all phases and their derivatives are zero at $I = 0$. We have also checked numerically that the same results are unchanged when beginning from a random initial condition. This seems to support the idea that the observed solutions are indeed stable and have a large basin of attraction. However, a more methodical search would be needed to assert the generality of the observations, regarding the use of very special commensurate configurations as initial conditions in the simulations. In this section we follow this line of thought and investigate how our description of the depinning of the array changes when configurations which contain vortices are used as initial conditions in the dynamical simulations. We first summarize the observed numerical behavior and then go on to obtain some analytical results.

Numerical simulations with vortices

The question arises of what the behavior would be if the initial condition were another of the numerous static solutions of the system, specifically when vortices are present in the array. To address this issue we perform a series of simulations where solutions with vortices are taken as starting points for the simulations. In all of them, for a given $\{I, f\}$, we begin with an initial condition which includes a number of 2π -“jumps” in the vertical junctions and we observe its dynamical evolution under the governing equations of the system.

Let us begin with the relevant case in which *one* jump of 2π is introduced in the middle cell of the array

$$\phi_j^H(t=0) = 0, \quad \phi_j^V(t=0) = 2\pi \Theta \left[j - \text{ceil} \left(\frac{N+1}{2} \right) \right], \quad j = 1, \dots, N+1 \quad (2.69)$$

where $\Theta(x)$ is the Heaviside step function. This initial condition, not a solution of the system, is allowed to evolve under the dynamical equations (2.18), until it relaxes

into a solution for our ladder. In most cases, it generates a static configuration with a topological vortex in cell a of the array such that $n_a = 1$ and $n_j = 0, \forall j \neq a$, once all the phases have been reduced to the interval $[-\pi, \pi)$. This is the *one-vortex superconducting solution*. The behavior observed in the simulations with varying f and I is as follows:

- There is a minimum field f_c below which the one-vortex solution is not attainable from this initial condition and the system evolves to the no-vortex superconducting solution discussed in Section 2.3.1.
- When $f > f_c$ and I is small, the system relaxes into the one-vortex solution with a vortex in the middle of the array, $a = \text{ceil}(\frac{N+1}{2})$. As the current is increased, this remains unchanged as long as $I < I_{LAT}(f)$, at which point the vortex moves from the center cell to the left. Our notation is in analogy to the well known Lobb-Abraham-Tinkham critical current for *two-dimensional* junction arrays. Using static methods, they numerically calculated the critical current for which a vortex depins in the sinusoidal potential of an infinitely extended array [50]. This is equivalent to our I_{LAT} calculated from dynamical simulations when the vortex is placed far away from the edges in a long array.
- Only for a current $I \approx I_{LAT}$ does the vortex become pinned again between the center and the ends. Unless the sweeping of the current is done very slowly around I_{LAT} , the vortex moves all the way to the left edge as soon as $I > I_{LAT}$.
- There is a second critical current I_{edge} at which the vortex, located now at the left end, is expelled from the array. At that point the no-vortex solution is recovered again, and it remains stable until I_{dep} is reached, as discussed in Section 2.3.2.

This is summarized in Figure 2-14 where several snapshots of the system are represented at different values of I and f .

A simple picture serves us to interpret the snapshots depicted in Figure 2-14 in more physical terms. When a current I is injected in the array, the vortex located in

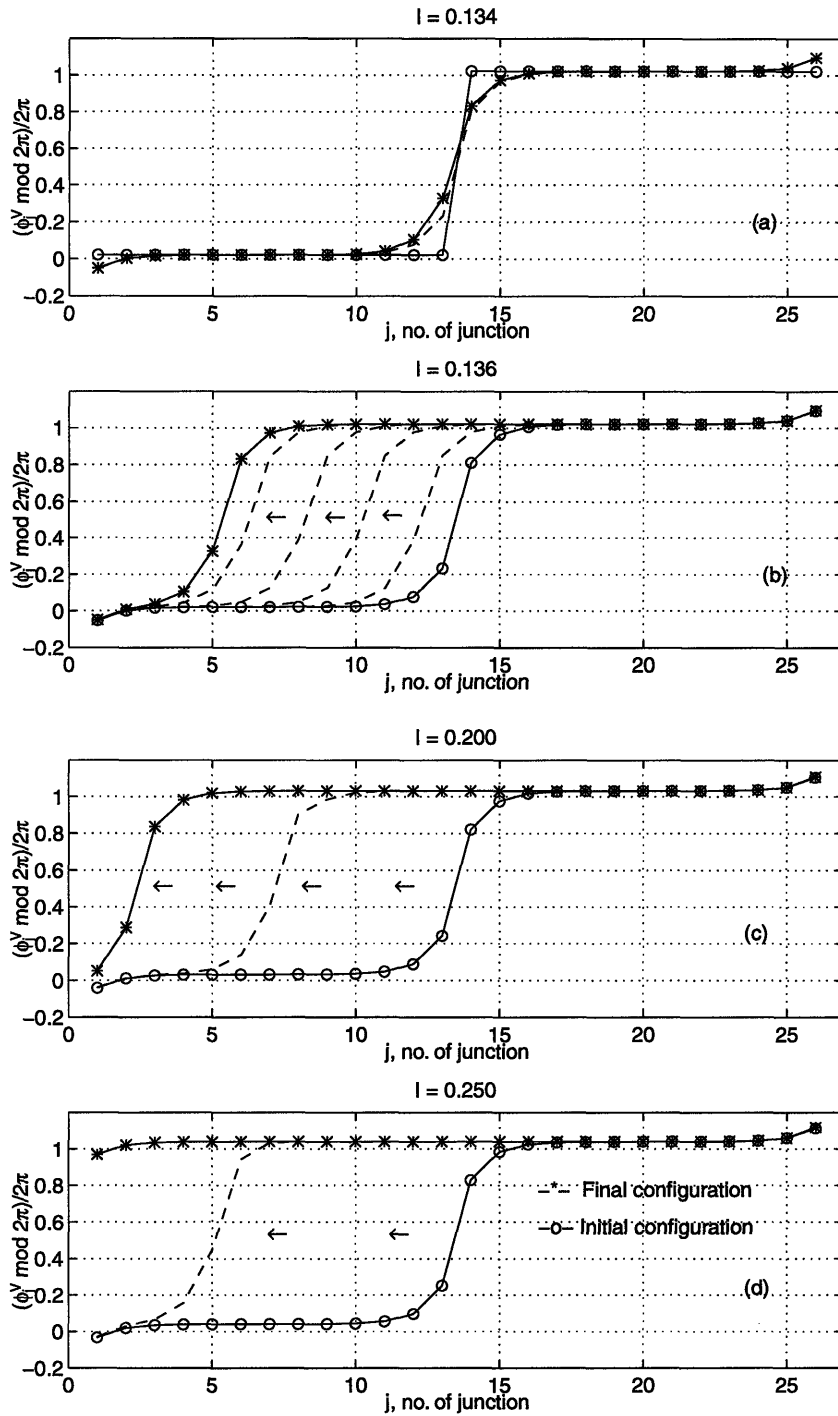


Figure 2-14: Snapshots of the one-vortex solution for a 25×1 ladder array with $\beta = 10$ and $f = 0.2$ and increasing I : (a) $I < I_{LAT}$ and the initial configuration with a 2π -jump relaxes to the one-vortex solution which is stationary; (b) $I \simeq I_{LAT}$ and the vortex begins to move slowly towards the left end; (c) when $I_{LAT} < I < I_{edge}$ the vortex moves until it gets pinned near the edge, where the potential is larger; (d) $I > I_{edge}$, and the vortex is expelled from the array. The final configuration in this case is the *no-vortex solution* described in Section 2.3.1.

the center of the array is subjected to an electromagnetic Lorentz-like force –a Magnus force in more precise fluid mechanical formulation– in the $-\hat{x}$ direction. However, the motion of the vortex does not occur in free space but across the array of Josephson junctions. It can be shown that this motion can be mapped onto the damped motion of a particle in a sinusoidal potential, where the maxima of the potential correspond to the vertical junctions and the minima are located in the middle of the cells [93]. Thus, an initial barrier has to be overcome to begin the motion, which explains the existence of the critical current I_{LAT} . This picture is at the heart of the static calculation of Lobb-Abraham-Tinkham [50]. Intuitively, the presence of the edges introduces an envelope, which decays exponentially from the edges, on the sinusoidal potential. Thus, the vortex can move from the center of the array, where the barrier between cells is smaller, and get trapped in deeper “wells” closer to the edges. In addition, as we saw in Section 2.3.1, the effect of the edges dies off quickly as we go into the array, which explains that the vortex moves almost immediately all the way to the boundary and remains there where the edge barrier is larger. When the critical current I_{edge} is reached, the vortex is expelled from the array and the no-vortex configuration is recovered, i.e. no new vortex enters the ladder.

The same physical picture emerges when we use a *multivortex initial condition*. In that case, Nf 2π -“jumps” are placed in the array and let evolve. For $I = 0$, the initial condition relaxes into a solution with Nf vortices in the array. As the current is increased, they begin to move towards the left end where they accumulate until they are expelled one by one at different currents. After the expulsion of the vortices, we recover once again the no-vortex solution. In other words, no train of vortices continues to propagate along the ladder; the depinning of the vortex, or series of vortices, is not the same as the depinning of the whole array when edges are present. This behavior is depicted in Figure 2-15 for $f = 0.2$ and $N = 25$, and, consequently, *five* vortices are introduced in the array. This sequence becomes fuzzier when the current is increased very suddenly or when many vortices are present in the array. This is expected since in those cases the interaction between vortices plays an important role.

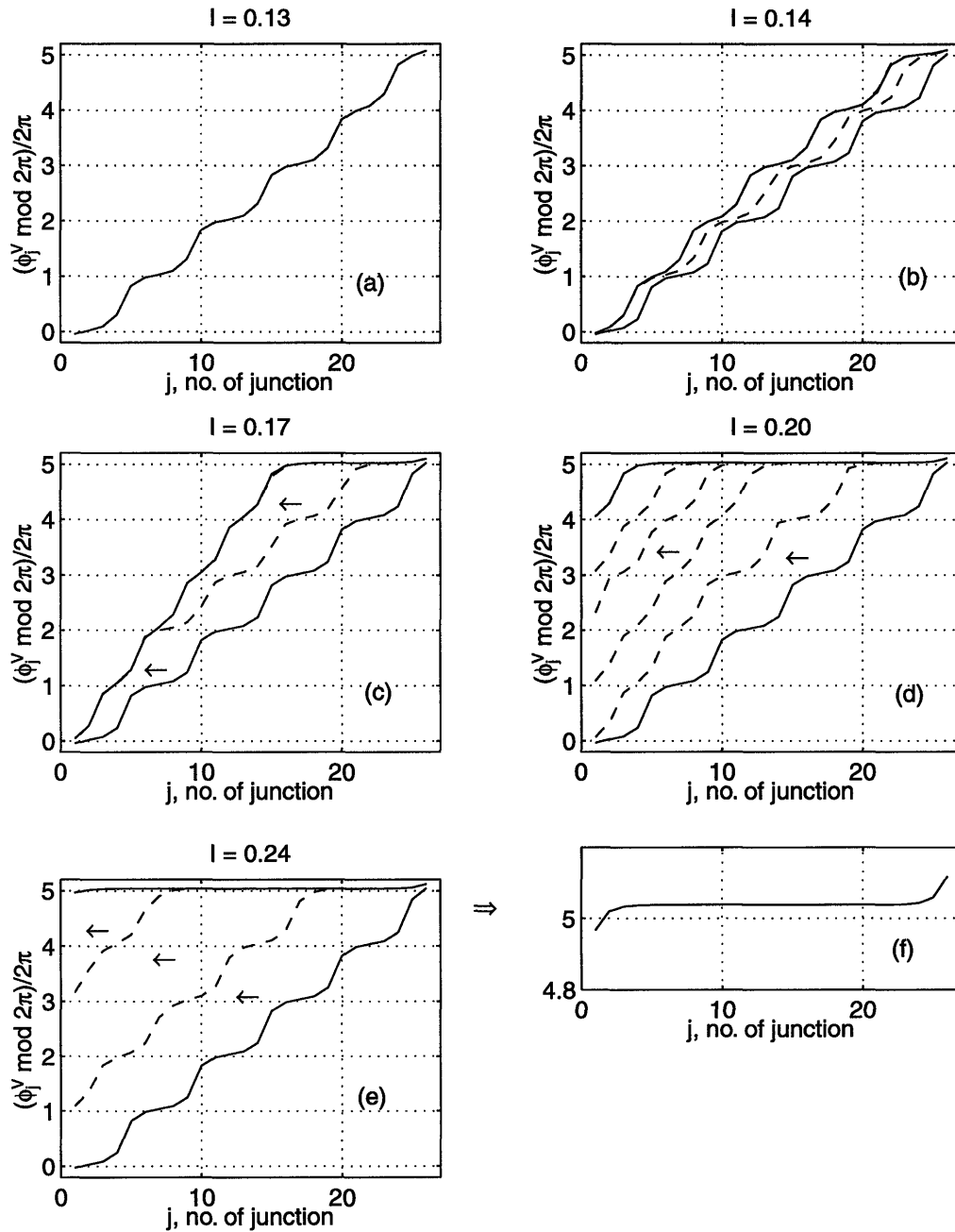


Figure 2-15: Snapshots of the time evolution of the multivortex initial condition for $N = 25$, $f = 0.2$, $\beta = 10$. In this case, we place $Nf = 5$ “jumps” of 2π in the array. The solid lines represent the initial and final configurations. The multivortex solution is statically stable for $I < I_{LAT}$, as in (a). When I_{LAT} is reached but $I < I_{edge}$, the vortices begin to move towards the left and become pinned close to the edge, as in (b) and (c). If the current is large enough to surmount the energy barrier from the edge, the vortices are expelled one by one as in (d) and (e). In the latter, all of them have been expelled and the final configuration is the no-vortex solution, as shown in (f), which is a blow-up of (e).

In summary, the numerical observations validate the assumption that even if initial conditions which include vortices in the array are used, the no-vortex and half-filled solutions are the relevant ones when the depinning transition is studied. The physical picture deduced from the simulations implies that, as the current is increased, the vortices are expelled from the array and, eventually, those limiting solutions are recovered. In describing the expulsion of the vortices from the array, we have focussed mainly on the case where one vortex is present in the array. There we identified two critical currents: one, I_{LAT} , at which the dynamical depinning of the single vortex occurs; the other, I_{edge} , at which the vortex is expelled from the edge. In the remainder of this section, we concentrate on giving an analytical approximation to the one vortex solution and describe this behavior.

Analytical approximation to the one-vortex solution

We obtain now an analytical approximation to the one-vortex solution using similar techniques to the ones developed in Section 2.3.1. There, we calculated the effect of the edges as corrections to basic solutions. Here, we do the same to include the effect of the presence of a vortex located in cell a of the array. It is readily observable from Figure 2-14 (a) that the solution far from the edges and from cell a , is still the no-vortex superconducting solution, if all the phases are reduced to the interval $[-\pi, \pi)$. Hence, assume a solution of the system (2.22)-(2.23) of the form:

$$\begin{cases} \phi_j^{V\dagger} = \phi^{V\dagger} + A_j, & j = 1, \dots, N+1 \\ \phi_j^{H\dagger} = \phi^{H\dagger} - B_j, & j = 1, \dots, N \end{cases} \quad (2.70)$$

where

$$\phi^{V\dagger} = \arcsin I, \quad \phi^{H\dagger} = \pi f$$

and A_j, B_j are corrections which result both from the presence of the edges and of the vortex in the array, i.e. $n_a = 1$. Far from the ends and from the vortex center, the corrections are small and, hence, the equations can be linearized to yield the same result previously given in equations (2.36)-(2.39). Following the exact same

procedure spelled in Section 2.3.1, we obtain the following approximate solution for the configuration with one vortex in cell a :

$$A_j = \begin{cases} Pr^{j-a} + Qr^{1-j}, & j \leq a \\ P'r^{j-(N+1)} + Q'r^{a+1-j}, & j > a \end{cases} \quad (2.71)$$

$$B_j = \frac{A_{j+1} - A_j}{2}, \quad j \neq a \quad (2.72)$$

and

$$r = \alpha + \sqrt{\alpha^2 - 1}, \quad \alpha = 1 + \frac{\sqrt{1 - I^2}}{\cos \pi f} \quad (2.73)$$

as given by (2.39) and (2.36).

This solution, depicted in Figure 2-16, has two distinct regions, $j \leq a$ and $j \geq a+1$. Inside each of them, the solution is the no-vortex superconducting solution in the presence of edges. The presence of the vortex in cell a , effectively introduces two new “edges”, at a and $a+1$, which produce exponentially decaying corrections. However, the conditions at those two points are closely connected by the fact that a topological vortex is present at cell a rendering the following fluxoid quantization equation

$$A_a - A_{a+1} + 2B_a = 2\pi, \quad (2.74)$$

which is the matching condition for the two regions of the solution.

There are five unknown constants P, Q, P', Q', B_a in our solution. First, we eliminate B_a by using the fluxoid quantization condition at cell a (2.74) to obtain

$$B_a = \pi + \frac{P'r^{a-N} + Q' - P - Qr^{1-a}}{2}. \quad (2.75)$$

The other four constants can be determined from the boundary conditions

$$I = \sin \left(\pi f - \frac{r-1}{2r} (Pr^{1-(a-1)} - Q) \right) + \sin(\arcsin I + Pr^{1-a} + Q) \quad (2.76)$$

$$I + \sin \left(\pi f - \frac{r-1}{2r} (P - Qr^{1-(a-1)}) \right) =$$

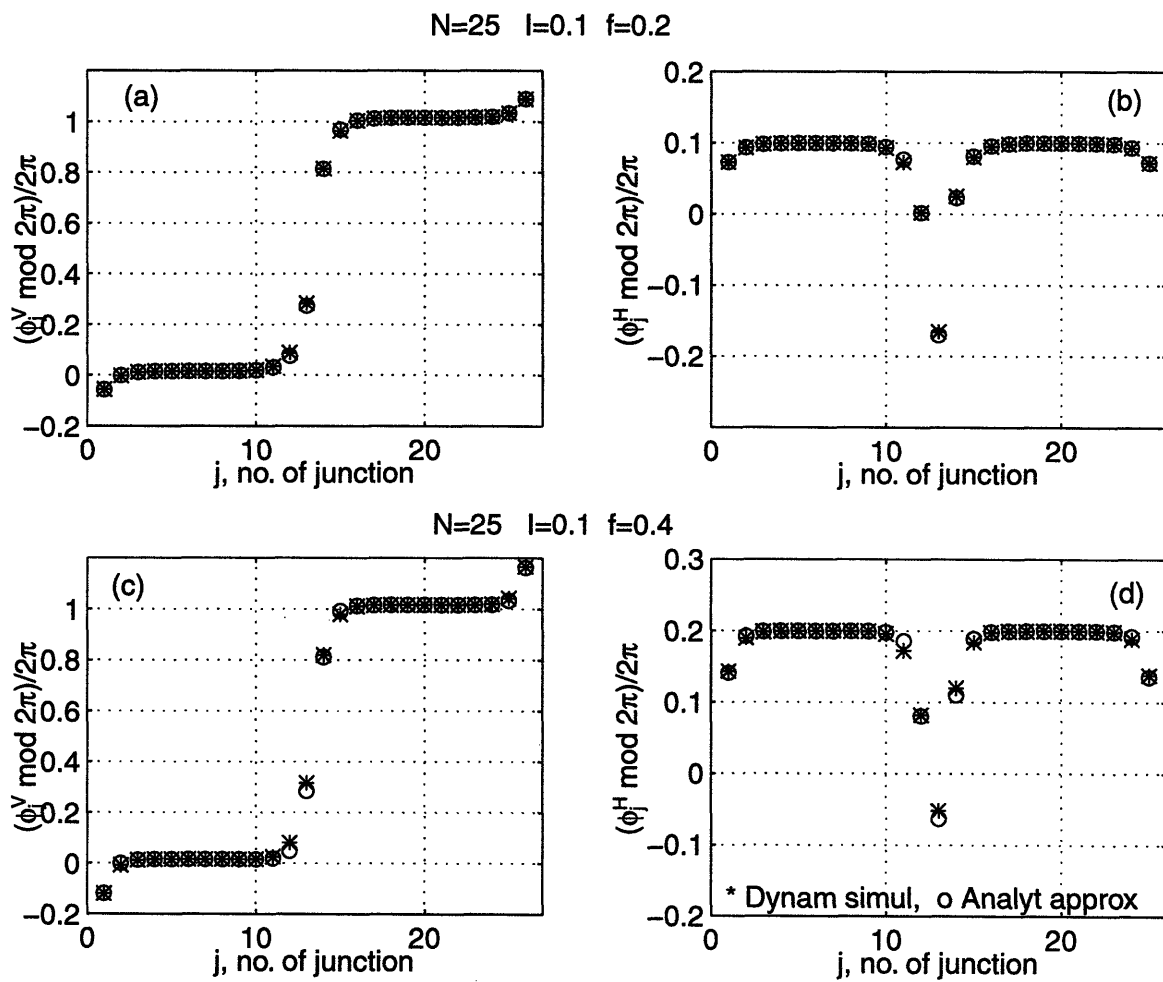


Figure 2-16: Two examples of a one-vortex solution for the 25×1 ladder with $I = 0$ and $f = 0.2, 0.4$. We compare for each of them the numerical configuration obtained from the dynamical simulations (*) with the analytical approximation (o) as given by (2.70).

$$\sin(\arcsin I + P + Qr^{1-a}) - \sin\left(\pi f - \frac{P'r^{a-N} + Q' - P - Qr^{1-a}}{2}\right) \quad (2.77)$$

$$I - \sin\left(\pi f - \frac{P'r^{a-N} + Q' - P - Qr^{1-a}}{2}\right) = \sin(\arcsin I + Q' + P'r^{a-N}) + \sin\left(\pi f - \frac{r-1}{2r}(P'r^{(a+1)-N} - Q')\right) \quad (2.78)$$

$$I + \sin\left(\pi f - \frac{r-1}{2r}(P' - Q'r^{(a+1)-N})\right) = \sin(\arcsin I + P' + Q'r^{a-N}) \quad (2.79)$$

which correspond to current conservation (2.22) at nodes 1, a , $a+1$ and $N+1$ respectively.

We solve numerically the above system for P, Q, P', Q' to complete the approximation for the superconducting configuration with one vortex at cell a for given current I and magnetic field f . We compare in Figure 2-16 this approximation with the solutions observed numerically when letting the system dynamically relax from an initial condition given by a 2π step function at cell a . The agreement is excellent, specially for small f . The exponential decay both from the edges and from $a, a+1$ is explicitly depicted for different values of f and I in Figure 2-17, where the predicted value of the characteristic penetration length is also checked.

Instability of the one-vortex solutions

We turn now our attention to the instability of this solution. We argued at the beginning of this section that the electromagnetic force applied on the vortex is linearly dependent on I . When the critical current I_{LAT} is reached, the force is large enough to produce the motion of the vortex in the sinusoidal potential which characterizes the junction array. In the absence of edges, this corresponds exactly to the current calculated by Lobb, Abraham & Tinkham [50] for two-dimensional arrays. We discuss now that this critical current corresponds to the point at which the stability of the one-vortex solution changes. To verify this, we follow the same procedure as for the no-vortex solution in Section 2.3.2, pages 62-66. In short: we look for the current I^\diamond

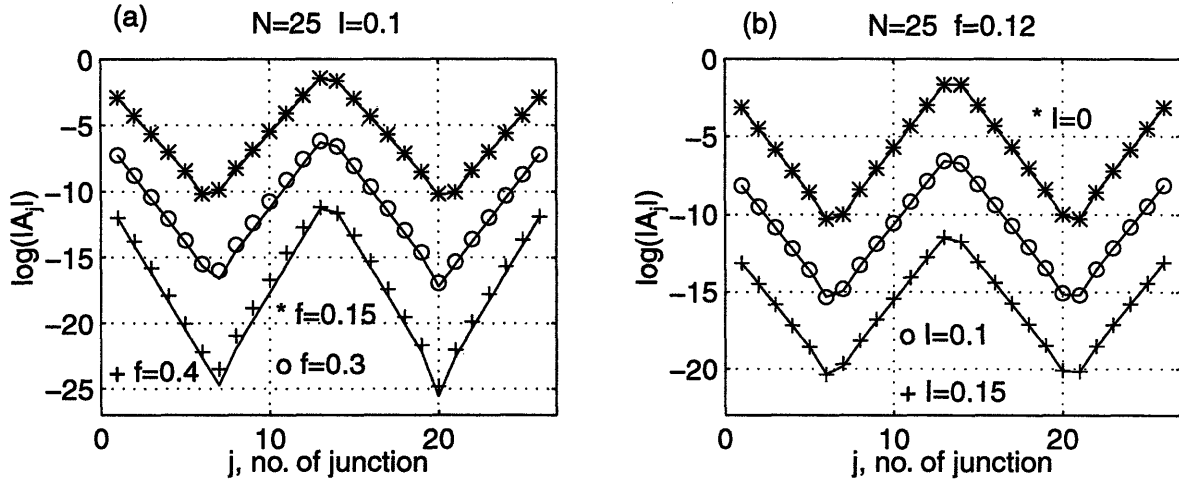


Figure 2-17: Exponential decay of the correction A_j of the one vortex solution from the edges and the cell with vortex. The solid lines are the predicted values, given by (2.71) with slope $\sim \log r$ while the symbols are obtained from the numerical simulations. We study the dependence of the penetration depth with: (a) f , (b) I . In both (a) and (b), the different graphs have been offset for clarity.

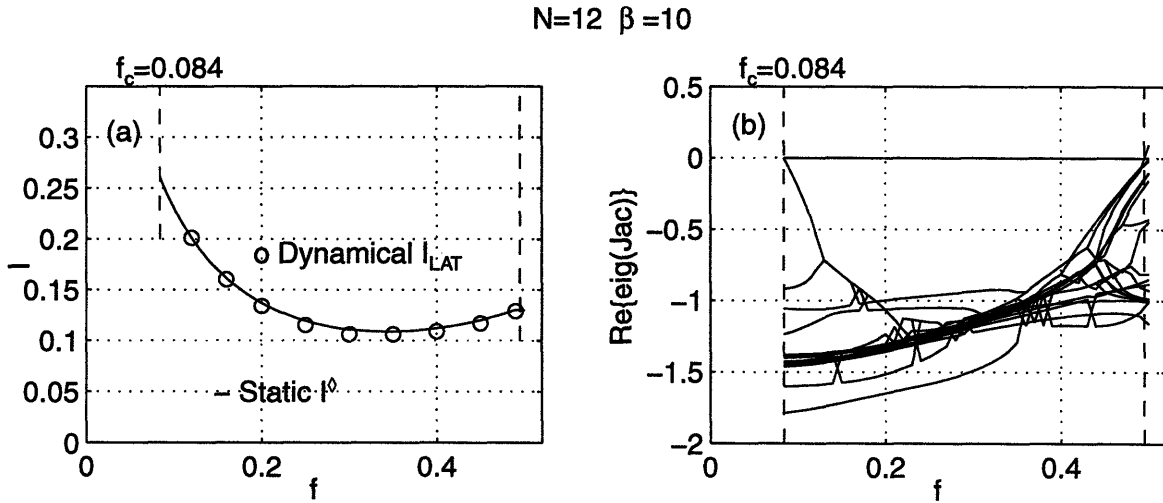


Figure 2-18: Depinning of a vortex located at the center of a 12×1 ladder array: (a) Comparison of $I_{LAT}(f)$, calculated dynamically from numerical simulations, and $I^0(f)$ obtained from the static solution of the system (2.81). We conclude that $I_{LAT} = I^0$. (b) Real part of the eigenvalues of the Jacobian of the system (2.60) for the one-vortex solution in the center of the array at I^0 . For $f_c < f < 0.49$, the solution is linearly stable under the addition of a small perturbation if $I < I^0$. For $f < f_c \simeq 0.084$, this solution is linearly unstable since one of the eigenvalues has a positive real part.

at which the one-vortex solution of the system fulfills the condition

$$\mathcal{F}_{2N+2} = \max \{ \Re [\text{eig}(J_{i,j})] \} = 0. \quad (2.80)$$

As in (2.62), we solve for the augmented system

$$\vec{\mathcal{F}}(\vec{x}, I^\diamond) = \mathbf{0}. \quad (2.81)$$

This means we obtain the configuration where the solution goes from being linearly stable to linearly unstable, since all the eigenvalues of the Jacobian matrix have negative real parts except for one which is zero, as seen in Figure 2-18 (b). In Figure 2-18 (a) we compare with excellent agreement the calculation of $I^\diamond(f)$ from the static augmented system (2.81) with the $I_{LAT}(f)$ obtained from numerical simulations where a vortex is placed in the middle of the array and the current increased until the vortex moves. Therefore, we conclude that

$$I_{LAT} = I^\diamond,$$

i.e., we find a rigorous criterion for the depinning of the single vortex as the current at which the single vortex solution goes unstable. In fact, the only difference with the numerical procedure used in Section 2.3.2 to identify the depinning transition as a saddle-node bifurcation (2.63) is the use of a different initial condition when numerically solving the system (2.81). As we did there, we emphasize that the calculation of I^\diamond is static and thus, we circumvent the mimicking of the experiment through the sweeping of the current.

Moreover, we clarify the existence of a *critical field* f_c below which the one-vortex solution is not attainable. Indeed, for values of the field $f < f_c$ the one-vortex solution is linearly unstable for any I , i.e. there is always one eigenvalue of the Jacobian matrix with a positive real part, as shown in Figure 2-18 (b). Unless the array is very small, so that the effect of the edges is felt in the center, this mathematical condition is met at $f_c = 0.084$, independently of the length of the array. However,

this minimum condition is only found when the sweeping of the current is done at very small increments. In fact, when dynamical simulations are used, the one-vortex configuration is only seen to be dynamically stable for values of f larger than ~ 0.12 .

Let us state the differences between our I_{LAT} and the calculation of Lobb-Abraham-Tinkham [50]. As explained above, theirs is a static estimation of the energy barrier E_b in infinitely extended two-dimensional junction arrays. The barrier is calculated as the difference of energy between two configurations in which the vortex lies at the center of the cell (low energy solution), or at a junction (high energy configuration). By minimising the energy of assumed $\arctan(y/x)$ solutions for both configurations, E_b is obtained, and, so is the critical current, which is one half of E_b . In our case, we calculate the dynamic current at which the one-vortex configuration in the ladder becomes unstable. The most fundamental difference lies in the distinct solutions associated with the vortex in the two-dimensional and the quasi-one-dimensional problems. Moreover, their static calculation does not include the effects of the field f , or the injected current I , on the configurations. These effects are taken into account in our case. In Figure 2-18 we observe that the vortex depinning current is higher for lower f . This is explained well in terms of the corrections that edges introduce on the basic no-vortex superconducting solution: a smaller f implies a smaller correction from the vortex on the rest of the array (see Figure 2-16) and, thus, a higher critical current. Within this physical picture, the depinning of the vortex is equivalent to study when the flux of the vortex enters the left side of the array.

One last result can be obtained from our approximation for the one-vortex configurations: the current I_{edge} , at which the vortex is expelled from the array, must correspond to the value of I at which the one-vortex solution with the vortex at the end of the array becomes unstable. Therefore, we repeat the same procedure as above for this configuration to characterize I_{edge} . The same conclusions are reached: the expulsion current observed in the dynamical simulations corresponds to the value of I where the configuration with the vortex at the leftmost cell becomes unstable, i.e. the maximum of the real parts of the eigenvalues of the Jacobian matrix is zero. Critical fields are found as well for this solution, below and above which this configuration is

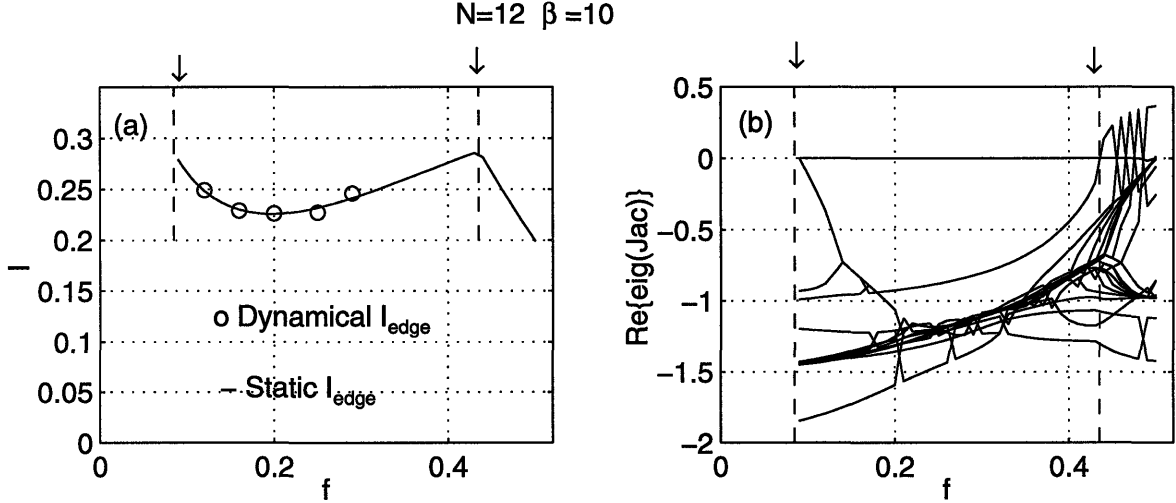


Figure 2-19: Expulsion of the single vortex at the edge of a 12×1 array: (a) Comparison of $I_{edge}(f)$ from dynamical simulations (o) and from a static calculation (-). (b) Real part of the eigenvalues of the Jacobian of the system (2.60) for the one-vortex solution with the vortex near the edge of the array at I_{edge} . Outside of the interval of the field indicated by the arrows, $0.09 \leq f \leq 0.43$, this solution becomes unstable for all I .

linearly unstable. These calculations, analogous to those performed for the depinning of one vortex at the middle of the array, are summarized in Figure 2-19.

Comparison with the continuum approximation

In the paragraphs above, we have pointed out the distinguishing features of our quasi-one-dimensional vortex solution and the full two-dimensional one. In this last part of the subsection we connect our results with the classical kink solution of the one-dimensional sine-Gordon equation. This continuum solution, which approximates well the vortex configurations observed in $1 - D$ parallel arrays, is not appropriate for the one-vortex configuration in the ladder. This highlights the importance of the presence of the horizontal junctions which introduce an implicit coupling between the vertical junctions, via the fluxoid quantization condition. The observed discrepancy implies that this coupling is not purely inductive, and the ladder cannot be easily reduced to a one-dimensional parallel array with an effective inductance.

The time independent sine-Gordon equation with no forcing [18]

$$\phi_{xx} - \frac{1}{\lambda^2} \sin \phi = 0 \quad (2.82)$$

has the well known kink solution

$$\phi(x) = 4 \arctan \left[\exp \left(\frac{x - x_0}{\lambda_{sg}} \right) \right]. \quad (2.83)$$

The solution corresponds to a 2π -“jump” which is parametrized by x_0 – the center of the kink around which the solution is symmetric– and λ_{sg} – its width, which represents the characteristic length over which the jump from 0 to 2π is produced. This solution is only exact when the domain of x extends to infinity.

Under certain approximations, the sine-Gordon equation describes our system. Consider the time-independent equations for the ladder (2.22)-(2.23) when $I = 0$ and in the limit of small *horizontal* phases $\phi_j^H \ll 1$. Then the governing equations become

$$\phi_{j-1}^H = \phi_j^H + \sin \phi_j^V \quad (2.84)$$

$$\phi_j^H = \pi f + \frac{\phi_j^V - \phi_{j+1}^V}{2}. \quad (2.85)$$

Combining both, it is immediate to obtain

$$\phi_{j+1}^V - 2\phi_j^V + \phi_{j-1}^V = 2 \sin \phi_j^V,$$

which, in the continuum limit, results in

$$\phi_{xx}^V - 2 \sin \phi^V = 0 \quad (2.86)$$

with the cell size taken as unity. In this simple way, we arrive at the standard approximation of the kink in the vertical junctions of the ladder with an arctan functional form and penetration depth $\lambda_{sg} = 1/\sqrt{2}$. This is valid when the phases in the horizontal junctions are small. We now show how our approximation compares

to this formulation.

To this end, we particularize the one-vortex solution (2.70) far from the edges, i.e. $1 \ll a \ll N + 1$, for $I = 0$. The boundary conditions (2.76)-(2.79) become then

$$\pi f + \frac{r-1}{2r}Q = -Q \quad (2.87)$$

$$\sin\left(\pi f - \frac{r-1}{2r}P\right) = \sin P - \sin\left(\pi f - \frac{Q' - P}{2}\right) \quad (2.88)$$

$$-\sin\left(\pi f - \frac{Q' - P}{2}\right) = \sin Q' + \sin\left(\pi f + \frac{r-1}{2r}Q'\right) \quad (2.89)$$

$$\pi f - \frac{r-1}{2r}P' = P', \quad (2.90)$$

from which the solution

$$Q = -P', \quad P = -Q'$$

is readily obtained. In conclusion, the vertical phases for the particular approximate solution under consideration are:

$$\phi_j^{V\dagger} = A_j = \begin{cases} Pr^{j-a} + Qr^{1-j}, & j \leq a \\ -(Pr^{a+1-j} + Qr^{j-(N+1)}), & j > a \end{cases} \quad (2.91)$$

with the constants P and Q given by

$$Q = -\frac{2r}{3r-1}\pi f \quad (2.92)$$

$$\sin P = \sin\left(\pi f - \frac{r-1}{2r}P\right) + \sin(\pi f + P) \quad (2.93)$$

and r is given by (2.73).

Since the arctan approximation is infinitely extended and no edges can be considered, we concentrate on the region far from the edges, around the cell where the kink

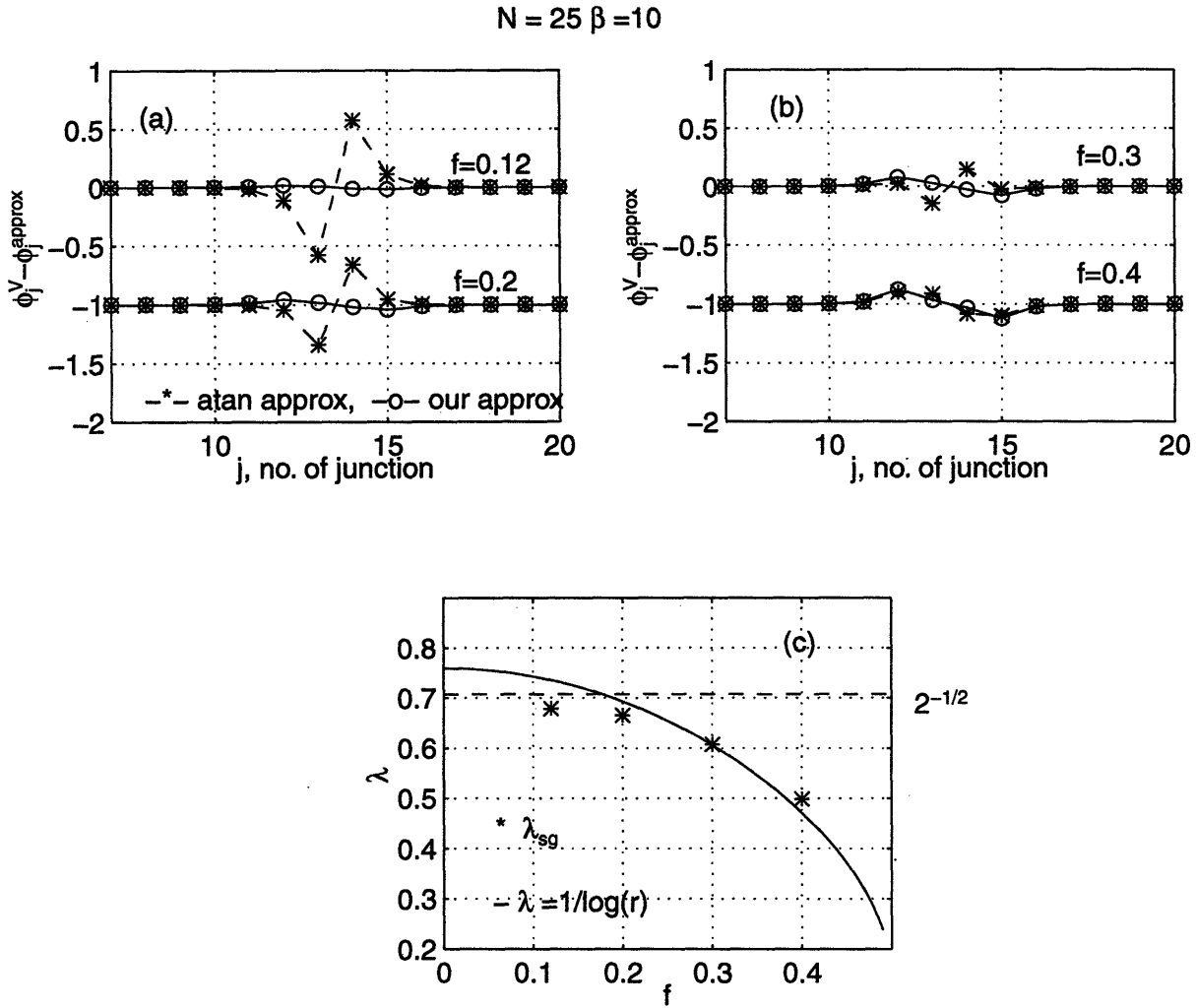


Figure 2-20: (a) and (b): Error of our approximation (\circ) and the standard sine-Gordon arctan approximation ($*$) for varying magnetic field $f = 0.12, 0.2, 0.3, 0.4$. Graphs for different f are offset for clarity. The arctan approximation is calculated with a linear fit of $\ln [\tan(\phi_j^V/4)]$ vs. j . The λ_{sg} ($*$) from this fit is plotted in (c) together with the characteristic length of our approximation $\lambda = 1/\ln r$ (solid line).

is located. Then the expression is further simplified to

$$\phi_j^V = \begin{cases} P \exp[(j - a)/\lambda], & j \leq a \\ -P \exp[(a + 1 - j)/\lambda], & j > a \end{cases} \quad (2.94)$$

which has the same properties as the arctan approximation: odd with respect to $x_0 = a + 1/2$ and with a characteristic length $\lambda(I, f) = 1/\ln r$, which is the same penetration depth which measures the extent of the perturbations from the edges to die away, as given in (2.39).

However, both their functional form and the interpretation of their parameters are different. In Figure 2-20 (a) and (b), both approximations are compared with the numerically observed one-vortex configurations. We conclude that ours is consistently better than the sine-Gordon approximation, especially at small fields, i.e. the arctan approximation gets worse as $f \rightarrow 0$. As f increases, the characteristic length λ of the vortex decreases and both approximations converge. This can be observed also in Figure 2-20(c) where the calculated λ from both approximations is represented. Again, at small f the sine-Gordon and our double-exponential approximations differ: as $f \rightarrow 0$, $\lambda_{sg} \rightarrow 1/\sqrt{2}$ while our $\lambda(0, 0) = 1/\ln r(0, 0) = 1/\ln(2 + \sqrt{3})$. Therefore, it is at low f that the difference between the two approximations becomes more important.

In summary, the sine-Gordon approximation presents the following contradiction: it gets worse as $f \rightarrow 0$, when, at the same time, its validity is based on the assumption that $\phi^H \rightarrow 0$ which is fulfilled when $f \rightarrow 0$. However, precisely in that limit, the characteristic length of the vortex grows and the discreteness of the array renders the approximation invalid. This underscores the inappropriateness of the arctan solution to describe ladder arrays with no inductances. Thus, the description of the ladder as a one-dimensional parallel array where the presence of the horizontal junctions is approximated as an effective inductance constitutes an oversimplification.

2.3.4 Summary and discussion

We have obtained in this section analytical approximations for the relevant superconducting solutions of the ladder array: the no-vortex, half-filled and one-vortex configurations. A common feature to all of them is the fact that any correction imposed on the basic solution decays exponentially in space with a calculated characteristic length dependent on I and f . The mentioned correction can be due to the presence of the edges, or of topological vortices in the array. In both cases, the effect of the perturbations is highly concentrated in space and their behavior can be well represented in terms of a local analysis. For instance, the depinning current of the array can be well explained by the study of the rightmost cell, and the depinning of the single vortex by the analysis of the cell where it is located. This explains why, besides the obvious independence from the purely dynamical parameter β , the depinning observables are also independent of the length of the array N . In addition, the dependence on f is quantitatively explained within our framework.

Finally, we summarize in Figure 2-21 the stability of the superconducting solutions analyzed in this section (no-vortex, half-filled, one-vortex) by representing the critical currents at which each of them becomes dynamically unstable. In the absence of a singular vortex in the array, the no-vortex or half-filled solutions remain stable until I_{dep} (solid line in the figure) is reached, at which the array ceases to be superconducting. If vortices are initially present in the array, the conclusions do not change. The discontinuous lines represent critical currents associated with the one-vortex solution: $I_{LAT}(- -)$ is the current at which a vortex in the center of the array depins, while $I_{edge}(-.)$ shows the current at which the vortex is expelled from the edge. When this current is reached, the no-vortex solution is recovered. Moreover, the one-vortex solution is always unstable for small fields. When the field is not too large, similar critical currents appear for multivortex solutions at which vortices begin to move and get expelled from the array. Thus, away from the limit $f \approx 1/2$, I_{dep} is always the observable depinning current and the depinning of the array is edge-dominated.

This does not contradict the conclusions of Kardar [40, 41]. We note first that

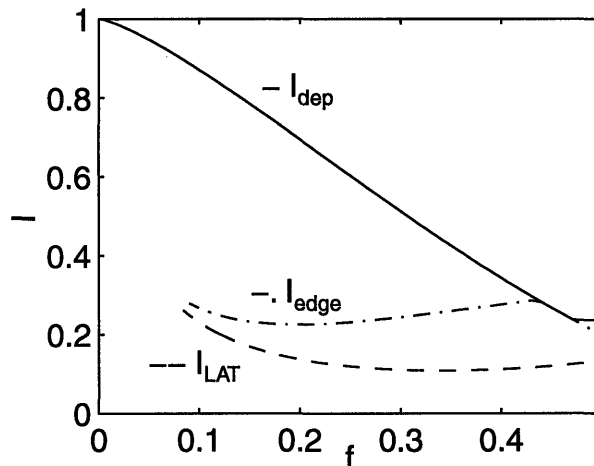


Figure 2-21: Summary of the critical currents for the analyzed superconducting solutions of the array: $I_{dep}(-)$ is the current at which the no-vortex solution (at $f < 0.45$) and the half-filled solution (for $0.45 < f < 0.5$) become unstable. $I_{LAT}(- -)$ is the dynamical Lobb-Abraham-Tinkham current which measures when the one-vortex superconducting solution becomes unstable and, thus, a vortex in the center of the array depins. Finally, $I_{edge}(-.)$ is the current at which the vortex is expelled from the edge and the no-vortex configuration is recovered.

those calculations are carried out for $I = 0$ with a brief discussion of the effects of a small current in the *parallel* direction. Thus, the extension of his results to the case with a finite I in the perpendicular direction is not immediate. Nevertheless he found that, for $I = 0$, the no-vortex solution is *thermodynamically* stable for $f < f_{c1} \simeq 2\sqrt{2}/\pi^2 = 0.287$, which we have checked numerically to good agreement. Our results indicate that although the one-vortex solution is not the ground state of the system, it is *dynamically* stable until I_{LAT} is reached. That is: for $f_c < f < f_{c1}$ the vortex configurations are metastable solutions of the system.

We conclude this analysis by comparing our independent results to the very recent numerical work on ladders by Hwang, Ryu and Stroud [34]. Among other simulation results, they present numerical observations of the depinning (critical) current for: a circular ladder with perpendicular injection, and for an open-ended ladder with parallel injection of current. In both cases overdamped junctions ($\beta = 0$) are considered. The fact that we used underdamped units with $\beta = 10$ does not modify the depinning predictions, as stated above. Their numerical findings are in agreement with

our predictions. Although we have not considered the ring geometry in our analysis, it is readily understood that the calculated depinning current of the vortex I_{LAT} is equivalent to the depinning current for a *circular* ladder array. Indeed, their values for the $I_{c\perp}$ of an isotropic array are very similar to the currents at which the one-vortex configuration becomes dynamically unstable, I_{LAT} . The small discrepancy observed as $f \rightarrow 1/2$ can be due to the relative importance of the edge effects in that limit. Moreover, they find a numerical value of the field, $f_{c1\perp}^* \simeq 0.12$ for which the depinning current is $I_{c\perp} = 1$ and they find exclusion of field. As stated above, this is the value below which the one-vortex configuration becomes dynamically unstable *for all* values of the current. Thus, the no-vortex solution (which in the absence of edges has a depinning current of unity) is the preferred superconducting solution of the system. In a more technical note, we too found this field to be 0.12 in our dynamical simulations. However, a more careful static calculation with the jacobian condition yielded the value 0.084 for this critical field. We can imagine two possible explanations for this difference: the numerical instability of the dynamical simulations which make it difficult to follow the solution all the way to its critical value; or the possibility that for small f the mechanism for the bifurcation of the one-vortex solution is no longer a saddle-node bifurcation and the instability appear through a different mechanism. Some research is needed to clarify this point.

The open-ended array they choose to study is the ladder with parallel current injection. No direct comparison can be established at this moment, although preliminary calculations indicate that the solution for this configuration would present the same features as for the open-ended array with perpendicular current injection, which has been extensively studied in this chapter. Hence, the depinning current $I_{c\parallel}(f)$ could be explained in terms of an edge-dominated depinning for the ladder as the f dependence seems to suggest. We note also that $I_{c\parallel}(f)$ for $f < f_{c1}$ observed in their simulations, seems to be accounted for with the analytical result of Benedict [5]

$$I = I_c \cos \pi f \sin \delta_c$$

where

$$\cos \delta_c = -\frac{1}{4} \left[\cos \pi f - \sqrt{1 + 15 \sin^2 \pi f} \right].$$

Future directions for this work will include a detailed analysis of ladder arrays in the ring configuration and open-ended ladders with parallel injection along the same lines developed here. Moreover, the obtained approximate solutions can be used further to carry out energy calculations and establish thermodynamic stability criteria which have been left out of this thesis. Finally, the inclusion of inductances in the problem would constitute a major step towards comparison with a broader range of experiments and to assess the influence of self-fields on the observables.

2.4 Whirling solution

In this section, we study the solution for the ladder array at large I , i.e the ohmic branch, and the critical current I_{inst} at which it becomes unstable in the return path of the $I - V$ characteristics. In the first subsection, we present results of the numerical integration of the equations for this regime and a description of the observed spatio-temporal solution. From these observations we deduce an approximate solution for the system, based on the “whirling” solution for the single junction. Finally, we take into account the presence of edges in our open ended array. In the second subsection, we study the mechanism for the instability of the ohmic branch by performing the linear stability analysis of the approximate whirling solution. In the third, we focus on the particular case $f = 0$ and some new solutions which appear as steps on the return path. They will be shown to correspond to a set of subharmonic whirling solutions for which the horizontal junctions oscillate non negligibly and can be related to an alternative description of the repinning instability. The appearance of such solutions illustrates the importance of the presence of the horizontal junctions and of the implicit coupling they introduce.

2.4.1 Observed and approximate whirling solutions

As we saw in Section 2.2.2, the behavior of the system at large values of I is characterized by a linear dependence of the dc average voltage $\langle V \rangle$ with I , in what we called the ohmic branch. This is always so, independently of the other parameters of the system $\{\beta, N, f\}$. The main feature of the spatio-temporal solution associated with this branch is the linear dependence of the vertical phases both with time and with their position in the array (Figure 2-22 (a) and (b)). They also have a small superimposed modulation as evidenced when the linear dependence is subtracted (Figure 2-22 (c) and (d)). Moreover, the horizontal phases oscillate around zero with a small amplitude. In summary, the vertical pendula (junctions) “whirl” quasi-harmonically, with almost constant frequency, while the horizontal junctions describe small librations. Hence the name *whirling mode* to describe this solution.

Whirling mode: $N=25, \beta=10, f=0.2, I=1.05$

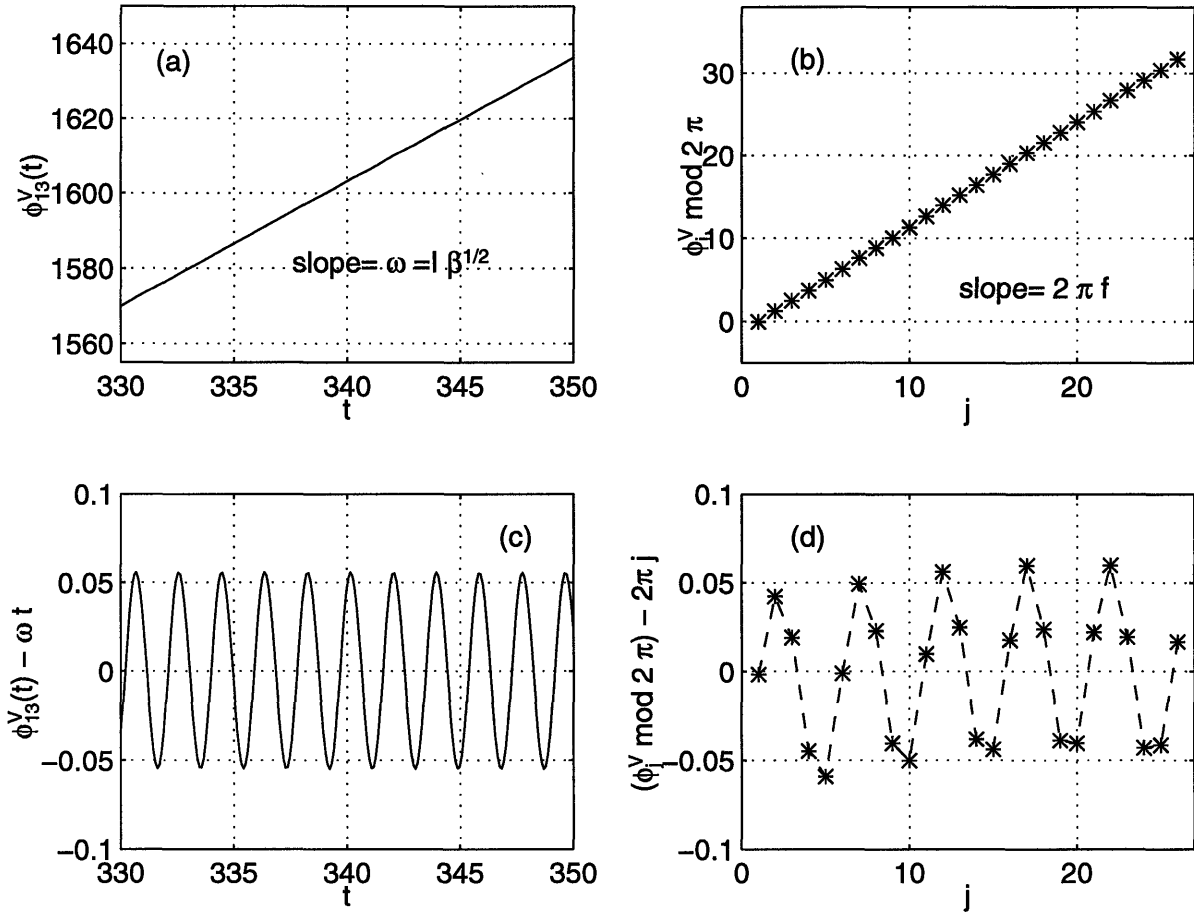


Figure 2-22: Numerical solution for the ohmic branch for a 25×1 ladder array with $\beta = 10, f = 0.2$ and driving current $I = 1.05$. The vertical phases grow linearly with time (a) and space (b). The result of subtracting the linear dependence is a small sinusoidal oscillation, as plotted in (c) and (d).

When no topological vortices are present in the array (i.e. $n_j = 0, \forall j$), the governing equations (2.18) become

$$\phi_j^V - 2\phi_j^H - \phi_{j+1}^V = -2\pi f \quad (2.95)$$

$$I + I_{j-1}^H = I_j^H + I_j^V \quad (2.96)$$

where the current in each branch, either vertical or horizontal, is related to the corresponding phase by

$$I_j = \ddot{\phi}_j + \frac{1}{\sqrt{\beta}} \dot{\phi}_j + \sin \phi_j.$$

Also, the boundary conditions are given by

$$I = I_1^H + I_1^V \quad I_N^H + I = I_{N+1}^V. \quad (2.97)$$

We note that the whirling solution for the *single* junction can be calculated perturbatively as [98]

$$\phi = \omega t + \frac{1}{\omega^2} \sin \omega t + \mathcal{O}\left(\frac{1}{\omega^3}\right)$$

where $\omega = I\sqrt{\beta}$ and ω^{-1} is the small parameter. Using this fact and the observed features of the solution, we assume a travelling wave solution for the vertical junctions

$$\phi_j^V = \xi_j + \frac{C_j}{\omega^2} \sin(\xi_j + \delta_j) \quad (2.98)$$

$$\xi_j = \omega t + 2\pi f j. \quad (2.99)$$

C_j and δ_j are functions to be determined consistently from the equations.

Let us begin with the simplest case in which we neglect the effect of the edges. This is equivalent to studying the region far away from the edges in a very long ladder array. Thus, we assume the following solution

$$\phi_j^{V\dagger} = \xi_j + \frac{A}{\omega^2} \sin \xi_j \quad (2.100)$$

where the amplitude of the modulation A does not change with j , since, when the

edges are at infinity, all the cells are equivalent.

Substitution of the assumed solution (2.100) in equation (2.95) yields the expression for the horizontal junctions

$$\phi_j^{H\dagger} = \frac{-A}{\omega^2} \sin(\pi f) \cos(\xi_j + \pi f). \quad (2.101)$$

From the expressions of the phases (2.100, 2.101), we calculate currents to $\mathcal{O}(1/\omega)$ from equation (2.96). We then substitute them in (2.96) to arrive at the value of A

$$A = \frac{1}{2 - \cos 2\pi f}, \quad (2.102)$$

which completes the solution far from the edges: $\{\phi_j^{V\dagger}, \phi_j^{H\dagger}\}$.

We include now the effect of the edges by assuming a solution where the superimposed modulation depends on the position j both in its amplitude and in its relative phase:

$$\phi_j^{V\dagger} = \xi_j + \frac{A_j}{\omega^2} \sin \xi_j + \frac{B_j}{\omega^2} \cos \xi_j. \quad (2.103)$$

We follow the same procedure as above to determine A_j and B_j . From substitution of $\phi_j^{V\dagger}$ in the governing equations (2.95)-(2.96), where we neglect terms of $\mathcal{O}(\omega^{-1})$ and higher, we obtain a system of two coupled second order difference equations for A_j and B_j

$$\frac{\cos 2\pi f}{2}(A_{j-1} + A_{j+1}) - 2A_j + \frac{\sin 2\pi f}{2}(B_{j-1} - B_{j+1}) = -1 \quad (2.104)$$

$$-\frac{\sin 2\pi f}{2}(A_{j-1} - A_{j+1}) + \frac{\cos 2\pi f}{2}(B_{j-1} + B_{j+1}) - 2B_j = 0. \quad (2.105)$$

After several algebraic manipulations, the general solution is found to be

$$A_j = A + c_1(re^{i2\pi f})^{j-(N+1)} + c_2(re^{i2\pi f})^{1-j} + c_3(re^{-i2\pi f})^{1-j} + c_4(re^{-i2\pi f})^{j-(N+1)}$$

$$B_j = i \{c_1(re^{i2\pi f})^{j-(N+1)} - c_2(re^{i2\pi f})^{1-j} + c_3(re^{-i2\pi f})^{1-j} - c_4(re^{-i2\pi f})^{j-(N+1)}\}$$

$$r = 2 + \sqrt{3}$$

where c_1, c_2, c_3, c_4 are constants to be determined from the boundary conditions. Note that, as in our analysis for the superconducting solutions in Section 2.3.1, r corresponds to a characteristic penetration depth which measures how much the influence of the boundaries is felt inside the array

$$r = e^{1/\lambda} \quad \Rightarrow \quad \lambda = 1/\ln r = 0.759.$$

The boundary conditions (2.97) allow us to solve *exactly* for the $\{c_i\}$. However, due to the small value of λ , we can simplify the analytical expressions by taking the limit $\lambda \ll N + 1$ which is valid even for very small ladders. In that case we obtain

$$c_1 = \frac{\sin \pi f}{2 - \cos 2\pi f} \frac{ie^{-i\pi f}}{3 - 1/r}, \quad c_4 = c_1^*$$

from the boundary condition at node $N + 1$. Similarly, from the boundary condition at node 1 follows

$$c_2 = c_1, \quad c_3 = c_4.$$

Substituting back in (2.103) and (2.95) we obtain the solution which includes edge effects:

$$\phi_j^{V\dagger} = \phi_j^{V\dagger} - \frac{A}{\omega^2} \frac{2r \sin \pi f}{3r - 1} \left\{ r^{j-(N+1)} \cos(\xi_{N+1} + \pi f) - r^{1-j} \cos(\xi_1 - \pi f) \right\} \quad (2.106)$$

$$\phi_j^{H\dagger} = \phi_j^{H\dagger} - \frac{A}{\omega^2} \frac{(r - 1) \sin \pi f}{3r - 1} \left\{ r^{j-N} \cos(\xi_{N+1} + \pi f) + r^{1-j} \cos(\xi_1 - \pi f) \right\} \quad (2.107)$$

where $\{\phi_j^{H\dagger}, \phi_j^{V\dagger}\}$ is the solution in the absence of edges from (2.100)- (2.101). We also summarize the notation introduced in the derivation

$$A = \frac{1}{2 - \cos 2\pi f}, \quad r = 2 + \sqrt{3}, \quad \xi_j = \omega t + 2\pi f j, \quad \omega = I\sqrt{\beta}. \quad (2.108)$$

We show now that the obtained solution agrees very well with the numerics in its defining characteristics:

- The almost linear dependence of $\phi_j^V(t)$ both with t and j was introduced in the travelling wave assumption (2.98) as our zeroth order approximation. This characterizes this solution as a linearly extended kink in which the pendula whirl with almost constant frequency. Both “slopes” (the frequency and the wavenumber) are deduced consistently from the governing equations.
- The small superimposed modulation of $\mathcal{O}(\omega^{-2})$ in the vertical junctions is a result of the nonlinear term in the equation of the single junction. Significantly, the coordinate for this modulation is still the travelling wave coordinate. Thus, both the frequency and the wavelength of the accompanying oscillation are commensurate with the zeroth order solution.
- The modulation of the vertical junctions produces an equally small, out of phase oscillation of the horizontal junctions. Hence, these librate with amplitudes of order $\mathcal{O}(\omega^{-2})$.

These results constitute the basic mathematical representation of the *whirling mode*, i.e. the solution of our system for $\omega \rightarrow \infty$.

We can also check other predictions which can be deduced from the calculated solution:

- The amplitude of the accompanying oscillations depends on the magnetic field f . This is most easily seen if we consider the solution far from the edges (2.100)-(2.102). In that case, the amplitude of the oscillations for the horizontal junctions is

$$\max\{\phi_j^{H\dagger}\} = \frac{\sin \pi f}{I^2 \beta (2 - \cos 2\pi f)}.$$

Good agreement is obtained in Figure 2-23 when checking this prediction with the numerical values of the amplitude of the horizontal junction in the middle (i.e. most distant from the edges) of a $N = 25$ ladder array for different values of f .

- The effect of the edges, as introduced by the boundary conditions (2.106) and (2.107), is mathematically expressed as an additional modulation from the end

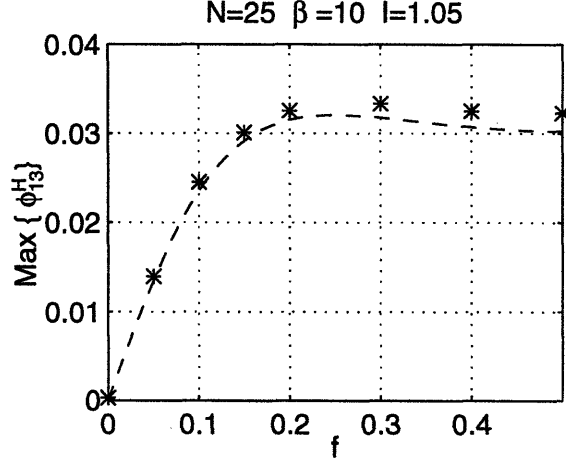


Figure 2-23: For different magnetic fields f , predicted (- -) and numerical (*) values of the amplitude of the oscillations of the horizontal junction most distant from the edges for the whirling mode of a 25×1 ladder array

junctions, wrapped in an exponential envelope. The decay of the perturbation from the edges is parametrized with a characteristic length $\lambda = 1/\ln r = 0.759$. We test this prediction in Figure 2-24 by plotting the numerical values of $\kappa_j \equiv \phi_j^H(t_0) - \phi_{j-2}^H(t_0)$ for our array with $f = 0.5$. Let us calculate the predicted value of this quantity from our solution. When $f = 0.5$, the wavelength is equal to two cell lengths and $\phi_j^{H\dagger} = \phi_{j-2}^{H\dagger}$. From equation (2.107) we conclude that κ_j decays exponentially with j from the edges

$$\kappa_j^\dagger = \{\phi_j^{H\dagger}(t_0) - \phi_{j-2}^{H\dagger}(t_0)\} \approx \begin{cases} r^{1-j}, & j \rightarrow 1 \\ r^{j-N}, & j \rightarrow N. \end{cases} \quad (2.109)$$

Hence, the slope of the logarithmic plot is predicted to be equal to $-\ln r = -1.317$ close to the left end of the array, and 1.317 close to the right edge. The agreement of this prediction with the numerical values, shown in Figure 2-24 (b), is excellent.

In summary, the influence of the edges in the whirling mode is virtually unnoticeable. The characteristic length is small and the edge corrections die off very sharply, as seen in Fig. 2-24 (a). In contrast with the importance of the boundary effects for the superconducting solutions, we will not need to consider

N=25 $\beta=10$ $f=0.5$ $l=1.05$

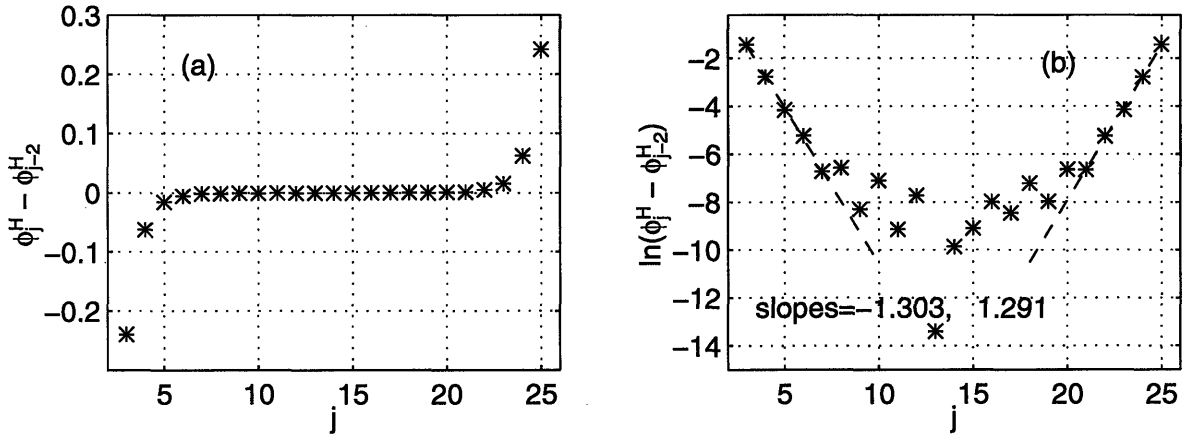


Figure 2-24: The effect of the edges in the whirling mode are most easily observed in the case $f = 0.5$. Then $\kappa_j = \phi_j^H(t_0) - \phi_{j-2}^H(t_0)$ decays exponentially from the edges, as seen in (a). The slopes of the logarithmic plot (b) near the edges give us the characteristic length in very good agreement with the predicted value: $\ln(2 + 3^{1/2}) = 1.317$

these corrections in the subsequent calculations for the whirling mode.

In connection with the previous points, we observe that in the absence of magnetic field, the librations of the horizontal junctions have zero amplitude to this order of the approximation, $\mathcal{O}(\omega^{-2})$. Likewise, edge effects also disappear. The mathematical description of the whirling mode when $f = 0$ is then simpler: the phases of the horizontal junctions are permanently zero, and the vertical junctions whirl in phase and in unison with an almost constant frequency—the correction of $\mathcal{O}(\omega^{-2})$ is still present for them. Consequently, it is tempting to consider the array as a collection of $N + 1$ uncoupled junctions, which behaves as a single junction. We will see in the following sections that this is not the case. The coupling, which the geometric and physical constraints introduce, is still present and modifies the mechanism for the instability of the whirling mode. Hence, the repinning for the array is not the same as for the single junction.

2.4.2 Instabilities in the whirling branch and repinning

We study now the mechanism for the observed instability of the whirling branch following a procedure developed partly in collaboration with one of the authors in [99, 96]. It is, in essence, a linear stability analysis of the whirling solution used there to study one-dimensional parallel arrays. In those devices no horizontal junctions are present and vertical junctions are coupled through an inductive term parametrized by a normalized inductance Λ . The main conclusion obtained there is that the repinning of the 1-D parallel array is caused by parametric instabilities of the whirling mode when its driving frequency resonates subharmonically with the eigenfrequencies of the array, regarded as an LC-transmission line. Depending on the value of Λ , the sequence of instabilities of the different modes will produce a series of steps or a single repinning instability.

However, no inductances are considered for our ladder array and the effective coupling is intrinsic to the system. In summary, of the material and array dependent parameters only the damping $\Gamma \equiv 1/\beta$ remains as a variable, since we take the limit $\lambda_{\perp} \rightarrow \infty$, $T \rightarrow 0$. In close comparison with the one-dimensional parallel array, we concentrate on studying three questions :

- when the instability happens;
- the possibility of observing steps as in the one-dimensional case;
- the comparison of the instability of the whirling branch of a ladder array with the bifurcation which causes the repinning for the single junction.

The procedure follows closely on the linear stability analysis developed in Section 2.3.1, particularizing those results for the whirling solution from Section 2.4.1. There we found that the whirling solution is well approximated by

$$\phi_j^{V*} = \xi_j + \mathcal{O}\left(\frac{1}{\omega^2}\right), \quad \phi_j^{H*} = \mathcal{O}\left(\frac{1}{\omega^2}\right)$$

with $\xi_j = \omega t + 2\pi f j$ and $\omega = I\sqrt{\beta} \gg 1$. This is valid both for the case in which edges are taken into account and when their effects are negligible.

We begin by adding a small perturbation $\{u_j, v_j\}$ to the basic solution above $\{\phi_j^{V*}, \phi_j^{H*}\}$ and studying the dynamical equations of the added perturbation in momentum space (i.e. the modal equations) as described in Section 2.3.1. Neglecting terms of order $\mathcal{O}(1/\omega^2)$, substitution in equation (2.28) gives

$$\begin{aligned} \ddot{\tilde{u}}_m + \frac{1}{\sqrt{\beta}} \dot{\tilde{u}}_m + \frac{a_m - 1}{a_m} \tilde{u}_m + \frac{1}{a_m} \sum_{n=0}^{N'} \tilde{u}_n v_{nm} &= 0 \\ v_{nm} &= \frac{2}{N+1} \sum_{j=1}^{N=1} \cos \xi_j \cos \left[\frac{n\pi}{N+1} (j - 1/2) \right] \cos \left[\frac{m\pi}{N+1} (j - 1/2) \right] \end{aligned} \quad (2.110)$$

where v_{nm} is the coupling coefficient between modes n and m .

If $f > 0$, the basic solution is j dependent and the modal equations are coupled. Thus, the analysis has to be done numerically by calculating the Floquet multipliers: when any of the multipliers becomes larger than unity, the perturbation grows, and the whirling branch becomes unstable. We do not consider here the case $f > 0$ but rather concentrate on the $f = 0$ case which allows more extensive analytical treatment. However, numerical studies carried out for one-dimensional parallel arrays [99] show that the main features of the analysis do not change in the presence of the magnetic field, thus suggesting the general validity of the physical picture emerging from the $f = 0$ case.

Case $f = 0$

When the applied magnetic field is zero, the basic solution is not space dependent: $\cos \xi_j = \cos \omega t$. Then equation (2.110) becomes uncoupled and simplifies to

$$\begin{aligned} \ddot{\tilde{u}}_m + \frac{1}{\sqrt{\beta}} \dot{\tilde{u}}_m + \left\{ \omega_m^2 + (1 - \omega_m^2) \cos \omega t \right\} \tilde{u}_m &= 0 \\ \omega_m^2 &= \frac{2s_m^2}{1 + 2s_m^2}, \quad s_m^2 = \sin^2 \frac{m\pi}{2(N+1)} \quad m = 0, \dots, N. \end{aligned} \quad (2.111)$$

Thus the dynamics of each of the Fourier modes of the perturbation $\tilde{u}_m(t)$ is governed by a Mathieu equation where the driving frequency is that of the basic whirling solution ω . The ω_m are the eigenfrequencies of the lattice. Notice in the expression

for s_m above, that modes from open ended boundary conditions correspond to modes from periodic boundary conditions with *double* the number of junctions [99]. This is a direct result of using Fourier transforms which fulfill the open ended boundary conditions.

For the whirling solution to remain stable, the null-perturbation solution

$$\tilde{u}_m(t) \equiv 0, \quad \forall m$$

has to be stable, i.e. an added perturbation will not grow without bound. The appearance of instabilities in the whirling branch can be understood within this picture as a result of the existence of instability regions in the parameter space of the Mathieu equation corresponding to the modes of the perturbation [37]. To show this, we first write 2.111 in the canonical form

$$\frac{d^2 \tilde{u}_m}{d\tau^2} + \gamma \frac{d\tilde{u}_m}{d\tau} + (\delta + \epsilon \cos \tau) \tilde{u}_m = 0 \quad (2.112)$$

by redefining

$$\tau = \omega t \quad \gamma = \frac{1}{\omega \sqrt{\beta}} \quad \delta = \frac{\omega_m^2}{\omega^2} \quad \epsilon = \frac{\delta}{2s_m^2}. \quad (2.113)$$

Let us consider the undamped system ($\gamma = 0$) first. The theory of Mathieu functions establishes that the stability of the solution $\tilde{u}_m(\tau) \equiv 0$ depends on the relative value of δ and ϵ . There exist regions of the (δ, ϵ) plane, called *Mathieu tongues*, where this solution is unstable, the perturbation grows exponentially and, thus, the whirling branch becomes unstable (Figure 2-25). Two observations are important:

- ϵ depends linearly on δ with a slope $1/2s_m^2$, which is different for each mode
- the high I limit corresponds to $\omega \rightarrow \infty \Rightarrow (\delta, \epsilon) \rightarrow (0, 0)$.

Therefore, the physical picture is the following: For high I -i.e. very small δ and ϵ - the null solution for the perturbation is stable, and so is the whirling branch. As I

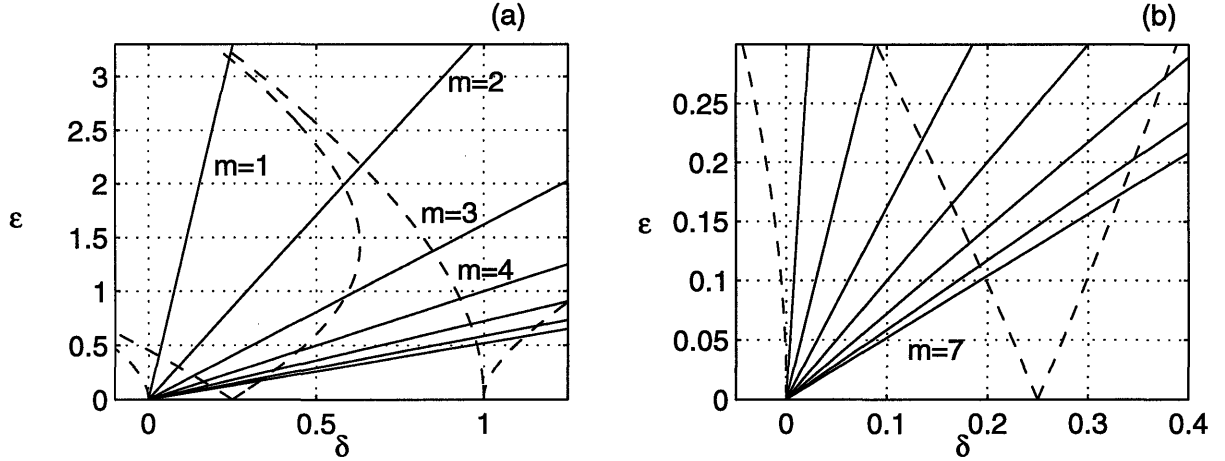


Figure 2-25: First and second Mathieu tongues in (δ, ϵ) parameter space in the absence of damping. Figure (b) is a blowup of (a). Dashed lines mark the boundaries of the tongues, i.e. points where the stability of the solution changes. Close to the origin, all modes are stable. Solid lines correspond to the modes $m = 1, \dots, 7$ for a $N = 7$ ladder.

is decreased, we move away from the origin following a different line for each mode. Each of them becomes unstable for different intervals marked by the crossings of the corresponding line with the first Mathieu tongue (Figure 2-25).

This overall description is unchanged in the presence of damping. When $\gamma > 0$, the tongues become narrower and their general shape is modified. If γ is big enough, the tongue's width shrinks to zero, and the interval of instability does not exist. Thus, the mode will always be stable. This can be seen by perturbatively calculating the boundary of the first Mathieu tongue [37] as:

$$\delta = \frac{1}{4} \mp \frac{\epsilon}{2} \sqrt{1 - \left(\frac{\gamma}{\epsilon}\right)^2} + \mathcal{O}(\epsilon^2) \quad (2.114)$$

where ϵ is the small parameter. The tongue disappears when $\gamma > \epsilon$ so that no instability is observed for the mode in that case.

Hence, given β , or the corresponding damping $\Gamma = 1/\sqrt{\beta}$, the m^{th} mode is unstable

when $\omega \in [\Omega_m^-, \Omega_m^+]$ given by

$$\Omega_m^\pm = \sqrt{4\omega_m^2 - \frac{2}{\beta} \pm \frac{2}{\beta} \left[\left(1 - \beta \frac{\omega_m^2}{2s_m^2}\right)^2 + 2\beta \left(\frac{\omega_m^2}{2s_m^2} - 2\omega_m^2\right) \right]^{1/2}}. \quad (2.115)$$

If $\gamma > \epsilon$, there is no instability. This expression is obtained by substituting the definitions 2.113 in equation (2.114) and solving for ω . It gives the crossing points of the first Mathieu tongue and the m^{th} mode line for $\gamma > 0$ and $\epsilon \rightarrow 0$ (similar to the $\gamma = 0$ case depicted in Figure 2-25). Note that each interval is roughly centered around $\omega \simeq 2\omega_m$. The theory of Mathieu functions predicts instabilities at those points, which correspond to subharmonic resonances with the eigenmodes of the lattice, at double their frequency.

Non-overlapping instability intervals for different modes will produce steps in the $I - V$ curves. While in these unstable regions of the whirling solution, the system must evolve to another dynamic state. Once the stability for all modes has been regained, the system can switch back to the whirling branch. However, this will not happen if the intervals overlap or the separation between them is small. Moreover, for the described instabilities to be observed they must occur before the whirling solution ceases to exist, due to either a saddle-node or a homoclinic bifurcation [31], at a critical current I_{whirl} as explained below.

In summary, when studying the instabilities from the whirling branch for a ladder array with N cells and a given β we must consider the following three criteria. The step corresponding to the instability of mode m will *not* be observable if any of the following conditions is met:

1. if there is overlap with another instability interval

$$\Omega_m^+ > \Omega_{m+1}^- \quad (2.116)$$

2. if, due to the magnitude of the damping, i.e. $\gamma > \epsilon$, the tongue disappears.

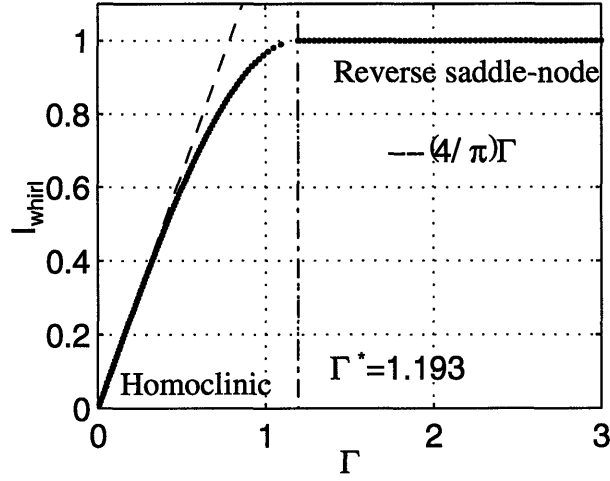


Figure 2-26: I_{whirl} vs. $\Gamma = \beta^{-1/2}$ for a single junction. For small $\Gamma \leq \Gamma^* \simeq 1.2$, the repinning occurs through a hysteretic homoclinic bifurcation. Above that value of the damping, a non hysteretic saddle-node bifurcation takes place.

Imposing this condition in 2.115 results in

$$(1 + 2s_m^2)(4s_m^2 - \sqrt{16s_m^4 - 1}) < \beta < (1 + 2s_m^2)(4s_m^2 + \sqrt{16s_m^4 - 1}) \quad (2.117)$$

3. if the basic whirling solution ceases to exist before the instability of the mode occurs

$$\Omega_m^+ < \omega_{whirl}. \quad (2.118)$$

Let us digress briefly to give a more detailed explanation of the third point. In Section 2.4.1 we concluded that, within our approximation, the whirling solution for the ladder array with $f = 0$ is effectively equivalent to a set of $N + 1$ almost independent in-phase whirling pendula. The couplings, corrections and oscillations of the horizontal junctions are negligible to order $\mathcal{O}(1/\omega^2)$. The same holds even when edge effects are included. Therefore, the existence of the running periodic solution for a single junction is a necessary condition for the existence of the whirling branch for the ladder [78, 31]. The basic features of the single junction are represented in Figure 2-26. In short, the single junction has a periodic attractor in its cylindrical phase space which ceases to exist through two different bifurcations:

- a saddle-node bifurcation at $I_{whirl} = 1$ for $1/\sqrt{\beta} \equiv \Gamma > \Gamma^* \simeq 1.2$
- a homoclinic bifurcation for $\Gamma < \Gamma^*$ characterized by the small damping limiting behavior [31]

$$\lim_{\Gamma \rightarrow 0} I_{whirl} = \frac{4}{\pi\sqrt{\beta}}.$$

From this critical current I_{whirl} we can obtain a lower bound ω_{whirl} for the observation of any instabilities in the whirling branch. For the high I limit, the first order approximation is good enough so that $\omega \simeq I\sqrt{\beta}$. However, as I gets smaller, we need to consider higher order corrections in the perturbative expansion for the running periodic solution of the single junction [98]:

$$\begin{aligned} \phi = \tau + \epsilon^2 \sin \tau &+ \epsilon^3 \Gamma \cos \tau + \epsilon^4 \left\{ -\Gamma^2 \sin \tau + \frac{1}{8} \sin 2\tau \right\} \\ &+ \epsilon^5 \left\{ -\Gamma^3 \cos \tau + \frac{\Gamma}{8} \cos 2\tau + \frac{\Gamma}{16} \sin 2\tau \right\} + \mathcal{O}(\epsilon^6) \end{aligned} \quad (2.119)$$

$$\tau = \left(1 - \frac{\epsilon^4}{2}\right) I\sqrt{\beta} t \quad (2.120)$$

$$\epsilon = \frac{1}{I\sqrt{\beta}} \ll 1 \quad \Gamma = \frac{1}{\sqrt{\beta}} \quad (2.121)$$

Thus, the observed voltage $\langle \dot{\phi} \rangle \equiv \omega$ to $\mathcal{O}(\epsilon^3)$

$$\omega \simeq \left(1 - \frac{1}{2I^4\beta^2}\right) I\sqrt{\beta} = I\sqrt{\beta} - \frac{1}{2}(I\sqrt{\beta})^{-3}$$

is used to calculate ω_{whirl} for a given I_{whirl} .

We return now to the discussion of the three criteria listed above for the observation of mode instabilities. They are summarized in Figure 2-27 (c) for a 7×1 ladder. There we represent, for different values of β , all the *existing* instability intervals $[\Omega_m^-, \Omega_m^+]$, as given by Eq. 2.115, together with the instability frequency for the single junction $\omega_{whirl}(\beta)$. The overdamped singular limit $\beta = 0$ is excluded from the analysis. The overall features of our predictions agree well with the observed numerical values of the repinning voltages for $f = 0$ and varying β (Figure 2-27 (b)):

- The first important conclusion is that the ladder array in the limit of no inductances presents *no series of steps on the return path around the whirling branch when this becomes unstable*. This is so because the instability intervals always overlap. There is no single mode whose instability region ends before the next mode goes unstable. Therefore, once the first becomes unstable, there is no interval in which the stability of all the modes is regained and, thus, the whirling branch never restabilizes. In conclusion, no steps are observable.
- As β decreases (and the damping increases) the tongues corresponding to higher number modes cease to exist and so do the instabilities associated with them. Hence, *the repinning frequency decreases with decreasing β* .
- For the range of β considered, the homoclinic bifurcation is never reached. The whirling branch becomes unstable before it ceases to exist. Therefore, although the array for $f = 0$ can be viewed as a collection of “uncoupled” vertical junctions, *the repinning mechanism for the array is different to that of a single junction*. The eigenmodes of the lattice, modified by the presence of the horizontal junctions, play a role in the instabilities leading to the repinning of the array.

Two further comments are in order. First, as expected, the physical picture does not change when N is increased. The distances between resonating frequencies decrease as their number increases and the above conclusions become more accentuated. On the other hand, for smaller arrays the effects of discretization become more important. We have checked however that steps do not appear even for the smallest ladder of $N = 2$ cells since the instability intervals still overlap. Secondly, the use of equation (2.115) to approximate the width of the intervals is justified for large mode number $m \simeq N + 1$, since then $\epsilon \simeq 1/8s_m^2 \simeq 1/8$. The approximation gets worse for small m , when ϵ becomes large. Consequently, we have verified that the general conclusion does not change when the full numerical solution for the boundaries of the tongues is used, as shown in Figure 2-25.

We finish this section by establishing the comparison of the ladder array with the

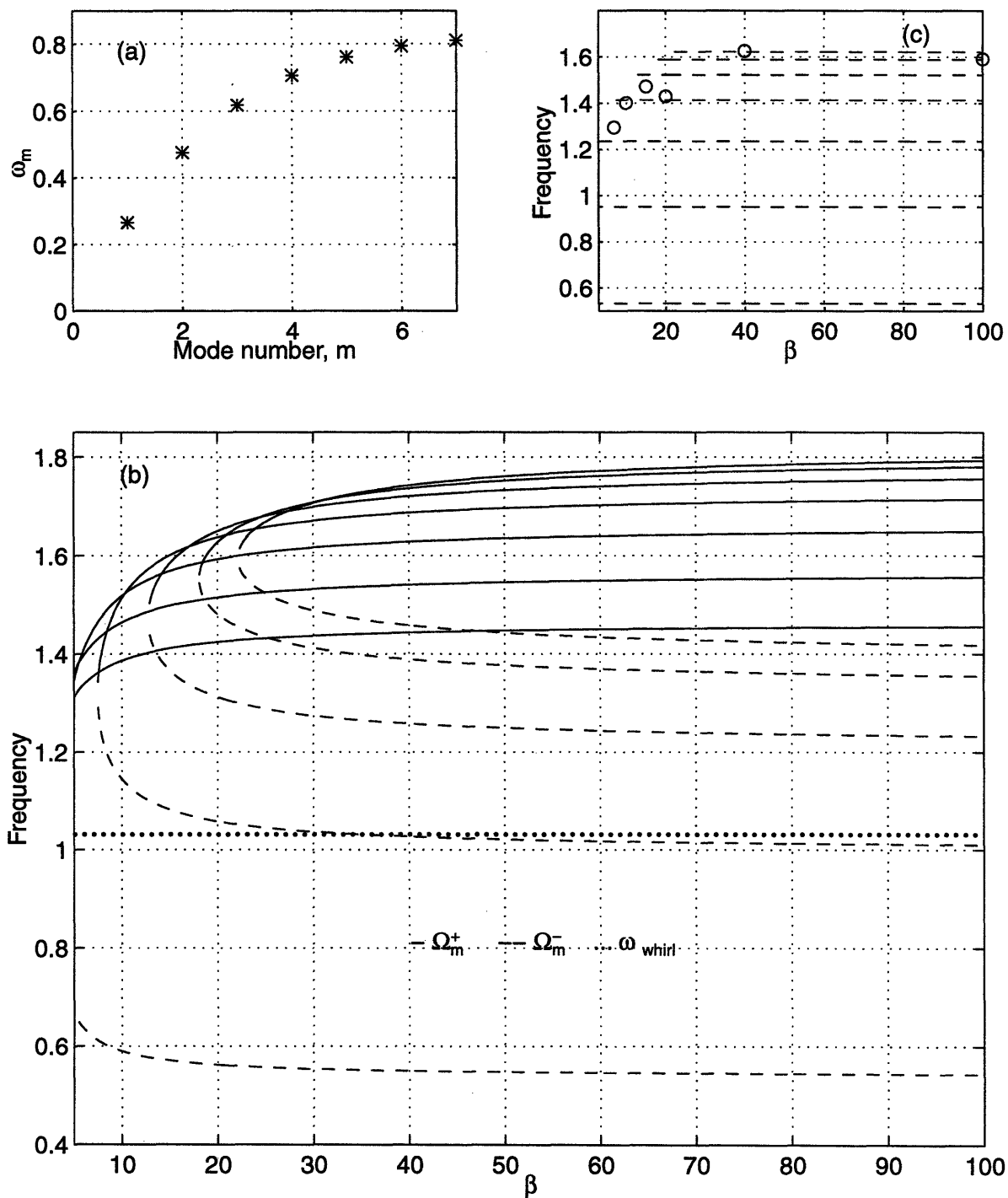


Figure 2-27: (a) Frequencies ω_m and (b) instability intervals associated with them, of the modes of an open ended 7×1 ladder. (c) Central instability frequencies $2\omega_m$ (- -) and numerically observed repinning frequencies (o) for the same array. As the damping increases, some of the instabilities cease to exist.

one dimensional parallel array studied by Watanabe *et al.* [99]. In their case, no horizontal junctions exist and the coupling between vertical junctions is introduced through the normalized inductance Λ , which is also a characteristic length of the kink in the array. The dispersion relation was

$$\omega_m^{par} = 2\Lambda s_m$$

and the steps are not observable when the inductances are too small. Instead, we have neglected the electric inductances in our arrays. The coupling between vertical junctions is intrinsic to the geometry and due to the physical constraints the horizontal junctions introduce. The dispersion relation is now:

$$\omega_m^{lad} = \sqrt{\frac{2}{1 + 2s_m^2}} s_m. \quad (2.122)$$

This modified dispersion relation has the effect of compressing the mode frequencies, making their separation smaller. This, together with the smallness of Λ , explains the impossibility of observing the steps produced by the restabilization of the whirling branch. The introduction of non-zero inductances in the problem is an unresearched direction of great interest.

From the comparison of the dispersion relations above, a small “intrinsic inductance” $\Lambda^{lad} \in [1/\sqrt{2}, 1/\sqrt{6}] \sim 1/\sqrt{2}$ can be assigned to our ladder. This was precisely the characteristic length for the sine-Gordon kink approximation as described in Section 2.3.3. In fact, this is consistent with the description of the horizontal junctions as oscillating pendula with very small amplitude. In this limit, their behavior can be approximated as an inductor with the Josephson inductance L_J

$$\left. \begin{array}{l} V = \Phi_0/2\pi \dot{\phi} \\ I = I_c \sin \phi \simeq I_c \phi \end{array} \right\} \Rightarrow V = \frac{\Phi_0}{2\pi I_c} \frac{dI}{dt} = L_J \frac{dI}{dt}. \quad (2.123)$$

This renders our array equivalent to a one-dimensional parallel array, like the ones studied in [99], with self-inductance $2L_J$, i.e. $\Lambda = 1/\sqrt{2}$. However, the dispersion

relation already indicates that this is not a strict correspondence. Similarly, our conclusions in Section 2.3 show that the identification of the horizontal junctions as mere inductors is an oversimplification. The most compelling evidence for the importance of the horizontal junctions, beyond providing an intrinsic coupling or inductance in the system, is given in Section 2.4.3 where they are shown to participate non-negligibly in new fully two-dimensional modes which exist only because of the presence of these horizontal junctions.

2.4.3 Novel subharmonic whirling state at zero field

In the preceding section we established that the instability of the ohmic branch for the ladder array is caused by the instabilities of the Mathieu modes associated with the whirling solution, much in the same way as for parallel arrays [96]. An alternative, more particular, description of this process will be detailed now for $f = 0$. In this case, and for a certain range of β , new branches appear on the return path of the $I - V$ curve when the whirling mode becomes unstable.

The usual $I - V$ curve for a ladder array with $f = 0$ and $\beta > 0$ resembles the single junction's. The *single junction* stays on the superconducting branch until it becomes unstable at $I = 1$ and then switches to the quasi-harmonic whirling branch, which is characterized by an almost linear dependence of V with I . If $\beta > \beta^* \simeq 0.7$, the return path is hysteretic: the system stays on the whirling branch until it ceases to exist at $I_{whirl} < 1$, at which point it returns to the superconducting solution through a homoclinic bifurcation. If $\beta < \beta^*$, the return path is not hysteretic and the mechanism for instability is simply an inverse saddle-node bifurcation [31, 78].

For a ladder array with $f = 0$, the initial sequence is identical (i.e. all the junctions in the ladder depin at the same time acting as a single junction). However, the return path is not. Firstly, in contrast with the single junction behavior, the instability of the whirling branch is due to subharmonic resonances with the eigenmodes of the lattice (as in the Mathieu description in Section 2.4.2). Secondly, when the whirling branch becomes unstable, in many instances the system does not return directly to the superconducting solution but to a *new* intermediate branch with non-vanishing V . Representative $I - V$ characteristics in Figure 2-28 show this behavior. Note that it is not observed for very small or very large β .

In the following, we obtain an approximate solution for this intermediate branch. The appearance of such a solution is a consequence of the presence of horizontal junctions which are intrinsically coupled to the vertical ones due to the physical constraints of the system (i.e. Kirchoff's law and the fluxoid quantization). The existence of this coupling is also necessary to explain the instability of the whirling

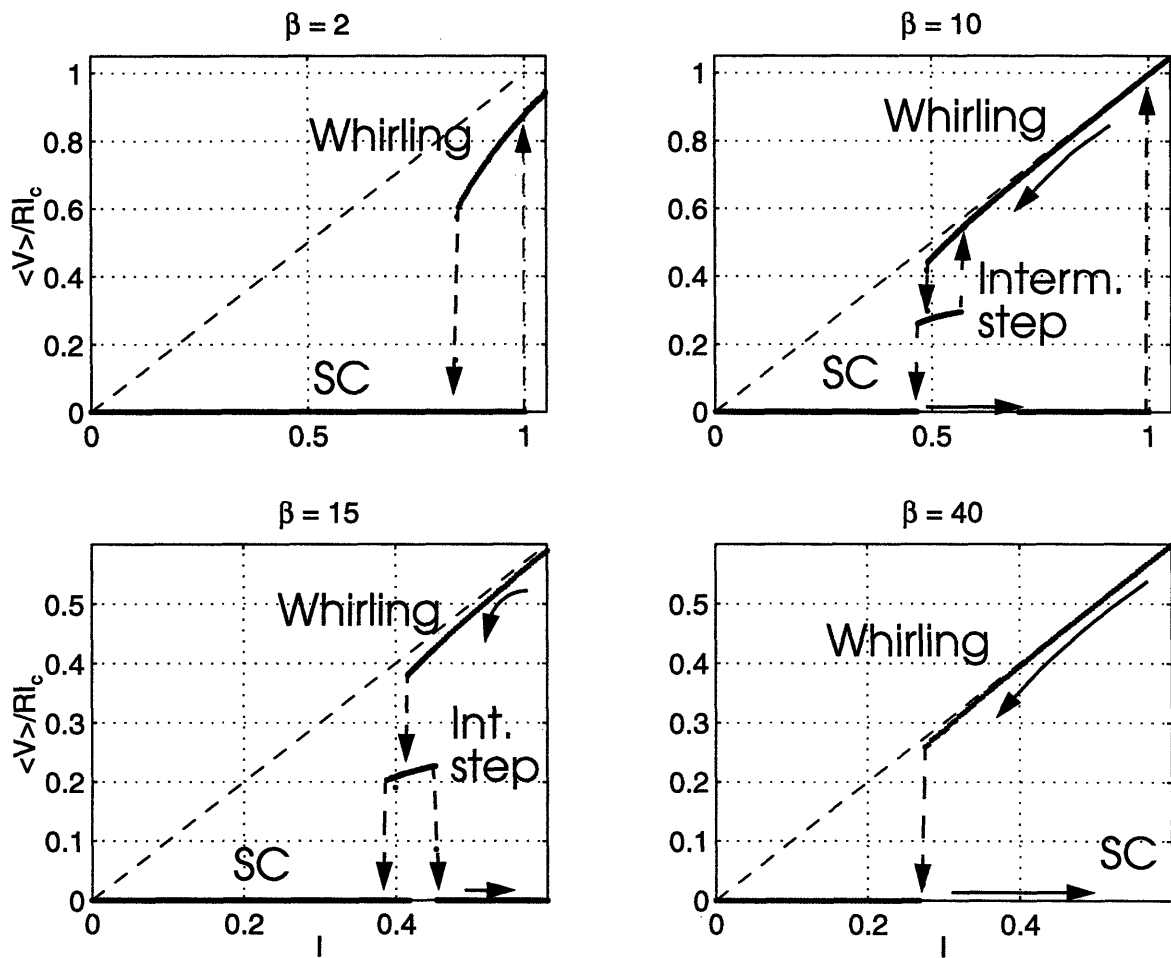


Figure 2-28: $I - V$ characteristics for ladder arrays with $f = 0$ for different values of β . The direct path is always the same, with $I_{dep} = 1$. For $\beta = 10$ and 15 the intermediate branch is observed.

branch. In the simplest approximation for the whirling mode, the horizontal junctions are ignored by assuming their phases are identically zero -and therefore uncoupled to the vertical ones- and the vertical junctions, all in phase, behave like one single junction. This simplification does not account for the observed branches and the instability process.

Description of the observed solution and reduction of the system

Snapshots of a representative numerical solution for the intermediate branch are shown in Figure 2-29. Its main feature is readily identified: the horizontal junctions have the structure of a standing wave with a node on every other cell

$$\phi_{2j}^H(t) = 0, \quad \forall j, t \quad (2.124)$$

We find now solutions for the ladder compatible with this restriction. By substituting the identity (2.124) in the governing equations (2.95)-(2.96), we obtain

$$\forall j, t \quad \left\{ \begin{array}{l} \phi_{2j}^V(t) = \phi_{2j+1}^V(t) \\ I_{2j-1}^H = -I_{2j+1}^H \Rightarrow \phi_{2j-1}^H(t) = -\phi_{2j+1}^H(t) \end{array} \right. \quad (2.125)$$

which explains all the features of the observed solution (Figure 2-29).

Subsequent substitutions and rearrangements in the governing equations allow us to express all the phases in terms of just two variables, i.e. the phases of the first horizontal and vertical junctions $\phi_1^H(t)$ and $\phi_1^V(t)$. This particular solution for the complete ladder array is given by

$$\left\{ \begin{array}{l} \phi_{2j}^H(t) = 0 \\ \phi_{2j+1}^H(t) = (-1)^j \phi_1^H(t) \\ \phi_{2j-1}^V(t) = \phi_1^V(t) - \phi_1^H(t) + (-1)^{j+1} \phi_1^H(t) \\ \phi_{2j+1}^V(t) = \phi_{2j}^V(t). \end{array} \right. \quad (2.126)$$

Therefore, the time evolution of the whole system is governed by the dynamical equations of those two variables.

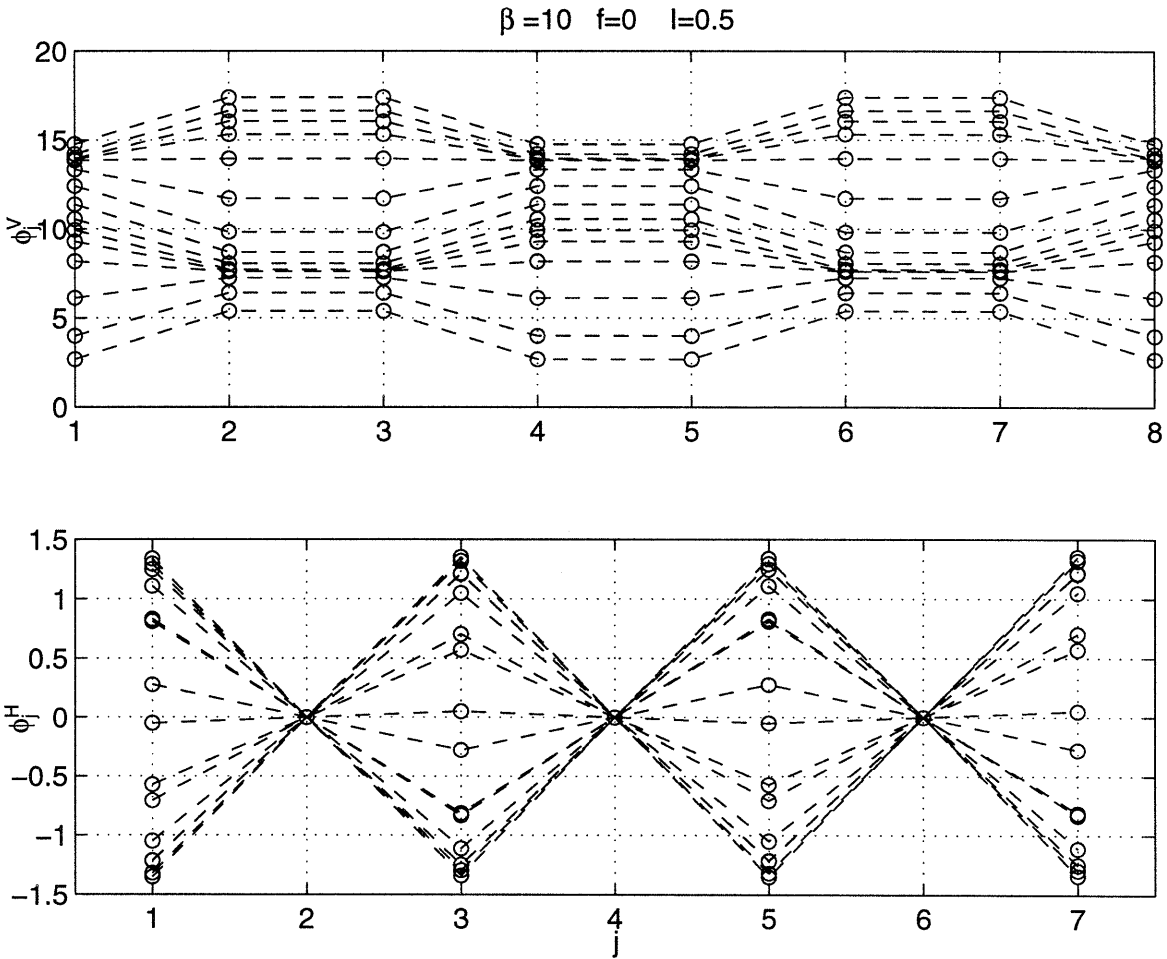


Figure 2-29: Snapshots of ϕ_j^H and ϕ_j^V for a 7×1 ladder array

The equations for ϕ_1^H and ϕ_1^V are obtained from the defining equations (2.18) particularized at nodes 1 and 2

$$\begin{aligned} I &= I_1^H + I_1^V \\ I + I_1^H &= I_2^V \\ \phi_2^V &= \phi_1^V - 2\phi_1^H. \end{aligned} \tag{2.127}$$

The result is compactly expressed as

$$\begin{aligned} \ddot{v} + \frac{1}{\sqrt{\beta}}\dot{v} + \sin v \cos h &= I \\ \ddot{h} + \frac{1}{\sqrt{\beta}}\dot{h} + \sin h \cos^2 \frac{v}{2} &= 0 \end{aligned} \tag{2.128}$$

where we have defined

$$v \equiv \phi_1^V - \phi_1^H \quad h \equiv \phi_1^H. \tag{2.129}$$

In Figure 2-30 we show the comparison of the phase portraits of the full (2.18) and reduced (2.128) systems dynamically integrated from the same initial condition. It clearly shows their equivalence. Thus, for this specific solution, the dimensionality of the system is drastically reduced. In effect, we have mapped our original system of $3N + 1$ coupled pendula onto a system of two coupled nonlinear oscillators. The external drive is directly applied on one of them which in turn drives the other coupled pendulum. Translated into our original context: the external current directly drives the whirling of the vertical junctions which drive the horizontal ones via the intrinsic coupling that the physical constraints of the system impose.

Analysis of the reduced system

The analytical study of the reduced system (2.128) is possible due to its lower dimensionality, drastically reduced from the full model (2.18). We begin the analysis by checking that its limiting regimes correspond to the superconducting and whirling solutions of the full system. Secondly, we will obtain an analytical approximation for

$$I = 0.5 \quad f = 0 \quad \beta = 10$$

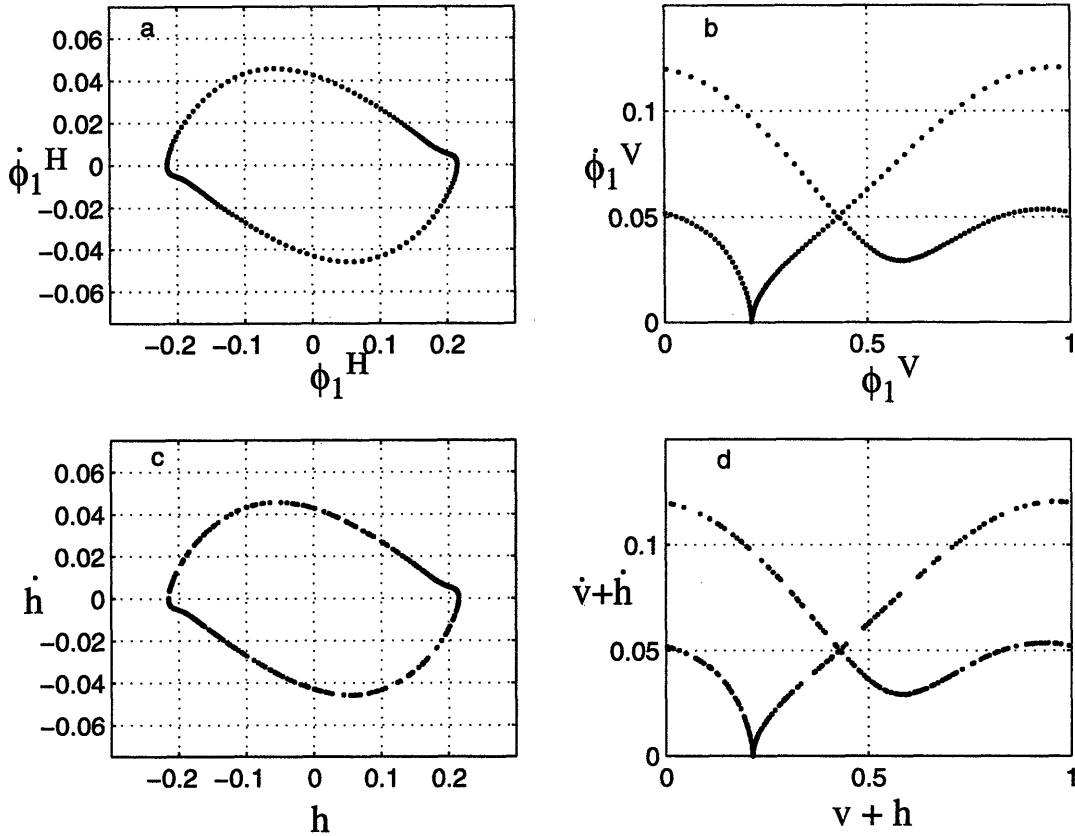


Figure 2-30: Comparison of the the full and reduced systems. The top row contains phase portraits from the full system for (a) ϕ_1^H and (b) ϕ_1^V . In the bottom row we represent the corresponding phase portraits from the reduced system: (c) h and (d) $v+h$

the new observed solution and interpret its main properties in connection with the original model.

Limiting regimes

- **Static solutions:** The fixed points $\{v_{st}, h_{st}\}$ of the reduced system (2.128) are obtained by requiring $\ddot{v} = \dot{v} = \ddot{h} = \dot{h} = 0$, which yields

$$\begin{aligned}\sin(v_{st}) \cos(h_{st}) &= I \\ [1 + \cos(v_{st})] \sin(h_{st}) &= 0.\end{aligned}\tag{2.130}$$

There are three distinct solutions to this system:

1. $v_{st} = \pi$ and h_{st} indeterminate: multiple solution, valid only when $I = 0$.
2. $h_{st} = 0$ and $\sin v_{st} = I$: equivalent to the stable superconducting solution with

$$\phi_{2j}^H = 0 \quad \phi_j^V = \arcsin(I), \forall j.$$

3. $h_{st} = \pi$ and $\sin v_{st} = -I$: corresponds to the unstable superconducting solution with

$$\phi_{2j}^H = 0 \quad \phi_{2j+1}^H = \pi \quad \phi_j^V = \pi - \arcsin(I).$$

As expected, these static solutions are the same as for the full system.

- **Whirling solution:** In the $I\sqrt{\beta} \gg 1$ limit, the solution for the reduced system is similar to the usual whirling mode in one dimensional parallel arrays [96] or in ladder arrays (Section 2.4.1). To show this, rewrite the reduced system (2.128) as

$$\frac{d^2v}{d\tau^2} + \epsilon \frac{1}{\sqrt{\beta}} \frac{dv}{d\tau} + \epsilon^2 \sin v \cos h = \frac{\epsilon}{\sqrt{\beta}}\tag{2.131}$$

$$\frac{d^2h}{d\tau^2} + \epsilon \frac{1}{\sqrt{\beta}} \frac{dh}{d\tau} + \epsilon^2 \sin h \frac{1 + \cos v}{2} = 0\tag{2.132}$$

where $\epsilon = 1/I\sqrt{\beta}$ is the small parameter, and time has been redefined as $\tau = I\sqrt{\beta}t$.

In this limit, the solution for (2.131) is of the form $v = \tau + \mathcal{O}(\epsilon^2)$ and (2.132) becomes

$$\frac{d^2h}{d\tau^2} + \epsilon \frac{1}{\sqrt{\beta}} \frac{dh}{d\tau} + \epsilon^2 \sin h \frac{1 + \cos \tau}{2} = 0$$

with a stable fixed point at $h^* = 0$. Then, (2.131) is just the single junction equation in the whirling limit.

Analytical approximation for the intermediate branch

We consider now the intermediate regime of interest. Figure 2-31 shows the numerical solution of the reduced system in the intermediate branch. We observe that this solution is indeed *another* whirling mode since the basic solution for the vertical junctions can be well approximated by $\phi^{V*} = \omega t$, plus a small modulation. However, the voltage in Figure 2-28 is roughly half of the voltage for the usual whirling branch. Since the voltage is equal to the frequency in certain reduced units, the frequency ω of this intermediate step is *not* given by $I\sqrt{\beta}$, as for the usual whirling mode. Moreover, in this case the horizontal junctions oscillate with a non negligible amplitude and a frequency that is half of the driving frequency.

The regularity of the numerical solutions for v and h , Figure 2-31, suggests an analytical form for the solution, which would not be obvious if the original variables ϕ_1^H and ϕ_1^V from the full system were considered. We assume a solution of the reduced system 2.128 of the form:

$$\begin{aligned} v^*(t) &= \phi_0 + \omega t + A \cos \omega t \\ h^*(t) &= \alpha \sin \left(\frac{\omega}{2} t + \delta \right). \end{aligned} \quad (2.133)$$

This is the simplest *ansatz* compatible with the numerics. The actual Fourier analysis of the solutions shows that v has an infinite number of even Fourier components of the basic frequency $\omega/2$. Similarly, h can be written as a Fourier series where only

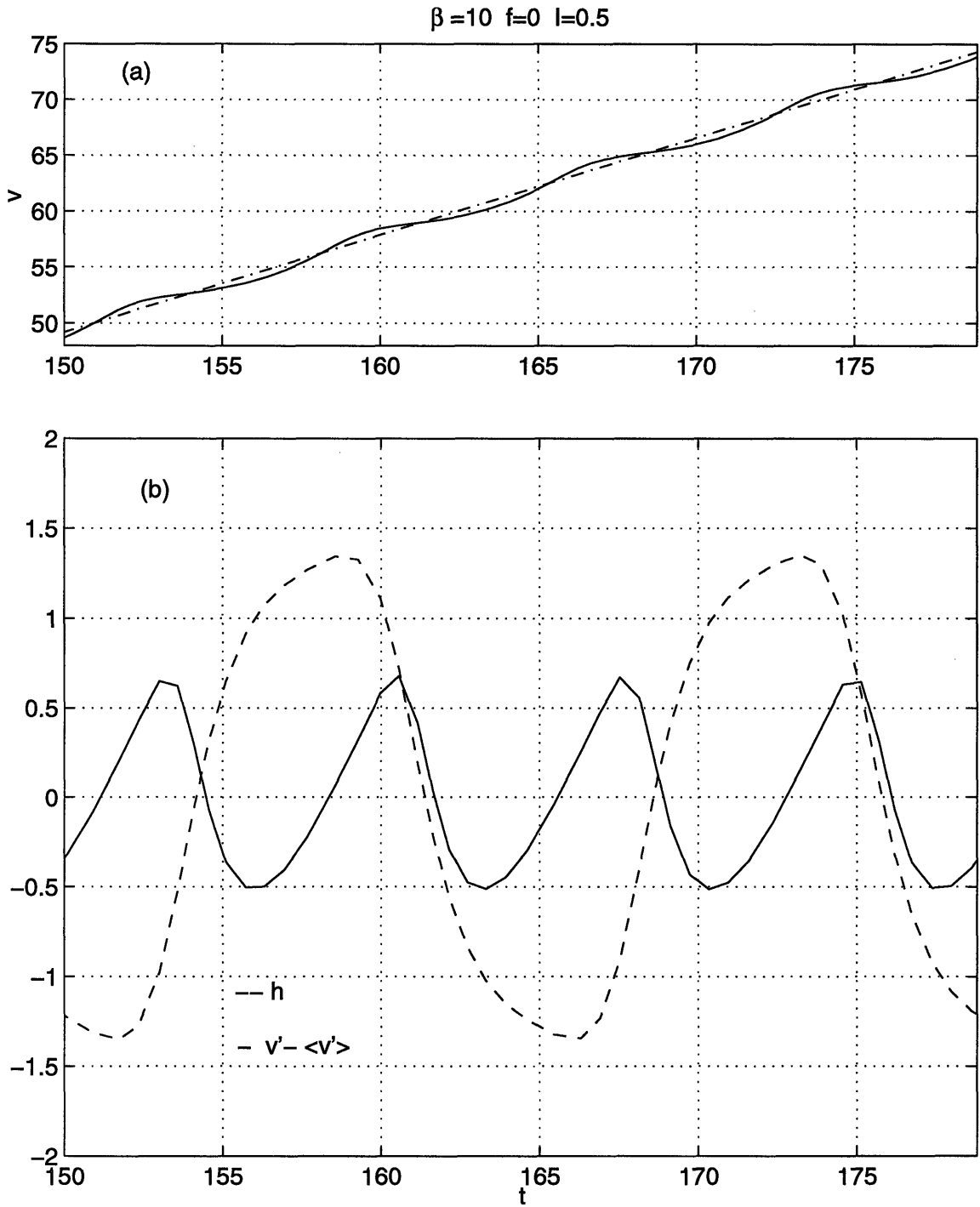


Figure 2-31: Numerical simulation of the reduced system (2.128): (a) $v(t)$, solid line, and zeroth order linear approximation $v_0(t) = \omega t + \phi_0$, dotted line; (b) $h(t)$, dashed line, and $v(t) - v_0(t)$, solid line, obtained from (a). Graph (a) shows that the intermediate step is well described by a whirling mode with a small superimposed modulation. In (b) the superimposed modulation and the oscillation of the horizontal junctions are represented. They can be well approximated with one harmonic.

odd multiples of $\omega/2$ are present. However, the weight of higher harmonics is not significant and, consequently, we only consider first harmonics.

In short, the assumed solution (2.133) is, in effect, another whirling mode: the vertical junctions rotate with almost constant ω and have a small superimposed harmonic oscillation of the same frequency and amplitude A . In addition, the horizontal junctions undergo out-of-phase oscillations of amplitude α with frequency *half* the driving ω .

The five parameters $(\phi_0, \omega, A, \alpha, \delta)$ are to be determined by substituting in the system's equations (2.128) and using the method of harmonic balance. Furthermore, the system depends parametrically on β and I . Our objective is to explain the dependence of ω on β and I . Since ω is directly proportional to the average voltage, this will give the $I - V$ characteristic for this solution. In addition, A and α serve as approximations for the amplitude of the oscillations in the vertical and horizontal junctions, respectively.

The analytical procedure consists of three steps:

1. Begin by changing variables

$$2z \equiv \phi_0 + \omega t + \pi; \quad v' \equiv \frac{dv}{dz} \quad (2.134)$$

and rewriting the system as

$$\frac{\omega^2}{4}v'' + \frac{\omega}{2\sqrt{\beta}}v' + \sin v [\cos h] = I \quad (2.135)$$

$$\frac{\omega^2}{4}h'' + \frac{\omega}{2\sqrt{\beta}}h' + \sin h \left[\frac{1 + \cos v}{2} \right] = 0. \quad (2.136)$$

The assumed solution (2.133) becomes then:

$$v^*(z) = 2z - \pi - A \cos(2z - \phi_0) \quad (2.137)$$

$$h^*(z) = \alpha \sin(z + \varphi) \quad (2.138)$$

where $\varphi = \delta + (\pi - \phi_0)/2$.

2. Standard expansions of sinusoidals of sinusoidals in terms of Bessel functions [1] yield the following expressions needed for our analytical approximation:

$$\begin{aligned}\cos v^* &= -J_0(A) \cos 2z \\ &- \sum_{k=1}^{\infty} (-1)^k J_{2k}(A) \{\cos[(2k-1)2z - 2k\phi_0] + \cos[(2k+1)2z - 2k\phi_0]\} \\ &- \sum_{k=0}^{\infty} (-1)^k J_{2k+1}(A) \{\sin[(2k+2)2z - (2k+1)\phi_0] + \sin[-4kz + (2k+1)\phi_0]\},\end{aligned}$$

and

$$\sin h^* = 2 \sum_{k=0}^{\infty} J_{2k+1}(\alpha) \sin[(2k+1)(z + \varphi)],$$

and

$$\begin{aligned}\sin v^* &= -J_0(A) \sin 2z \\ &- \sum_{k=1}^{\infty} (-1)^k J_{2k}(A) \{\sin[(2k+1)2z - 2k\phi_0] - \sin[(2k-1)2z - 2k\phi_0]\} \\ &+ \sum_{k=0}^{\infty} (-1)^k J_{2k+1}(A) \{\cos[(2k+2)2z - (2k+1)\phi_0] + \cos[-4kz + (2k+1)\phi_0]\},\end{aligned}$$

and

$$\cos h^* = J_0(\alpha) + 2 \sum_{k=1}^{\infty} J_{2k}(\alpha) \cos[2k(z + \varphi)].$$

3. Use the method of **harmonic balance** to obtain an algebraic system of five equations for the five unknowns. This is done by substituting the expansions above in (2.135)- (2.136); grouping terms; neglecting second and higher harmonics in the expressions; and, finally, requiring that the equations be fulfilled to first harmonics. In all of this, we assume that A, α are small enough to disregard terms in $J_5(A), J_9(\alpha)$ and up. This procedure results in a system of five equations (three from the $\cos 2z, \sin 2z$ and independent terms in (2.135); the other two, from the $\cos z, \sin z$ terms in (2.136)) for our five unknowns which has to be solved numerically. Several solutions of the algebraic system exist, as

Branch	I	α	δ	ω	A	ϕ_0
(1)	0.55	1.889	-0.035	0.865	0.489	0.771
(2)	0.55	$\sim 10^{-26}$	-0.312	1.639	0.349	1.386
(3)	0.55	0.972	-0.304	1.318	0.409	1.328
(4)	0.55	3.527	-3.838	0.381	-1.046	-5.293
(5)	0.40	$\sim 10^{-13}$	-0.432	0.354	-2.268	2.127
(6)	0.40	$\sim 10^{-13}$	-0.058	0.229	-3.010	2.930

Table 2.2: Parameters ($\alpha, \delta, \omega, A, \phi_0$) of the assumed solution for the different branches of the approximated algebraic system with $\beta = 10$ and varying I . See Figure 2-33.

discussed below.

In Figure 2-32 and Table 2.2 we represent, for fixed $\beta = 10$ and varying I , the frequency ω and oscillation amplitudes A and α for different solutions of the approximate algebraic system. These results are representative for a range of β . The branches can be described as follows:

- Branch (2), the usual whirling branch, is indeed a solution of the system—in fact, it is the only solution as $I\sqrt{\beta} \gg 1$. It is characterized by whirling of the vertical junctions with frequency $\omega \simeq I\sqrt{\beta}$ with a small superimposed modulation $A \simeq 1/\omega^2$. Oscillations of the horizontal junctions are truly negligible ($\alpha \sim 0$). The numbers in Table 2.2 fully support this usual description.
- Branch (1) in Figure 2-32 corresponds to the intermediate branch observed in the numerics of the full system. This is a subharmonic whirling solution in which: the amplitude α of the oscillations of the horizontal junctions is large; there is a non-negligible oscillation A of the vertical junctions; the subharmonic whirling frequency ω is roughly half of what the driving “torque” produces in the usual whirling branch since some of the provided “energy” goes into the oscillation of the horizontal junctions. However, these never whirl, and thus $\langle \dot{\phi}^H \rangle \sim 0$, i.e. the voltage across the horizontal junctions is still negligible. An example of the solution is presented in Figure 2-33. Note the good overall agreement with the original solution of the reduced system with the same set of parameters in Figure 2-31.

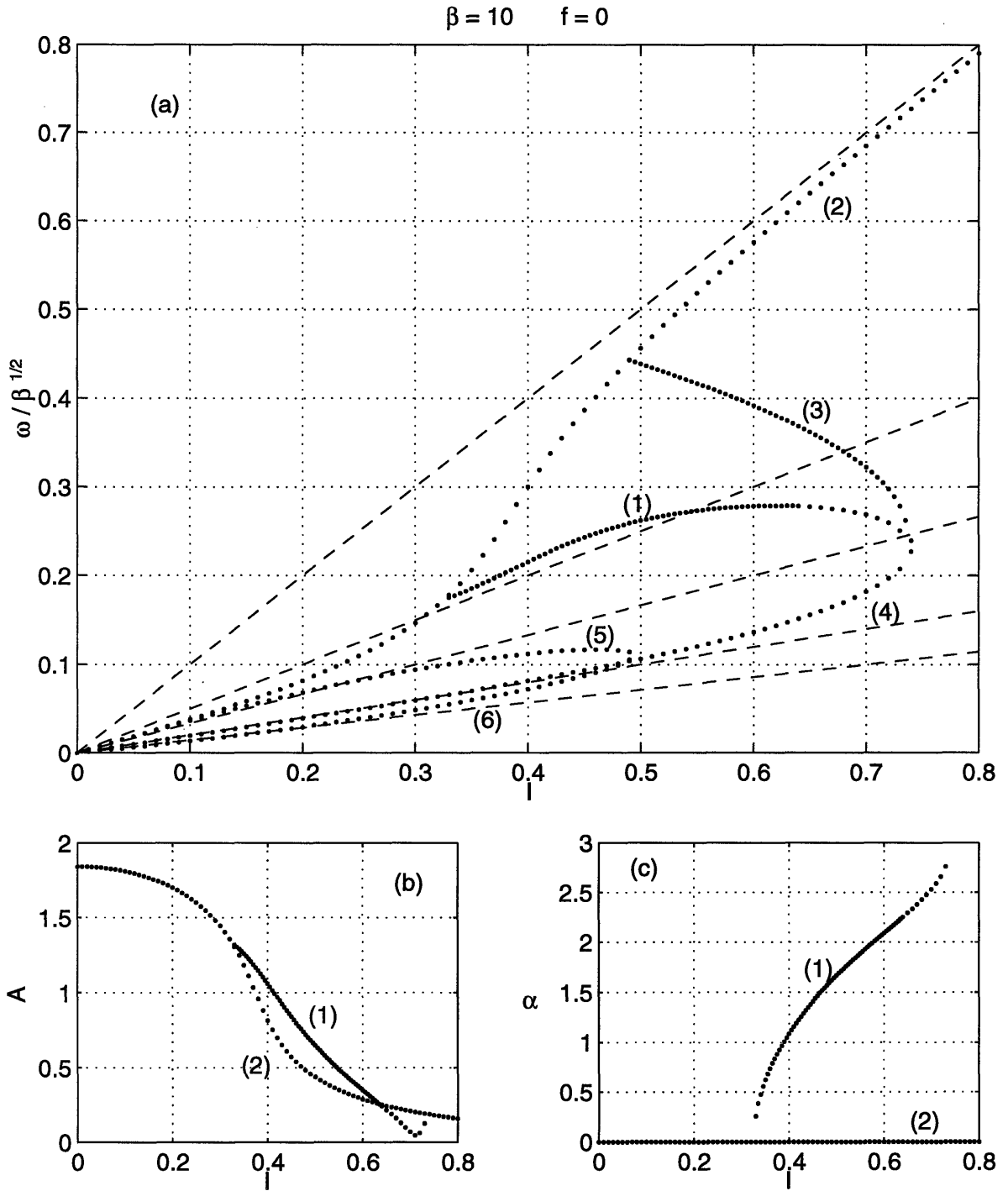


Figure 2-32: ω , A and α of different solutions of the approximate algebraic system for $\{v^*, h^*\}$ with $\beta = 10$. The different branches are explained in the text. Dashed lines in (a) are lines of slope 1, 1/2, 1/3, 1/5, 1/7

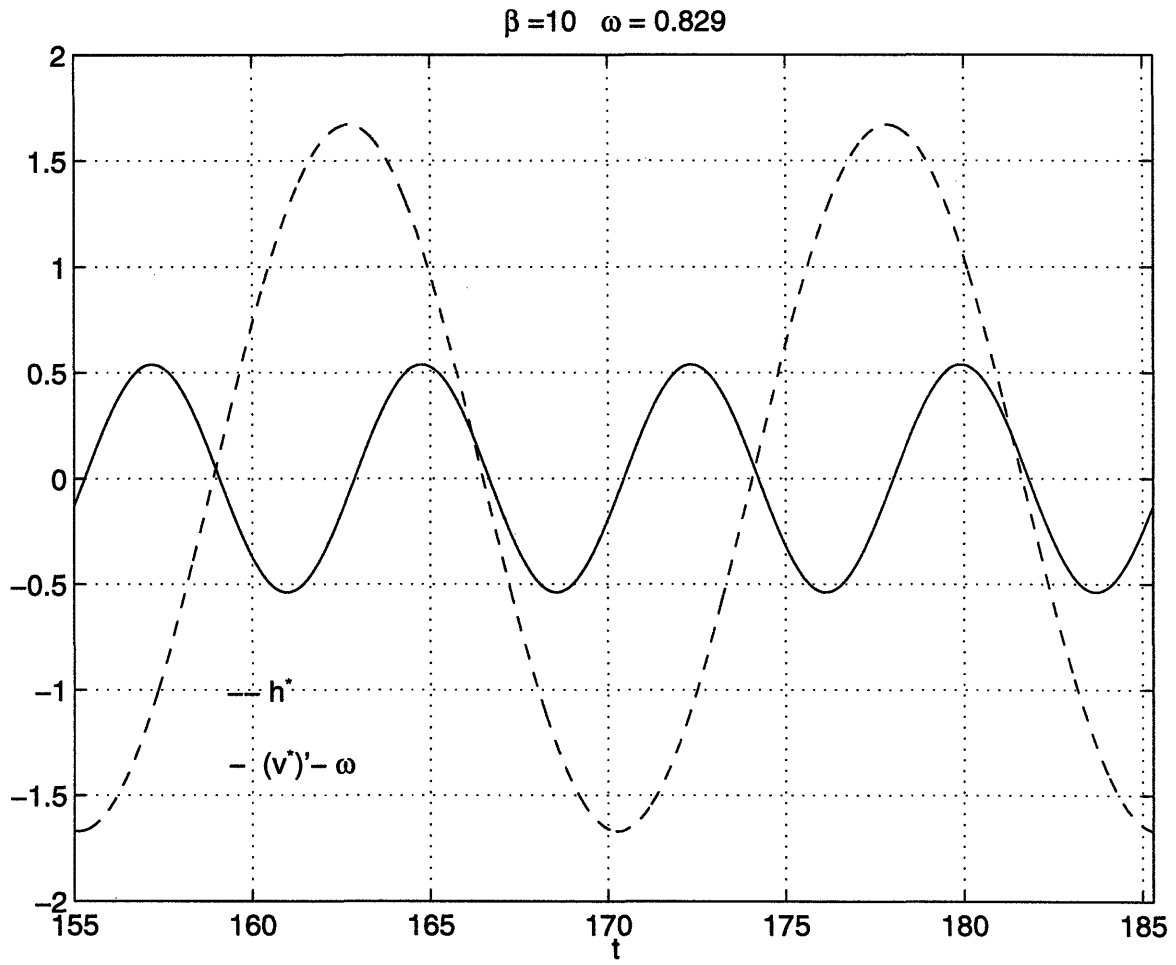


Figure 2-33: Approximated solution for subharmonic whirling branch, $\beta = 10$ $I = 0.5$. Compare to the solution of the reduced system in Figure 2-31 (b) for the same parameters

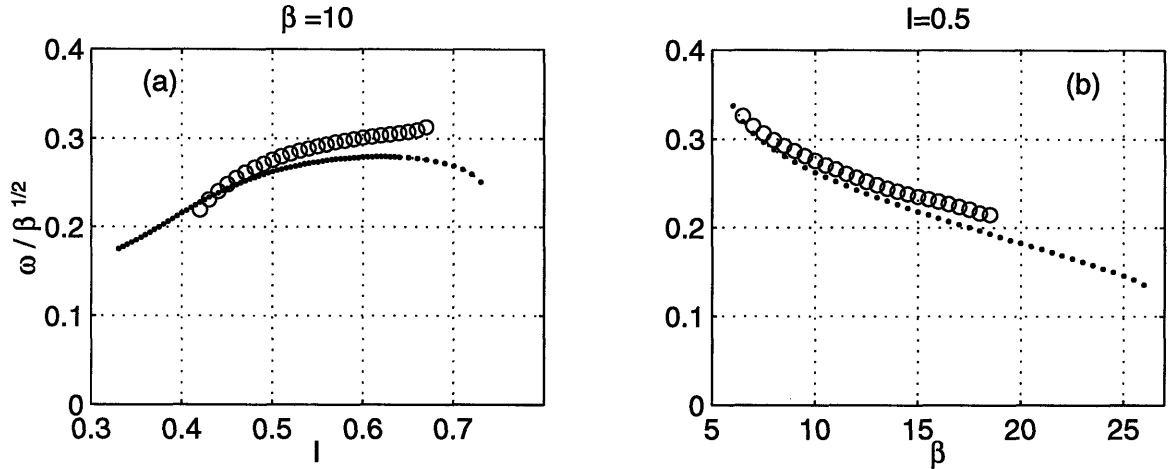


Figure 2-34: Frequency of the approximated(\cdots) and full(\circ) solutions for the intermediate branch of the reduced system: (a) vs. I at $\beta = 10$ and (b) vs. β at $I = 0.5$

To check the validity of the approximation method, we compare in Figure 2-34 the calculated frequencies for the approximated branch and the original numerical solution for varying β and I with good quantitative agreement. The approximate branch exists only for a range of β , as observed numerically. In conclusion, the characterization of the intermediate branch as a subharmonic whirling mode with large oscillations of some horizontal junctions and smaller modulation of the vertical junctions is in agreement with the numerics.

- Branch (3) in Figure 2-32 is related to the instability of the main whirling branch. It is another of the subharmonic branches in which the horizontal and vertical junctions oscillate appreciably. We present in Figure 2-35 numerical evidence which supports that the intersection of these two branches corresponds to the onset of instability for the whirling branch. In more physical terms, when the frequency of the whirling branch is equal (“resonates”) with that of a subharmonic branch where the horizontal junctions oscillate non-negligibly with half the frequency of the vertical ones, the main whirling branch becomes unstable and switches down to branch (1). However, the precise mechanism (be it based on existence, stability or energy arguments) remains to be studied.

This approach is to be compared to the one developed in Section 2.4.2 where

we related the instability of the whirling branch to the instability of Mathieu modes obtained by linearizing the equations. In that case, the method was more general and revealed a global mathematical mechanism for the instability of the whirling branch. However, because of the approximations involved, the quantitative predictions were not very accurate. The present description, although particular, seems to give an improved explanation of the observed numerical behavior.

The origin of both mechanisms is fundamentally the same: the resonance of the driving frequency with a characteristic frequency of the system causes the instability of the whirling mode. In the case of the intermediate step, the whirling branch with “silent” horizontal junctions “resonates” with the subharmonic modes where horizontal junctions are “active”. This is a particular case of the more general parametric instability picture developed in Section 2.4.2. In fact, the quantitative connection between the two approaches can be made more explicit. We observe that the interval of β for which the intermediate step appears, roughly $\beta \in [10, 18]$ as seen in Figure 2-34 (b), is approximately equal to the interval where the first parametric instability which the whirling mode encounters on its return path is caused by the resonance with the mode with $m = 4$ —see Figure 2-27(b). It is revealing that the wavelength of the intermediate step solution (Figure 2-29) is also equal to 4 cell lengths and the horizontal junctions can be described by a standing wave

$$\phi_j^H = u(\omega t) \sin\left(\frac{\pi}{2}(j - 2)\right)$$

which is equivalent to a wave with only the $m = 4$ mode excited, as given by (2.26).

Overall, this suggests the following sequence: As the current is decreased, the frequency of the whirling branch also decreases. When the driving frequency ω equals $2\omega_4$, the whirling solution becomes unstable due to the linear instability of the mode with $m = 4$. Thus, a new mode where this wavelength is the only

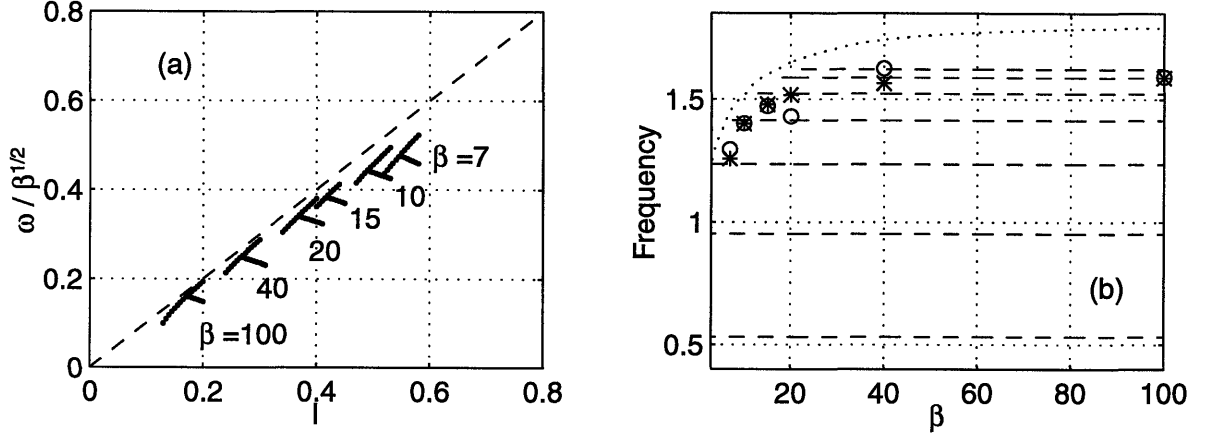


Figure 2-35: (a) Intersections of the subharmonic branch (3) with the main whirling branch (1) for different values of β . (b) Comparison of the numerically obtained repinning frequencies (o), above mentioned intersections (*), and Mathieu modes and associated instability intervals (- - , \cdots)

one, i.e. the intermediate subharmonic whirling mode, emerges as the stable solution of the system.

- Finally, the solutions of branches (4), (5) and (6) in Figure 2-32 are characterized by large modulations A and α and, thus, the approximations become worse. Nevertheless, it is noticeable that the slope of $\omega/\sqrt{\beta}$ is approximately given by I/n , with $n = 5, 3, 7$ respectively, thus emphasizing their subharmonic character.

One further step to confirm the validity of our approximation is the use of the approximate solutions as initial conditions for the full original system to observe if solutions of the proposed form exist. To this end, we first obtain the corresponding approximate phase configuration for the *full* system from (2.126) and (2.129). This is then used as the initial condition for the full dynamical system of $2n + 1$ second order differential equations (2.95)- (2.96). As expected, branches (2) and (1) evolve to the whirling and intermediate branches respectively. All other branches fall into one of the three already coexisting solutions: superconducting, whirling, intermediate. Since no new solution is observed when using branches (3)-(6) as initial conditions, we tentatively deduce that these branches are either artifacts of the approximations, or correspond to solutions of the full system which are unstable or with a small

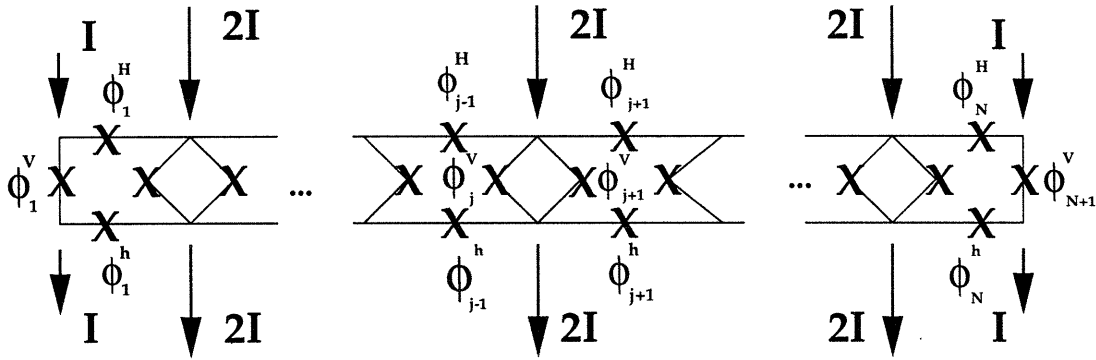


Figure 2-36: Diagram of superconducting device equivalent to the observed intermediate mode. This decimated ladder is intermediate between a square and triangular array

basin of attraction. Furthermore, a linear stability analysis of the five dimensional approximated system remains to be done in order to explain the observed jumps between branches in terms of stability or energy arguments.

We conclude by pointing out that the present mode of interest, in which the phases of the even horizontal junctions in both top and bottom rows are identically zero, is effectively equivalent to the physical device represented in Figure 2-36. This system is intermediate between a full square ladder and a triangular ladder array. Note that the triangular array can be obtained from a square ladder by removing all the even (odd) horizontal junctions in the top (bottom) row. Since these two most commonly used geometries have distinct properties and behavior, the proposed device could present interesting features of its own, regarding, for instance, vortex propagation. It could be also a realization where these subharmonic branches become observable.

In conclusion, the appearance of these modes illustrates the important role of the horizontal junctions in two dimensional Josephson Junction arrays. The physical constraints they introduce (via current conservation and fluxoid quantization) modify the behavior of the vertical junctions and allow the existence of new fully two dimensional modes. Observations, or analyses, which focus exclusively on vertical junctions need to effectively parametrize the presence of the horizontal links. Even then, a full two dimensional description of the modes is likely to be needed to explain the behavior of the arrays, especially in the intermediate, richer regimes.

2.4.4 Summary and discussion

We have presented in this section a thorough description of the whirling mode in ladder arrays in connection with the repinning transition. We began by obtaining an analytical approximation for the whirling solution, for any field f , both far from the edges and when edges are taken into account, to very good agreement with the numerics. The effect of the boundaries on the solution is of $\mathcal{O}(\omega^{-2})$ and, thus, almost negligible. When $f = 0$, the correction is zero to this order of the approximation.

A linear stability analysis around this approximate solution, in the line of a similar calculation introduced in [99], was performed to deduce the mechanism of the instability of the whirling branch. As a result, a dispersion relation which parametrizes the presence of the horizontal junctions was obtained. The first, but not only, effect of the presence of the horizontal junctions is the appearance of an effective inductance which couples the vertical junctions. This results from the fluxoid quantization restriction. The instability of the whirling solution is caused by parametric resonances of the whirling frequency with the characteristic frequencies of the modes of the array and is not a homoclinic-type bifurcation. The decrease of the repinning transition as the damping is increased is also accounted for within this approach as the high frequency resonances disappear due to the narrowing of the instability interval. Moreover, we explain the absence of the expected restabilization steps on the return path [99] in the numerics: the small value of the effective inductance introduced by the horizontal junctions produces a cascade of overlapping instabilities which renders them unobservable.

The important role of the horizontal junctions is fully displayed in a new intermediate step on the return path which was found for $f = 0$ and intermediate values of β . It was fully characterized as a subharmonic whirling branch where the horizontal junctions oscillate almost harmonically with non-negligible amplitude. By assuming a standing-wave form for the horizontal junctions, we were able to reduce the dynamical equations of this mode to a system of two coupled damped nonlinear pendula: one being externally driven and then driving the other. Moreover, an analytical ap-

proximation was derived for this reduced system through the method of harmonic balance. From this approximation, the $I - V$ dependence was predicted and checked satisfactorily with the numerics. The other possible solutions for the analytical system represent different subharmonic branches under the given restrictions. Although they do not appear in the dynamical simulations, they deserve a closer look in the future. For instance, numerical evidence suggests that the intersection of one of them with the main whirling branch explains well the observed repinning currents. Thus, the whirling branch becomes unstable when it resonates with a subharmonic solution where the horizontal junctions oscillate appreciably. In this light, the new intermediate step is the result of a special case of the parametric resonance whose excited mode generates a stable subharmonic solution. Indeed we proposed a new geometry for a device (a decimated ladder) intermediate between a triangular and a complete square ladder, where these and other effects could be observed. We conclude this discussion by noting in passing that other reduced systems have been proposed for the case $f = 1/2$ as an *ansatz* to simplify the system [75, 60]. We plan to investigate the connection with our system in the future.

Chapter 3

Two-dimensional Josephson junction arrays

3.1 Background

This chapter deals mainly with simulations of two-dimensional, square, open-ended Josephson junction arrays with perpendicular injection of current and in the presence of a magnetic field. For simplicity, all the simulations are performed in the limit of no inductances and zero temperature. Our main aim here is the compact characterization of the different dynamical regimes of these systems using the tools of nonlinear dynamics. In addition, we will consider the dependence of their behavior on two of the variable parameters of the physical system: the characteristic damping of each of the junctions, as given by the McCumber parameter β , and the perpendicular applied magnetic field, parametrized in terms of the frustration f . We restrict ourselves to this simplified system in order to extract physically meaningful conclusions. Thus, we do not investigate the dependence of the observables on temperature, self-induced fields, the number of cells of the array in the x and y directions, or other types of connectivity (e.g. triangular).

Review of experiments

All of these parameters, and more, have been explored in the considerable amount of experimental and theoretical work undertaken in the last fifteen years. As stated in the Introduction (Chapter 1), the interest in these systems stems from their potential technological applications mainly as high-frequency emitters [9], and their use as wave mixers and detectors [49] is also important. The old idea of employing these superconducting elements as memory circuits (due to their hysteretic behavior) has not delivered on its initial technological promise [27].

From a more fundamental point of view, these devices are closely related to other systems for which, in many cases, experiments are difficult. For instance, they can serve as controlled models for phenomena occurring in high- T_c superconductors. These are ceramic materials (perovskite oxides) which, in their processing and synthesis, form microcrystalline structures with numerous grain boundaries which act as natural weak junctions [43]. Thus, the understanding of the $I-V$ characteristics of Josephson junction arrays could be of great help to further our knowledge of the more complicated measurements in high- T_c superconductors [70, 52]. Even more fundamentally, some of these oxygen-deficient perovskites crystalize in highly anisotropic layered structures with the superconducting transport occurring fundamentally in planes separated by insulating sections [42]. Hence, they can be viewed as an intrinsic set of stacked quasi-continuous Josephson-junctions. Consequently, this line of research has pursued the simulation and fabrication of stacked continuous junctions [87, 64] and of stacked discrete one-dimensional parallel arrays [20]. Bridging the gap between stacks of one-dimensional systems and truly two-dimensional devices, recent experimental work [73] has explored the tunable crossover from one-dimensional to two-dimensional arrays.

In a different direction, Josephson junctions provide a good testing ground for fundamental concepts of Quantum and Statistical Mechanics which are at the heart of the description of these devices. The prediction by Kosterlitz-Thouless-Berezinskii [44] of the existence of a temperature- or field-induced phase transition has been the

object of several experiments [91, 88, 84, 72]. Similarly, the predictions from the theory of quantum vortices [23] have begun to be realized in the measurement of some interference effects [21].

Finally, the study of the classical regime of the array (where charging energies are negligible) has been experimentally rewarding. In this limit, the vortex can be considered as a classical particle which moves under the action of electromagnetic forces in a sinusoidal potential. The ground states of the system form flux lattices which begin to move in a flux-flow fashion similar to the one observed in continuous superconductors when random pinning centers are present [54]. In the case of underdamped arrays, when the current is increased further, row-switching events occur [92, 83] in which the voltage loss is restricted to certain rows in the array. This spatially non-homogeneous solutions have been observed experimentally with low-temperature scanning electron microscopy [47, 15]. Moreover, the observation of ballistic motion of vortices, which behave very much like a very massive particle with large inertia, in triangular arrays, where the intercell energy barriers are small [89], is the object of ongoing theoretical work and controversy.

Review of simulations

The experimental overview above stresses both the encouraging overall agreement between theory and experiments, and the need for some insight to guide the search for the optimization of specific applications within the huge space of experimental parameters. This void has been filled with numerical simulations, which provide the capability to concentrate on the effect on the behavior of some of the parameters. The important body of *numerical* work is validated by the existence of a good quantitative model (RCSJ) which faithfully reproduces the physical characteristics of the system. The body of *analytical* work is considerably smaller for two-dimensional arrays [101, 24, 53] due to the difficulty of reducing the dimensionality of the problem in any significant way. Simplifications to map the observed behavior of the arrays onto other well studied systems are also difficult.

The freedom, when performing numerical simulations, to select the approxima-

tions, or the limiting regimes, and to concentrate on different parameters and effects, has produced a rich and diverse literature which we review briefly. To that end, we summarize the main themes pursued, and the results obtained, through some relevant examples. Some of the topics investigated in the numerical literature include:

Influence of self-fields By taking into account the inductances of the problem (i.e. λ_{\perp} finite), self-fields are shown, among other effects, to alter the depinning current of the array and to introduce added asymmetries in the sequence of row-switching events [67, 66, 70, 52, 85, 17]. Most of the simulations in the rest of the literature do not include self-field effects since the computational cost is increased substantially.

Underdamped vs. overdamped dynamics These two cases represent different limiting behaviors with their own interesting characteristics. In the overdamped limit, the McCumber parameter β is taken to be zero, and the equations of the junctions become of first order. Thus, the inertia term is missing and neither row-switching nor hysteretic effects are easily observed. This limit is physically realizable in Nb-Al₂O_x-Nb junction arrays. Aluminum junction arrays, on the other hand, where the junctions are underdamped, show hysteresis and row-switching. Examples of simulations in overdamped arrays are found in [12, 22] while arrays with capacitive junctions have been studied in [66, 105].

Influence of temperature In addition to the deterministic simulations at $T = 0$, temperature can be introduced as a stochastic Langevin term in the dynamical equations. The presence of randomness in the system reveals chaotic behavior in certain regimes [7, 6, 22].

Influence of disorder In order to mimic more realistically the experimental setups, disorder is introduced in the system of equations in different manners: as random irregularities in the positions of the junctions [16]; as a random distribution of critical currents of the junctions [62]; or as disorder in both the critical currents and the resistances [48]. Similarly to the effects of a non-zero

temperature, the disorder uncovers complex properties. Domínguez [16] observed the appearance of a plastic flow phase just above the depinning current in overdamped *irregular* arrays with f integer. In that state, vortices flow in channels across the array before entering a phase of homogeneous flow. Under completely different considerations, Octavio *et al.* [62] concluded that the synchronized states in two-dimensional arrays are more stable under the presence of disorder than the corresponding coherent oscillations in series arrays. Even more surprisingly, Landberg *et al.* [48] propose controlled disorder as a means to *enhance* frequency-locking in arrays.

Influence of the geometry of the array Different topologies and connectivities of the arrays have been used to explore distinct effects. One of the examples where the most common square geometry was not used is [104], where simulations of triangular arrays were performed in search of ballistic motion of vortices.

AC-driven vs. DC-driven The presence of an external driving frequency produces additional resonances between the external and characteristic frequencies (Shapiro steps) which have been extensively investigated [103, 68]. Similar effects appear when the arrays are studied in the presence of an oscillating magnetic field [6].

Static vs. dynamic calculations Static calculations are performed, in the spirit of the statistical mechanical principles, by searching for the ground states in the complicated phase space of the system. The procedure commonly used applies standard minimization algorithms based on Monte Carlo or simulated annealing techniques [82, 81] or more advanced improved Newton's methods [67]. In short, static calculations are based on the minimization of the free energy of the system, while dynamical calculations simulate the time evolution of the system from the equations of motion.

Common to all these studies, a series of physical pictures serve to present the information gathered from the simulations. The most common are: the concept of

vortex propagation in a viscous medium [32, 4, 93]; the analysis of spatiotemporal structures in terms of flux lattices and defects [22, 29, 74, 54, 53]; the pendulum analogy and the reduced mechanical systems [99, 60, 75, 100]; the connection between the continuum and discrete models [93, 64]; and the reduction of the system to smaller tractable units which are then coupled as a means to reproduce the larger system [101, 24, 87, 99]. We will also use simulations to gain knowledge about the system and will represent our results partly in terms of this well-known notation and, more importantly, with concepts and methods of nonlinear dynamics which have not been used in this context.

The chapter is organized as follows: In the first section we introduce the physical description of the system, its mathematical formulation, the general notation, and an explicit enumeration of the approximations introduced in the model. Furthermore, we describe the mathematical methods used to characterize the system beyond the standard time and space averaged I - V characteristics. In the second and third sections, we investigate, respectively, the dynamical regimes and physical observables of underdamped (β large) and overdamped ($\beta = 0$) arrays of junctions. In particular, we explore the interplay between the formulations in terms of localized excitations and of extended waves in the system; and relate the collective behavior of the array to the motion of the individual junctions. For the underdamped case, we also establish the connection of the two-dimensional results with those obtained for ladder arrays, which we studied as an intermediate system towards the fully two-dimensional case. Since the dynamical regimes in both systems correspond to similar physical pictures, certain solutions of the ladder can be used to describe the regimes of two-dimensional arrays and thus lead to some quantitative predictions. Finally, we characterize the overdamped system numerically and relate the main features of its I - V curves to other systems where flux-flow phenomena are dominant [74].

3.2 Introduction: model and methods

3.2.1 Physical description and model equations

We begin by summarizing the physical features of two-dimensional arrays and introducing the mathematical formulation for their modeling. Much of this section is analogous to Section 2.2.1 for the ladder array, to which we refer the reader for a more detailed account of some of the physical concepts underlying the equations. However, the present system's greater complexity and absence of significant simplifying constraints require the introduction of a more general and compact matrix formulation [66].

Consider an $N \times M$ open-ended square array of Josephson junctions. The system, shown in Figure 3-1 together with its basic cell, is constituted by $N + 1$ rows and $M + 1$ columns of superconducting islands, each of them weakly connected to its four neighbours through Josephson junctions. A uniform dc-current is injected in the y direction in each of the islands at the top row and extracted from the bottom. The right and left boundaries remain free. In addition, an external magnetic field \mathbf{B}_{ext} can be applied perpendicularly to the xy -plane which contains the array.

As explained when studying the ladder array, each island is described by a phase $\Theta_{i,j}$, and each junction by a gauge invariant phase difference $\phi_{i,j}$ given by (2.1). From that definition and the notation introduced in Figure 3-1(b) we obtain the following expressions for the phases of the vertical and horizontal junctions in the array:

$$\phi_{i,j}^V = \Theta_{i,j} - \Theta_{i,j+1} - \frac{2\pi}{\Phi_0} \int_{(i,j)}^{(i,j+1)} \mathbf{A} \cdot d\mathbf{l} \quad (3.1)$$

$$\phi_{i,j}^H = \Theta_{i,j} - \Theta_{i+1,j} - \frac{2\pi}{\Phi_0} \int_{(i,j)}^{(i+1,j)} \mathbf{A} \cdot d\mathbf{l} \quad (3.2)$$

where \mathbf{A} is the vector potential of the *total* magnetic field \mathbf{B} through the array.

Following a counterclockwise closed path in cell (i, j) , shown in Figure 3-1, the winding of the phases on the islands gives

$$(\Theta_{i,j} - \Theta_{i,j+1}) + (\Theta_{i,j+1} - \Theta_{i+1,j+1}) - (\Theta_{i+1,j} - \Theta_{i+1,j+1}) - (\Theta_{i,j} - \Theta_{i+1,j}) =$$

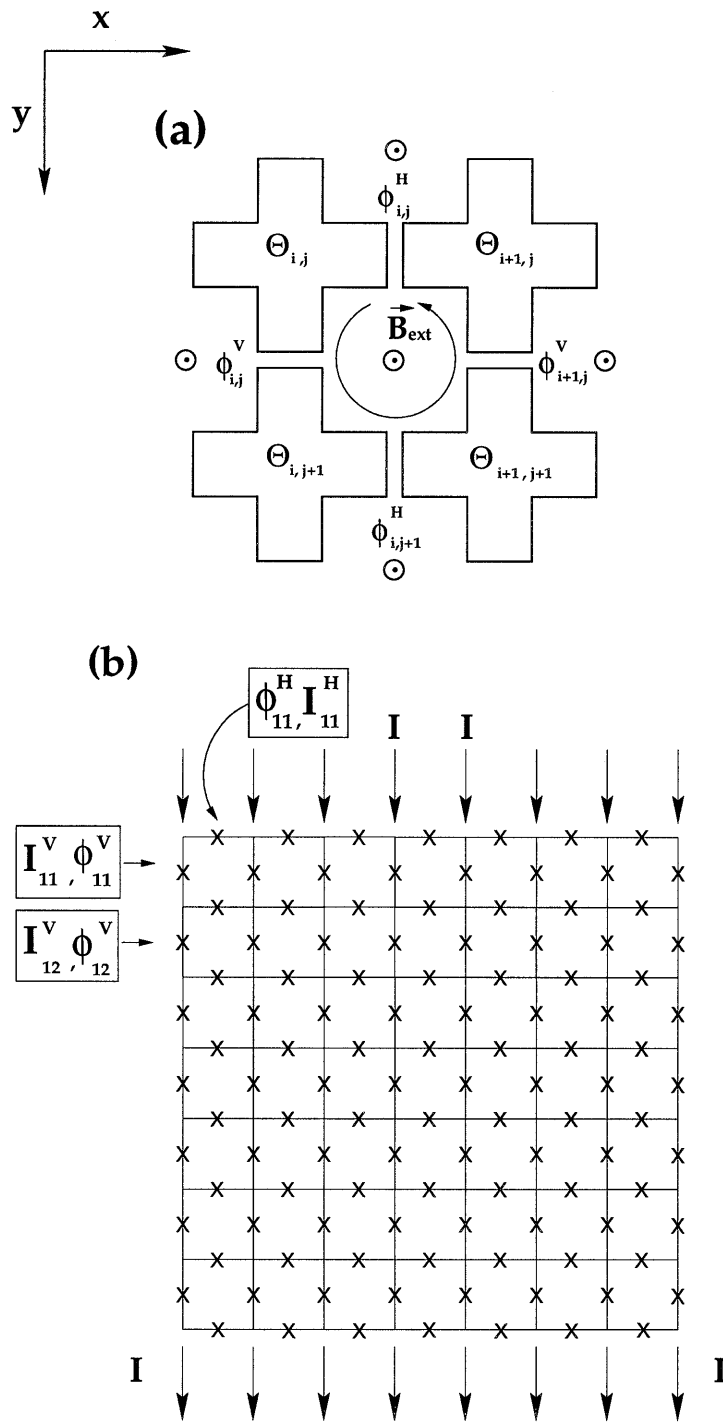


Figure 3-1: (a) Cell of the 2-D array formed by four superconducting islands, with the corresponding phase $\Theta_{i,j}$ weakly linked to the four nearest neighbors forming four junctions denoted with a gauge invariant phase difference $\phi_{i,j}$. (b) Schematic of a 7×7 array with free boundaries and current injection from top to bottom. Branch variables $I_{i,j}$ and $\phi_{i,j}$ are defined in the figure.

$$\phi_{i,j}^V + \phi_{i,j+1}^H - \phi_{i+1,j}^V - \phi_{i,j}^H + \frac{2\pi}{\Phi_0} \oint \mathbf{A} \cdot d\mathbf{l} \quad (3.3)$$

which yields the *fluxoid quantization* condition for the cell

$$\sum_{(i,j)}^{\rightarrow} \phi = \phi_{i,j}^V + \phi_{i,j+1}^H - \phi_{i+1,j}^V - \phi_{i,j}^H = 2\pi \left(n_{i,j} - \frac{\Phi}{\Phi_0} \right) \quad (3.4)$$

where $n_{i,j}$ is an integer and Φ is the total magnetic flux through the array whose cell area is taken to be unity. The symbol $\sum_{(i,j)}^{\rightarrow}$ denotes an oriented sum around cell (i, j) . To obtain (3.4), the univaluedness of the phase Θ –up to integer times 2π – as well as Stokes' theorem have been invoked. Also, the total magnetic flux Φ results from two contributions: the flux of the external field perpendicular to the array, and the flux produced by the self-fields caused by the circulating currents in the system.

This set of $N \times M$ equations (3.4), one per cell, will be used to generate the governing equations together with other relations obtained from:

1. Kirchoff's law: conservation of current at each node

$$I_{i-1,j}^H + I_{i,j-1}^V = I_{i,j}^V + I_{i,j}^H. \quad (3.5)$$

2. RCSJ model with constant resistance (2.5)-(2.8) for each of the Josephson junctions

$$I_{i,j} = \ddot{\phi}_{i,j} + \frac{1}{\sqrt{\beta}} \dot{\phi}_{i,j} + \sin \phi_{i,j} = \mathcal{N}(\phi_{i,j}) \quad (3.6)$$

or, equivalently,

$$I_{i,j} = \beta \phi_{i,j}'' + \phi_{i,j}' + \sin \phi_{i,j}, \quad (3.7)$$

where $\phi' = d\phi/d\tau_{num} = \dot{\phi}/\sqrt{\beta}$. Here the current is measured in units of I_c , β is the McCumber parameter and \mathcal{N} is a nonlinear operator. Thus the time evolution of each junction strictly follows the equation of a forced damped nonlinear pendulum.

These equations, which formalize the physical description of the system, can be recast into compact matrix form following standard notation from circuit theory [14,

66] and linear algebra [77]. To that end, we introduce the following definitions for the array of $N \times M$ cells in Figure 3-1:

- Number of nodes (islands): $S = (M + 1)(N + 1)$.
 Number of edges: $E = M(N + 1) + N(M + 1)$.
 Number of cells: $C = M N$
- Vector of phases of the islands: $\vec{\Theta}_{S \times 1}$.
 Vector of phases of the junctions: $\vec{\phi}_{E \times 1}$.
- Node current source vector: $\vec{I}_{S \times 1}^{ext}$. Zero for all islands except for those in the top row, where current is injected (source of intensity $+I$), and for the nodes in the bottom, where the current is extracted (sink of intensity $-I$).
 Branch current vector: $\vec{I}_{E \times 1}^b$.
 Mesh current vector: $\vec{I}_{C \times 1}^m$. Circulating current associated with each cell as a counterclockwise loop is described.
- Connectivity matrix: $A_{E \times S}$. This is the topology matrix which takes into account the geometrical connections between nodes. Translates node variables into branch variables (node-to-branch) and is equivalent to a node sum operator.
- Mesh matrix: $M_{C \times E}$. This is the edge-to-cell matrix. Relates the edge variables to a counterclockwise loop around a cell, i.e. equivalent to a cell sum operator like $\sum_{(i,j)} \vec{\tau}_{(i,j)}$ introduced in (3.4) .

The formulation is then simplified considerably:

- Equation (3.4) becomes

$$M \vec{\phi} = 2\pi \left(\vec{n} - \frac{\vec{\Phi}}{\Phi_0} \right) \quad (3.8)$$

where $\vec{n}_{C \times 1}$ is a vector over cells which contains integers $n_{i,j}$ associated with the existence of topological vortices on each cell, and $\vec{\Phi}_{C \times 1}$ is the vector of cell fluxes.

- Equation (3.5) becomes

$$A^T \vec{I}^b = \vec{I}^{ext} \quad (3.9)$$

which establishes the balance of currents in each node.

- Equation (3.6) becomes

$$\vec{I}^b = \mathcal{N}(\vec{\phi}). \quad (3.10)$$

The total flux on each cell $\vec{\Phi}$ can be separated into two parts

$$\vec{\Phi} = \vec{\Phi}^{ext} + \vec{\Phi}^{ind} \quad (3.11)$$

which we define as follows:

1. Flux of the applied constant field, which we parametrize in terms of the constant frustration f –i.e. in fractions of the quantum of flux Φ_0 ,

$$\vec{\Phi}^{ext} = \vec{f}\Phi_0$$

where $\vec{f}_{C \times 1}$ is a constant vector with all elements equal to f .

2. Flux of the induced magnetic field, produced by the circulating currents in the array \vec{I}^m and given by

$$\vec{\Phi}^{ind} = L^m \vec{I}^m$$

where $L^m_{C \times C}$ is the cell-to-cell inductance matrix.

Therefore, the fluxoid quantization (3.8) can be written as:

$$M\vec{\phi} + \frac{1}{\lambda_\perp} L^m \vec{I}^m = 2\pi(\vec{n} - \vec{f}) \quad (3.12)$$

where $\lambda_\perp = \Phi_0/(2\pi I_c \mu_0)$. In our simulations, however, we have considered only the limit $\lambda_\perp \rightarrow \infty$, where self-fields are negligible and, thus, the total flux is only produced by the external applied field. As discussed for the case of ladder arrays, this limit is physically realizable in aluminum arrays with large normal resistance and large λ_\perp .

With this approximation, (3.8) becomes

$$M\vec{\phi} = 2\pi(\vec{n} - \vec{f}) \quad (3.13)$$

where \vec{n} can be put to zero without loss of generality. This implies that

$$\mathbf{B} = \mathbf{B}_{ext} = f\Phi_0 \hat{z}. \quad (3.14)$$

with an associated vector potential \mathbf{A}_{ext} such that

$$\nabla \times \mathbf{A}_{ext} = \mathbf{B}_{ext}$$

For simplicity of the calculations we choose a Landau gauge where

$$\mathbf{A}_{ext} = f\Phi_0 y \hat{x}$$

such that equations (3.1)-(3.2) can be written as

$$\vec{\phi} = A \vec{\Theta} - \vec{\eta} \quad (3.15)$$

where A is the connectivity matrix and $\vec{\eta}_{E \times 1}$, an edge-vector, has value zero for all the vertical edges and value $2\pi f j$ for all the horizontal edges in row j .

We are finally in a position to write the system of governing equations in an operationally efficient form:

$$\begin{cases} \vec{z} = \vec{\Theta}' \\ \vec{z}' = \frac{1}{\beta} [(A^T A)^{-1} \{ \vec{I}^{ext} - A^T \sin(A\vec{\Theta} - \vec{\eta}) \} - \vec{z}] \end{cases} \quad (3.16)$$

which follows directly from (3.7), (3.9), (3.10) and (3.15).

The time evolution of the physical system is obtained from the solution of this system of equations beginning from a given initial condition of the phases and derivatives of the phases $\{\vec{\Theta}_0, \vec{\Theta}'_0\}$. The number of degrees of freedom of the system of coupled

differential equations is $2(S - 1) = 2(M + 1)(N + 1) - 2$, since one of the nodes is grounded to eliminate the redundancy of the phases, thus allowing the inversion of $A^T A$. It is easy to understand that the computational cost of numerical integration increases rapidly and the simulation of large arrays requires large computational resources.

This system of equations corresponds to a strict mechanical analogue of our system: a square lattice of coupled damped nonlinear pendula, forced by an external torque I , with open ends and with a frustration f . This analogy of each junction as a pendulum, will be exploited in our analysis of the behavior of the arrays under variation of the damping β , torque I , or frustration f .

3.2.2 Numerical analysis of simulated I - V characteristics

The measurement of $\langle V \rangle$, the dc-voltage difference between top and bottom rows of a two-dimensional array, as a function of the injected current I constitutes its I - V characteristic. This is one of the standard experimental techniques to study how the dc behavior of the arrays changes with the variation of external parameters like the applied magnetic field f or the temperature T , which modifies λ_{\perp} and β . The I - V curve also serves to investigate the dependence on other intrinsic properties of the array like its extension in the x and y directions or the material of the junctions. In short, they are a first diagnostic for the relevant parameters which affect the design of technological applications derived from these superconducting arrays.

The existence of multiple interdependent experimental variables, and the contradicting effects they produce on the fundamental parameters of the equations, make clear conclusions and simple physical pictures difficult to extract from the experiments. Thus, numerical simulations provide a good substitute to obtain precise and separate information about the dependence of the dc behavior on those variables. To this end, and with the aim of clarity, we consider a simplified scenario where the temperature is zero, self-fields are neglected ($\lambda_{\perp} \rightarrow \infty$) and the size of the array is fixed to be 7×7 . Under these simplifications, we study the f dependence of the I - V characteristics of underdamped ($\beta = 10$) and overdamped ($\beta = 0$) arrays.

The simulated I - V curves, which reproduce similar experimental measurements reasonably, are obtained by numerically integrating the system of governing equations (3.16). The integration is performed with an Adams-based algorithm [67] to obtain the time variation of the phases and phase derivatives $\{\vec{\Theta}_t, \vec{\dot{\Theta}}_t\}$ from a given initial condition. From those, we calculate the *measurable* dc-voltage given by (2.21)

$$\langle V \rangle = I_c R \frac{\overline{\langle \dot{\phi}_j(t) \rangle}}{\sqrt{\beta}} \quad (3.17)$$

where $\dot{\phi}_j$ is averaged both in time $\overline{\dot{\phi}}$ and in space $\langle \phi \rangle$ over the complete array. For a given pair of parameters $\{f, \beta\}$, $\langle V \rangle$ is calculated as a function of I to give the numerical I - V characteristic. The numerical simulation begins from $I = 0$, with

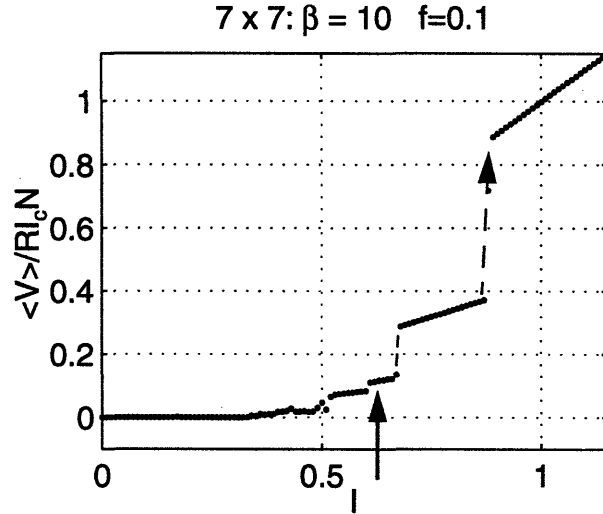


Figure 3-2: Direct path of the I - V characteristic of a 7×7 two-dimensional array with $\beta=10$ and $f = 0.1$. The corresponding spatially extended I - V is shown in Figure 3-3. In Figures 3-4 and 3-5, we depict the space-time evolution of the point marked with the solid arrow, $I = 0.64$.

the initial condition that phases and phase derivatives are zero, and the current is swept up in small increments. An example of the direct path (“up”) of an I - V curve is shown in Figure 3-2. Even in this simplified system, and with the rough probing tool that the I - V characteristic is, we can already observe the complicated landscape of regimes, critical currents and hysteretic cycles that this physical system supports. To gain some insight into the behavior of the system, we unravel the compressed information contained in those graphs by considering the spatio-temporal solutions which originate them. Therefore, we summarize now the numerical methods and the notation which will be used to characterize the dynamical regimes of the system. All refer to the example presented in Figure 3-2.

First, it is helpful to study the time-averaged but spatially extended frequency of all the junctions in the array $\bar{\phi}_{i,j}$ as a function of the current I , i.e. the *spatially extended* I - V . We choose to represent it as a 3-D plot where the index of the junction, as given in Figure 3-3(a), is placed in the x -axis, i.e. the x -axis is a juxtaposition of the rows of the array. Figure 3-3(b) depicts the spatially extended I - V for the example of Figure 3-2. Note that that I - V curve is indeed the result of averaging Figure 3-3(b) along the x -axis. The advantage of the spatially extended I - V is readily

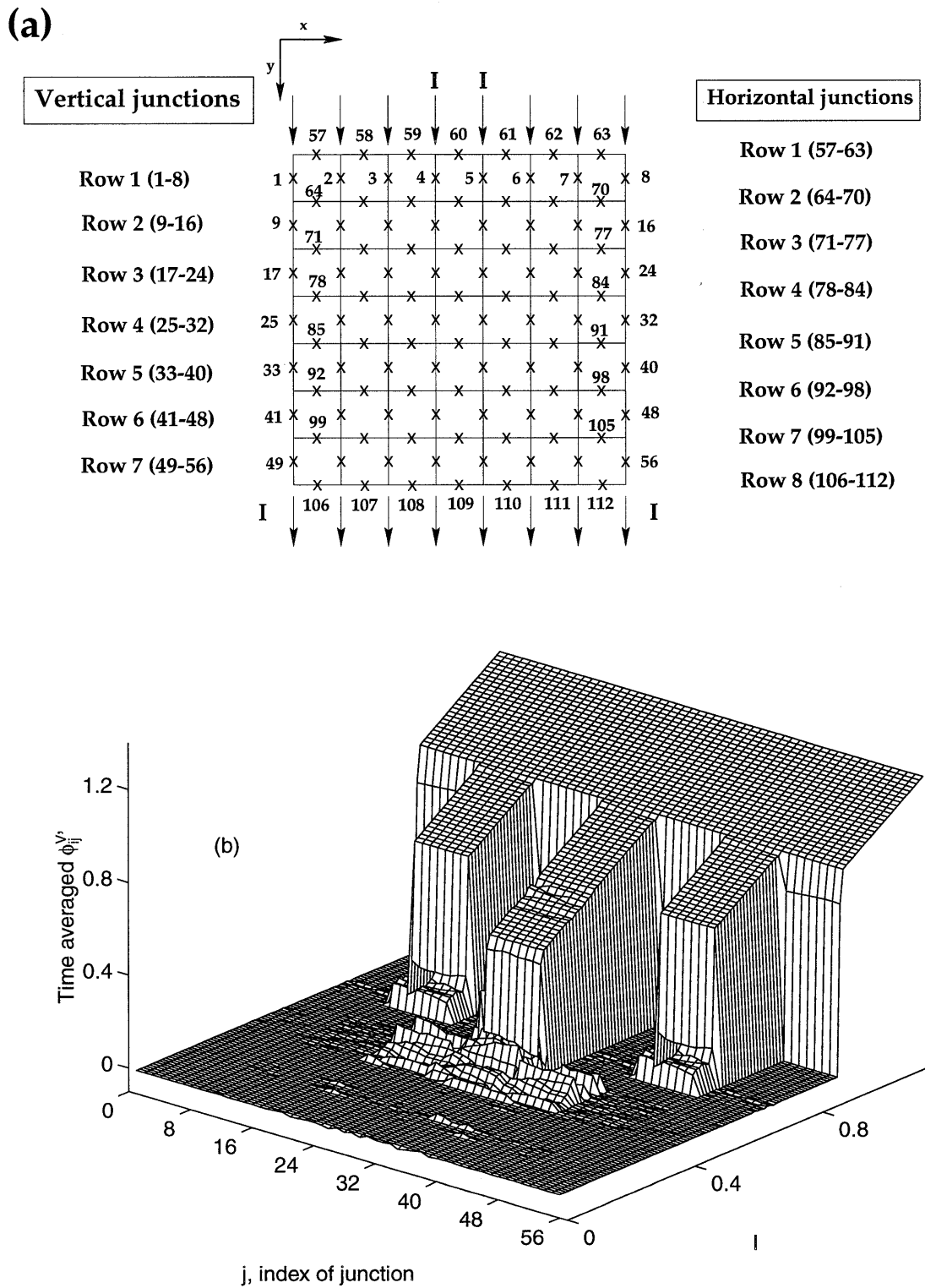


Figure 3-3: (a) Indexing of junctions in a 7×7 square array. (b) Spatially extended I - V for the vertical junctions of the example presented in Figure 3-2 ($\beta = 10$, $f = 0.1$). Consecutive rows of vertical junctions are juxtaposed along the x -axis of the graph, following the indexation introduced in (a).

observable from the figure: it helps to elucidate the existence of spatially inhomogeneous solutions, which are characteristic of these arrays.

More detailed information can be obtained about a specific point of the $I - V$ curve by analyzing the spatio-temporal solution associated with it. Note that the only information from the solution in the $I - V$ curve is its time and space averaged frequency, while, in fact, the simulations provide the time evolution of all the phases and their derivatives. A convenient way to summarize these data is in a *space-time* diagram of the solution like the one shown in Figure 3-4(a) which corresponds to the point marked with the arrow in the $I - V$ diagram of Figure 3-2. The space-time diagram is a contour plot of $\phi_{i,j}'(t)$ and serves to study the propagation of waveforms in the array. In effect, this is a compact way of representing an animation of the system. Both the average speed and the non-uniformity of the propagation of travelling wave solutions can be extrapolated from the study of these graphs, as will be discussed below. Similarly, the periodicity and the space symmetry of the solution become apparent from their examination.

In addition, the specific time evolution of each junction can be investigated through its *phase portrait*, i.e. the graph of $\phi'(t)$ vs. $\phi(t)$. In this respect we recall the analogy of the junction to a nonlinear pendulum and trace the motion that the pendulum describes. In Figure 3-5, we depict the three types of motion found in the junctions of these arrays:

1. Figure A corresponds to a *libration*. The pendulum oscillates around its equilibrium position with its phase always contained between $[0, 2\pi)$, i.e. it does not “whirl” over the top. Moreover, the complicated motion is still periodic. It is important to note also that, for this junction, $\overline{\phi'} \simeq 0$. Thus the voltage drop across the junction is zero and the junction remains superconducting.
2. Figure B shows a *whirling* junction, for which the pendulum goes over the top periodically. Here, $\phi'(t)$ is roughly constant, which implies an almost harmonic oscillation and a finite dc-voltage in this junction. This motion is qualitatively equivalent to the running periodic solution of the single junction.

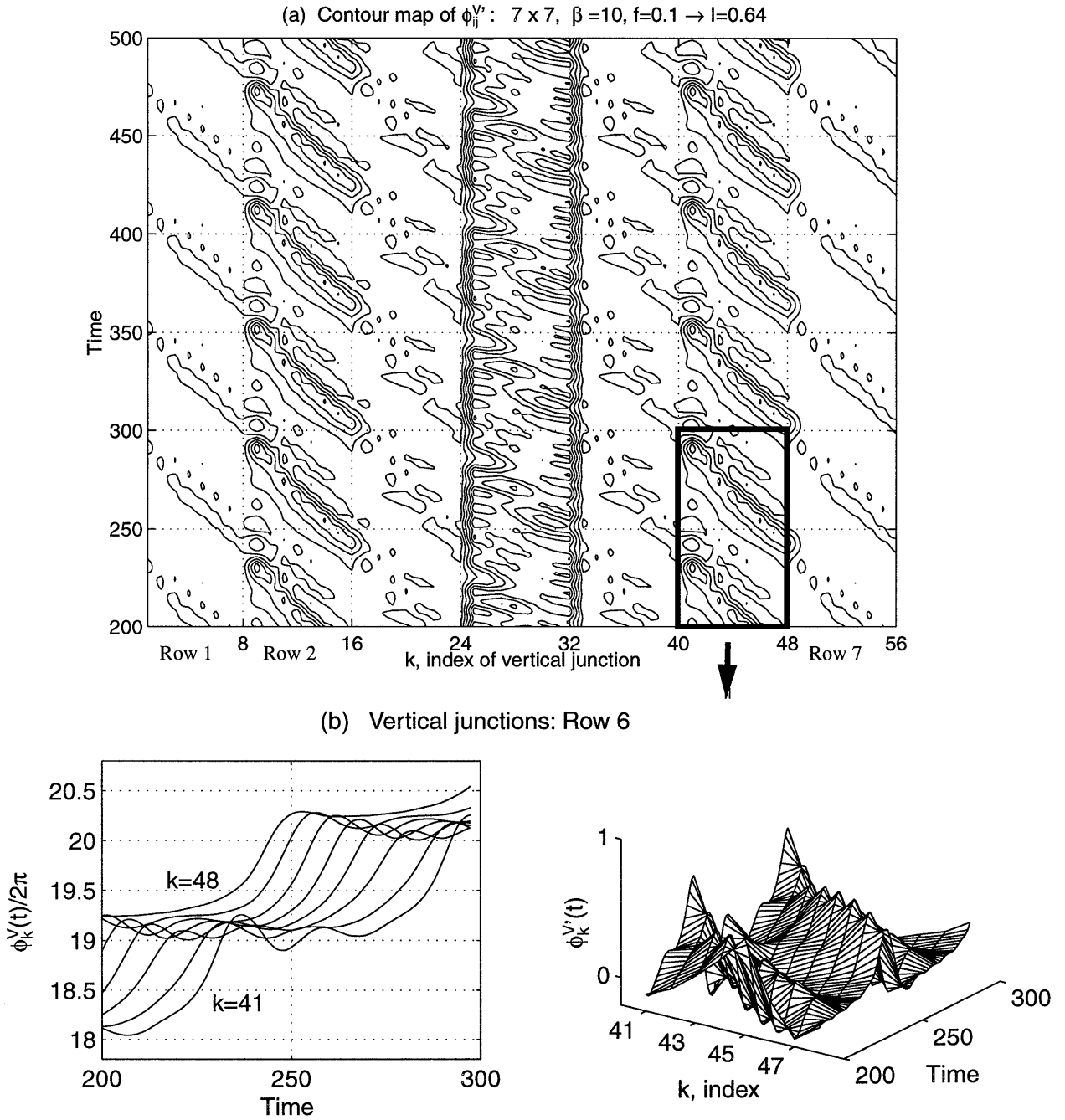


Figure 3-4: (a) Spatio-temporal graph of the solution for the same example of Figure 3-2, at $I = 0.64$. We represent a contour map of $\phi_{ij}^{V'}$ of juxtaposed rows of vertical junctions indexed according to Figure 3-3(a). The different behaviors of the rows is clearly visible and analyzable from the graph. For instance, row 6 –marked with arrows in (a)– is studied in (b) by showing the time evolution of the phases ϕ_k and the spatio-temporal dependence of ϕ_k' for this row, $k \in [41, 48]$. It corresponds to a clear pattern of vortex propagation, as discussed in Section 3.3.

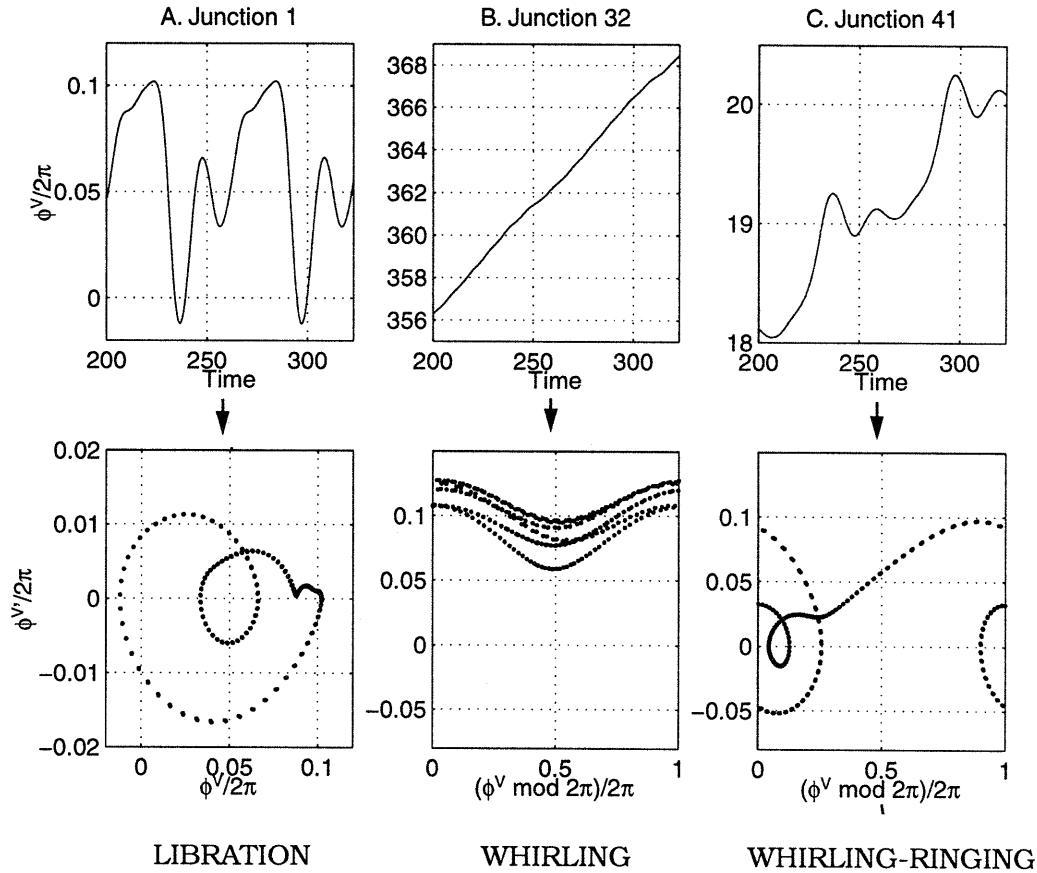


Figure 3-5: Individual motion of three vertical junctions of the array with the same parameters as in Figure 3-4. For all three, the top row depicts $\phi(t)$ and the bottom row corresponds to the phase portrait ϕ' vs. ϕ . The first column (A) corresponds to a librating junction in row 1. Column B shows a whirling junction in row 4. Finally, column C shows a junction with whirling-ringing motion in row 6, where localized kink-like excitations (“vortices”) propagate.

- Figure C presents a *whirling-ringing* solution. In this case the junction goes over the top rapidly, producing a 2π jump in the phase, but describes also some oscillations (ringing) around a ghost equilibrium point in between whirling motions. The concept of ringing implies that there are regions in the phase portrait where $\phi' < 0$, and the pendulum displaces backwards.

In summary, using the techniques described above we can quantify the dependence on f and I of several of the features of the I - V characteristics. We also achieve a more fundamental description of the different regimes in the I - V curves in terms of the dynamical behavior of the system. We have found the following properties helpful

to describe the system:

1. *Identification of non-superconducting rows.* One of the main characteristics of these arrays – and object of much recent research [92, 66, 83]– is the appearance of stable solutions which are spatially non-uniform. This feature is readily observable from the spatially extended $I-V$ (Figure 3-3) where non-superconducting rows appear as the ones with a non zero average frequency.
2. *Periodicity.* We study Poincaré sections in the phase portraits of Figure 3-5 to obtain the period of each of the junctions. From this analysis we can deduce the periodicity of the different rows and the overall periodicity of the solution. Periodic repetition and spatial symmetry are also observable in the spatiotemporal contour map in Figure 3-4.
3. *Propagation of waveforms.* Most easily studied in the space-time diagram (Figure 3-4), where patterns and waveforms can be seen to propagate from right to left in some of the rows. We can quantify the analysis by numerically calculating the velocity of propagation of the “waveform” and the degree of nonuniformity of the propagation. This serves to distinguish between two types of propagating waveforms: a train of localized excitations moving usually along a row (“vortices”); and another solution uniformly extended over the row linearly dependent both on space and time (“whirling mode”).
4. *Type of motion of the pendula.* We label the motion of each of the pendula under one of the three categories described above: librating, whirling, whirling-ringing. We will observe that this classification is directly related to the type of propagation observed in the row.

This section summarizes the computational procedure used to simulate the $I-V$ characteristics and argues for a more complete use of the dynamical information provided by the spatio-temporal solutions so obtained. We have also introduced several numerical tools which facilitate the understanding of the complicated dynamical behavior of the system. In particular, they serve to reveal the interplay and transition

between regimes in which “particle” and “wave” interpretations are more appropriate. Moreover, the pendulum analogy for the junctions introduces useful mechanical concepts and terminology and is a powerful means of visualization for the system. Only methodological and notational aspects have been addressed until now. In the following sections we apply these tools to study the nonlinear dynamics of square arrays of underdamped and overdamped Josephson junctions.

3.3 Array of underdamped junctions

We begin the characterization of two-dimensional, open-ended square arrays by studying the dynamical behavior of arrays formed by *underdamped* junctions, with $\beta = 10$. The mechanical terminology stems from the analogy of each of the junctions to a nonlinear pendulum with damping $\Gamma = 1/\sqrt{\beta}$, as given in (3.6). A small damping translates into a motion with large inertia, or large mass, with a small rate of decay and a strong tendency to persist once it has begun. This is the reason for the existence of hysteretic phenomena in the I - V curves when β is large. Experimentally, this limit corresponds to aluminum junctions whose resistance is large, as discussed in Section 2.2.2, and, thus, have larger β . On the other end, we find Nb – Al₂O_x – Nb junctions, with smaller resistance and β , which are experimental realizations of the underdamped limit $\beta = 0$ and which we will address in the following section.

We have studied numerically the dependence of the simulated I - V characteristics on the external magnetic field f for a 7×7 square open-ended underdamped array, at zero temperature, in the limit where self-fields are negligible, ($\lambda_{\perp} \rightarrow \infty$). To this end, we consider arrays of junctions with $\beta = 10$ and varying magnetic field $f = 0.05, 0.1, 0.2, 0.3$. Each point of the simulated I - V curve for a given $\{\beta, f\}$ is obtained by numerically integrating the system of governing equations (3.16) for each value of I , and averaging the calculated frequency over time and over the complete array, $\langle \bar{\phi}_{i,j}(t) \rangle \equiv \langle V \rangle$. The current is then swept up at small increments to complete the graph of $\langle V \rangle$ vs. I and the final phase configuration of each point is taken as the initial condition for the next integration with the new I .

The resulting I - V characteristics for varying f , shown in Figure 3-6, have been extensively studied in the literature as diagnostic tools which allow direct comparison to the I - V curves of related systems, like the single junction, flux lattices or continuous superconductors [78, 63, 74]. The different regions in the I - V characteristics correspond to distinct dynamical regimes of the junctions in the array. Similarly to the ladder array, there are three main regimes –superconducting, flux flow, whirling– which are found as the current is increased. It is important to remember that a sim-

ulated, or even experimental, I - V represents a *dynamical* path through the different states, or solutions, of the system. This is closely related, but not exactly equivalent, to finding the solution which is energetically most favorable at each point. In fact, there are regions in which two or more dynamical solutions coexist and the state in which the system finds itself depends critically on the past history of the experiment, i.e. hysteretic effects are characteristic of these arrays. The usual sequence as the current is increased can be observed in Figure 3-6 and summarized as follows:

1. The array is initially in a *superconducting solution* in which all junctions librate with negligible amplitude and with zero average frequency. The calculation of ground states for $I = 0$ is a well documented topic in the literature [82, 81] although it is not trivial to extend those results to obtain the state of minimum energy in the presence of a current. Independently of this, when the critical current I_{dep} is reached, all the fixed points of the system go unstable (or cease to exist, presumably through a saddle-node bifurcation) and a solution with a finite $\langle V \rangle$ appears.
2. After the depinning of the array, the system enters the *flux-flow* region, usually characterized as a non-static (that is, non-superconducting) state with resistance directly proportional to f , in the limit of small f . The flux-flow resistance is seen to depend on λ_{\perp} [85] and is always much smaller than the normal resistance of the array. In fact, this linear dependence is a simplification of a more complicated behavior which includes some clear substructure.
3. The flux-flow solution becomes unstable at a current I_{switch} where *whirling modes* are dominant. In these whirling solutions, one or more of the rows of the array can be described by a whirling mode, similar to those described for the ladder in Chapter 2: all the junctions in the row whirl almost harmonically, i.e. with almost constant frequency, and generally out of phase. There exist spatially non-uniform solutions, called *partially row switched states*, where some rows are in the whirling mode and others remain either superconducting or in the flux-flow regime. As the current is increased, the final, most resistive *totally*

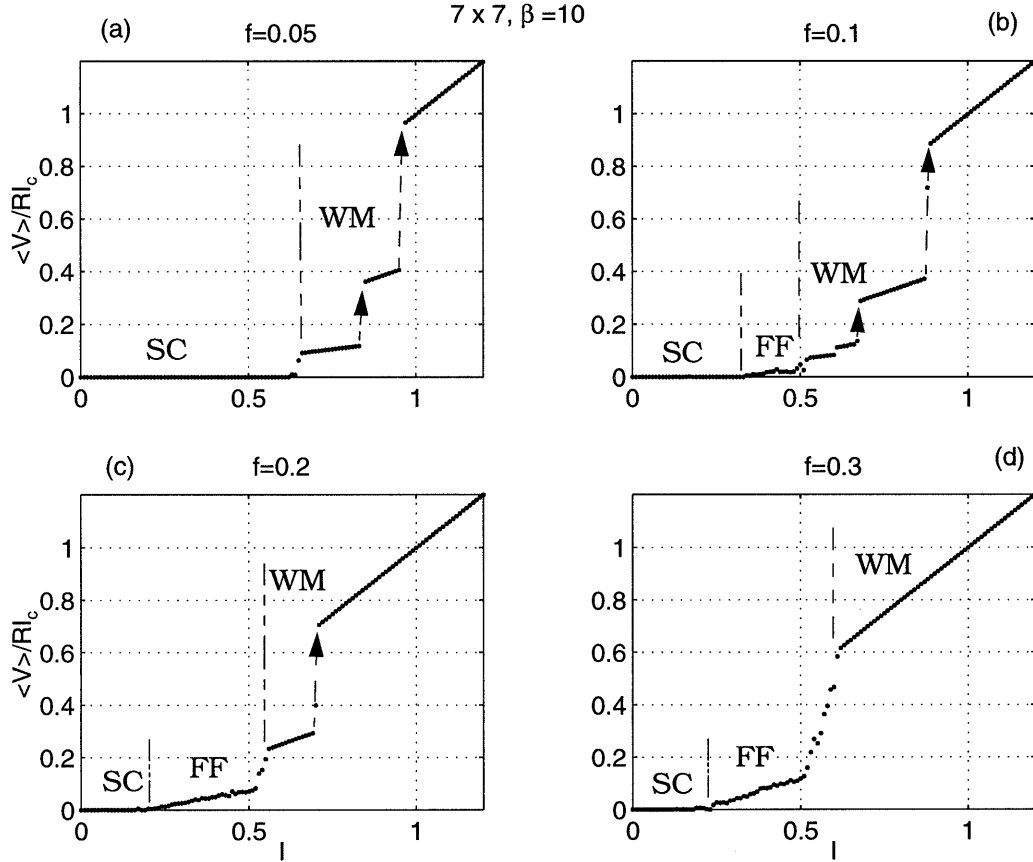


Figure 3-6: Direct path of the I - V curves for an underdamped 7×7 array with $\beta = 10$ and varying f . We have indicated the three dynamical regions: superconducting (SC), flux-flow (FF) and whirling modes (WM).

switched state is reached, where all rows (and junctions) can be described with the whirling solution and the I - V dependence is ohmic with a resistance per junction equal to its normal resistance R_n .

This description of the I - V characteristics can be made more precise and quantitative by using the numerical tools described in Section 3.2.2. We choose the case $f = 0.1$ in Figure 3-6(b) to exemplify the analysis which was also performed on the other examples. In Figure 3-3(b) we can already observe the importance of the spatially non-uniform solutions. The existence of partially row switched states—where some rows oscillate with an “ohmic” average frequency while others remain superconducting—is clearly visible for currents $I > I_{switch} \simeq 0.52$. In Figure 3-7 we also summarize the detailed calculation of the period of the solution, the velocity of

propagation of the waveforms, and the classification of the junctions-pendula according to their type of motion. These are obtained numerically from the spatio-temporal diagrams and the phase portraits of the junctions as explained above.

We briefly describe the dynamical behavior for this case $f = 0.1$ in terms of a series of critical currents as follows:

- For $I < I_{dep} = 0.34$, the array remains in a superconducting solution which contains vortices. This is expected for 2-D arrays as the critical field for penetration of vortices is $f_c \approx 0.08$ [67].
- The interval $0.34 < I < I_{switch} = 0.52$, corresponds to the flux flow region where the motion of the active junctions is of the whirling-ringing type as shown in Figure 3-7(c). Moreover, the solution is not spatially uniform since only the three central rows present a non zero average frequency. In fact, a process of row activation is produced at $I = 0.36$ when the solution goes from one to three active rows. It is also unexpected that the solution in this regime is periodic in the interval $0.34 < I < 0.40$. Below we explore this complicated regime in more detail.
- The region where whirling modes are dominant begins at $I_{switch} = 0.52$. The sequence of row-switching occurs as the current is increased:
 - * For $0.52 < I < .60$, one row is whirling while the rest are superconducting.
 - * From $I = 0.60$ to 0.68 , the central row (number 4) remains whirling but rows 2 and 6 get activated to a flux-flow whirling-ringing solution. That is, this is a mixed solution where row 4 can be described with a stretched kink (whirling mode) while rows 2 and 6 present propagation of localized waveforms or kinks, in a typical flux flow pattern.
 - * At $I = 0.68$, rows 2 and 6 switch to whirling. This three-rows switched state is observed until $I = 0.88$.
 - * The totally row switched state appears at $I = 0.88$. For currents above, the behavior is purely ohmic.

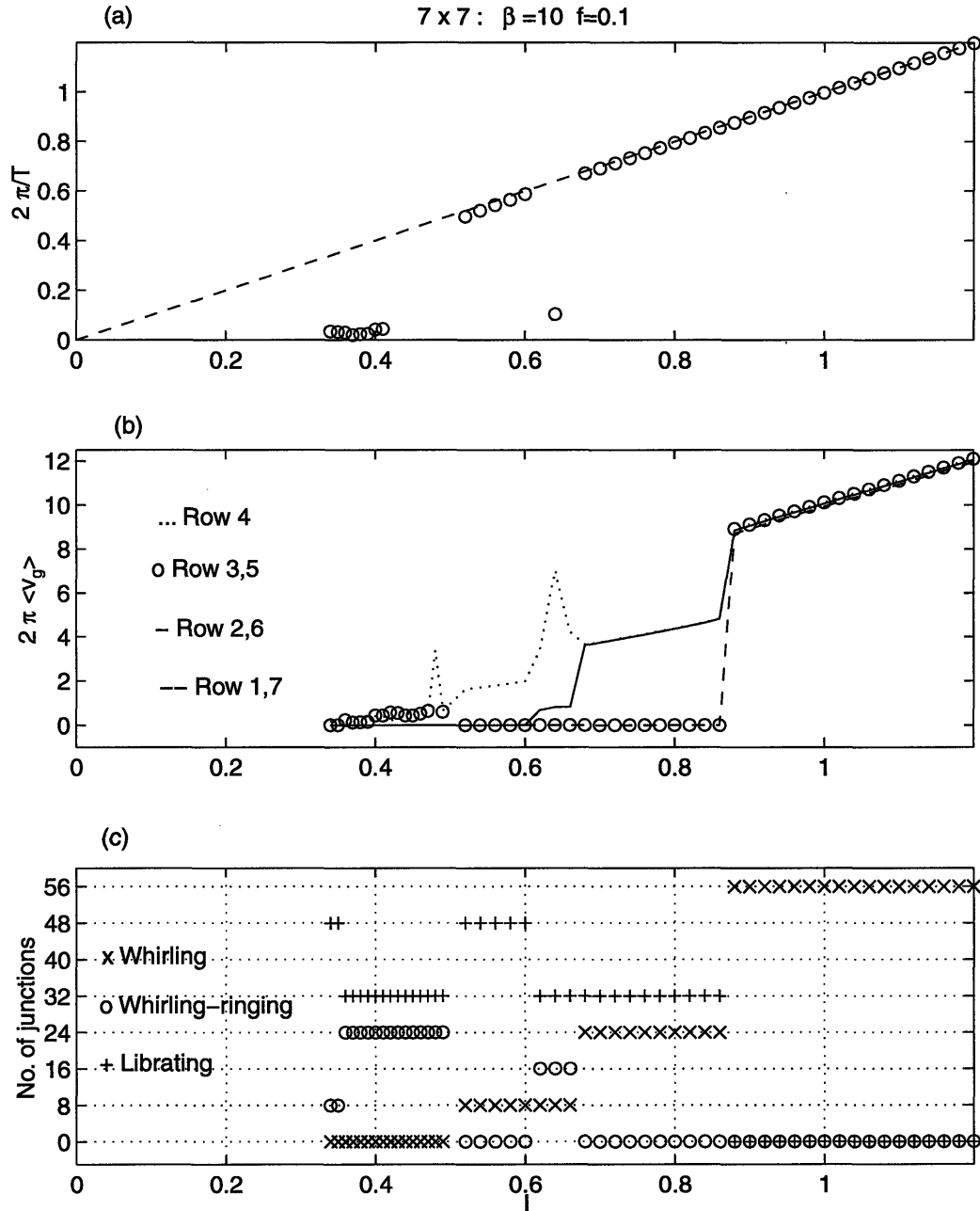


Figure 3-7: Detailed dynamical analysis of the I - V characteristic of a 7×7 array with $\beta = 10$ and $f = 0.1$: (a) Frequency of the overall solution ($2\pi/T = \omega/\sqrt{\beta}$) as a function of I . Note that whenever there is whirling motion, the frequency is always $2\pi/T_0 \simeq I$; (b) Velocity of propagation of waveforms in each of the rows as a function the normalized current; (c) Number of junctions with each of the three types of motions (libration, whirling-ringing, whirling) as a function of I . The flux-flow region is characterized by whirling-ringing motion. Row-switching corresponds to pure whirling motion.

(a) Normalized current, I

f	I_{dep}	Flux-flow region: No. of active rows			
		1	3	5	7
0.05	0.63	0.63-0.64			
0.1	0.34	0.34-0.35	0.36-0.50		
0.2	0.24				0.24-0.48
0.3	0.24				0.34-0.53

(b) Normalized current, I

f	I_{switch}	Whirling region: No. of switched rows			
		1	3	5	7
0.05	0.66	0.66-0.83	0.85-0.95	0.97-	
0.1	0.52	0.52-0.60	0.68-0.87	0.88-	
0.2	0.54	0.54-0.69		0.71-	
0.3	0.60				0.60-

Table 3.1: 7×7 underdamped array ($\beta = 10$): (a) Critical currents for the flux-flow region: depinning and row activation sequence. (b) Row-switching sequence for the whirling region: Intervals of I where the different spatially non-uniform solutions exist.

This type of descriptive analysis is carried out for other values of f to obtain a similar overall picture. The increase in magnetic field f produces the expected effects: the flux flow of vortices takes place in more rows, and the critical currents at which the row-switching in the whirling region, and the row-activation in the flux flow region, take place, decrease. We have summarized these numerical results in Table 3.1.

We consider now a more detailed study of the spatio-temporal solutions of the observed dynamical regimes. Analytical results for $2-D$ arrays are scarce, and mainly constrained to overdamped arrays [53, 24] or deal with the in-phase state stability [101]. Recently, analytical techniques based on a continuum approximation, with fluid mechanical notation, have yielded a promising description for the solution of the totally row switched state and its properties [95]. In this section, some analytical work will be presented together with a numerical characterization of the solutions. Moreover, we will establish a close parallelism between these regimes and the corresponding behaviors in the ladder array, for which we obtained a rigorous description

in Chapter 2. Therefore, the physical picture of the solutions, bifurcations and ranges of validity for the regimes of the ladder can be used as a guide for the characterization of the more complicated $2-D$ arrays. At the same time, the observed differences between the two devices are the result of both very strong constraints in the y direction and dominance of edge effects in the ladder array.

3.3.1 Superconducting state and depinning

As discussed for ladder arrays (Section 2.3), the problem of depinning is related to the calculation of the point where the ground state of the system undergoes a bifurcation that affects its stability. We have not carried out an in-depth study of the dependence of I_{dep} vs. f . However, the depinning behavior of the ladder can be used to establish some qualitative understanding of the depinning in $2-D$ arrays. The behavior for ladder arrays can be summarized as follows: For $f < f_{c1} \approx 0.29$, the configuration with a vortex in the array is *not* the ground state of the system. Thus, one-vortex configurations are at most metastable, i.e. dynamically stable but energetically unstable, and the vortices are expelled as the current is increased. In this region, the depinning occurs when the *no-vortex* solution undergoes a saddle-node bifurcation which, we concluded, is dominated by the effects from the edges. On the other hand, for the small interval around $f \approx 1/2$, the half-filled solution dominates the depinning behavior.

A similar phenomenon is observed for the two-dimensional case, the main difference being the small value of f_{c1} , the critical field for which the entrance of one vortex is energetically favorable. A rough estimate of this field, obtained from the continuum formula presented in [67], gives $f_{c1} \approx \ln N^2 / N^2 \simeq 0.07$ for a 7×7 array. Therefore, the region where the no-vortex solution is relevant, and, hence, an edge-dominated depinning occurs, is very narrow. It is observable however, in $I_c(f)$ diagrams [12, 70, 73] as a smooth decaying region for $f < f_{c1}$, reminiscent of the behavior observed in the ladder. An example of such a solution is found for $f = 0.05$ and shown in Figure 3-8. Although it should be amenable to analysis with the techniques developed in Chapter 2, we have not yet followed that direction which might

7 x 7, $\beta = 10$ $f = 0.05$ $l = 0.63$

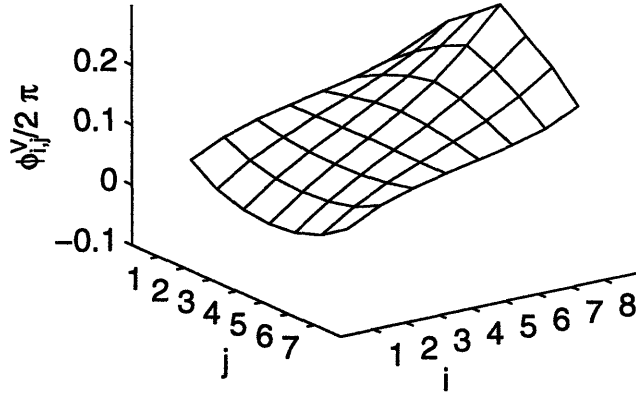


Figure 3-8: Example of no-vortex superconducting configuration in a 7×7 array – equivalent to the no-vortex solution for the ladder. In the two-dimensional case, these states are ground states of the system for $f < f_{c1} \approx 0.07$ and, hence, relevant for the depinning only in that interval. The depicted configuration corresponds to $f = 0.05$.

yield an analytical explanation to the numerical fitting obtained for the $I_c(f)$ at small field in [12].

For $f > f_{c1}$ the ground states with vortices are responsible for the critical current of the array and the analysis of the depinning behavior becomes more involved. However, we note that the observed values of the depinning for $2-D$ arrays when $f > f_{c1}$ and *incommensurate* are similar to the values of I_{dep} close to $f = 1/2$ in the ladder. One could argue that the depinning of incommensurate configurations with many vortices for open-ended arrays will be dominated by the barrier at the edges (roughly given by the I_{edge} calculated for the quasi-one-dimensional ladder in Section 2.3.3). Similarly, if periodic boundary conditions are considered, the barrier should be approximately I_{LAT} . Commensurate states have to surmount added barriers and thus appear as peaks of the $I_c(f)$ when f is a rational number.

3.3.2 Totally row-switched state

At the other end of the $I - V$, the high I limit, the system is in the totally row-switched solution. As stated above, in this state all the rows can be approximated

with a whirling solution similar to the one obtained for the ladder array (2.98), i.e. the stretched kink

$$\phi_j^V = \xi_j = \omega\tau + 2\pi f j + \mathcal{O}(\omega^{-2}), \quad \phi_j^H = \mathcal{O}(\omega^{-2}) \quad (3.18)$$

where $\omega = I\sqrt{\beta}$ is large. Recent analytical studies show that this assumed solution can be made consistent with the equations of the system and the boundary conditions at the edges, when applying a continuum formulation [95]. Moreover, it can be shown that the implicit coupling in the y direction produces coherence between all the rows when $f \neq 0$, as seen in the simulations. In other words, this totally row-switched solution is similar to a stack of in-phase whirling ladders. Thus, the average voltage is

$$\frac{\langle V \rangle}{RI_c} = N_y I \quad (3.19)$$

where N_y is the number of cells in the vertical direction. Moreover, the wavelength of the waveform is $\lambda = 1/f$. Both observations are shown in Figure 3-9 together with similar data from partially row-switched states. In summary, the totally row-switched state is virtually equivalent to the whirling mode of the ladder array which is well described with the zeroth order solution (3.18), since the effect of edges can be neglected, as seen in page 97 of Section 2.4. Therefore, the observables of the $2-D$ system which depend on the whirling mode will have the same behavior as for the ladder. We have checked that the $I-V$ dependence is indeed equivalent. We expect also that the repinning behavior on the return path (not studied here) will be the same, i.e. no steps will be observable for a $2-D$ array with no inductances, and the repinning will be caused by the parametric instabilities that the whirling mode undergoes due to the resonance of its whirling frequency with the eigenfrequencies of the lattice. This equivalence of the repinnings of the ladder and the $2-D$ array can be seen in several simulations [66] where the return path has been calculated and, most dramatically, in [28] where the repinning of the single junction through a homoclinic bifurcation and that of the array through parametric instabilities are directly compared.

As an illustration of the physical concepts underlying this system, we compare now this “wave” description to the usual “particle” formulation of the problem, where vortices are considered to be propagating in the array. Although they give equivalent results for the totally row-switched state, we will show this is not the case for the partially row-switched solutions, where only the wave description -in terms of the whirling mode- is able to explain the numerical observations.

Within the vortex picture, the flow of magnetic flux is viewed as the motion of particle-like vortices at constant speed $\tilde{u} = dx/d\tau$ across the array. Thus, \tilde{u} is the terminal velocity of a motion resulting from the competition between the electromagnetic force, which tends to accelerate the vortices, and the dissipation of energy in interactions with the lattice, which can be modelled as a drag force opposing the motion.

We consider a $N_x \times N_y$ array with a uniform magnetic flux f . The voltage produced by the uniform motion of a uniform vortex density f is given by Faraday’s law as

$$\langle V \rangle = - \frac{d\Phi}{dt} \frac{dt}{d\tau} = \tilde{u} N_y f \Phi_0 \frac{2\pi R I_c}{\Phi_0} = I_c R N_y 2\pi f \tilde{u}.$$

From (3.19) the speed of the vortices is then

$$\tilde{u} = \frac{I}{2\pi f}. \quad (3.20)$$

It is immediate to check that this is precisely the phase and group velocities of the stretched kink (3.18)

$$v_p = v_g = \frac{\omega}{k} = \frac{I}{2\pi f}.$$

Hence, both descriptions are consistent for the totally row-switched case.

3.3.3 Partially row-switched states

As explained above, spatially non uniform whirling solutions exist for underdamped arrays. In these, only certain rows switch to a whirling solution while the rest remain usually superconducting, although they can also present vortex propagation. In fact,

		Current, I								
		Number of switched rows, m								
f	1			3			7			
	$1/\lambda^v$	$1/\lambda^w$	$1/\lambda^{num}$	$1/\lambda^v$	$1/\lambda^w$	$1/\lambda^{num}$	$1/\lambda^v$	$1/\lambda^w$	$1/\lambda^{num}$	
0.1	0.7	0.4	0.34	0.233	0.2	0.19	0.1	0.1	0.10	
0.2				0.467	0.4	0.38	0.2	0.2	0.20	
0.3							0.3	0.3	0.30	

Table 3.2: $1/\lambda$ for the switched rows of a partially row-switched solution in a 7×7 array, $\beta = 10$. $1/\lambda^v$, calculated with the vortex picture (3.22), is not able to reproduce the numerical $1/\lambda^{num}$ obtained from several linear fits like the ones presented in Figure 3-9, for different f and I . Our prediction from the wave description $1/\lambda^w$ given in (3.32) and (3.32) is in good agreement with the numerics.

the observed I - V dependence is, expectedly,

$$\frac{\langle V \rangle_m}{I_c R} = mI \quad (3.21)$$

where m is the number of switched rows (Figure 3-9).

One is tempted to apply the vortex picture, as for the totally row-switched state, to obtain the speed of propagation of the vortices as

$$\tilde{u}_m = \frac{m}{N_y} \frac{I}{2\pi f}.$$

By equating \tilde{u}_m to the group velocity of the waveform, the wavelength of the whirling mode (in the m rows which have switched) would be found to be

$$\lambda_m^{pred} = \frac{m}{N_y} \frac{1}{f}. \quad (3.22)$$

In Figure 3-9 and Table 3.2, we show that the waveforms of the switched rows are indeed whirling modes (3.18) but the wavelength does *not* agree with the predicted value from the vortex picture (3.22).

Therefore, for partially row-switched states, the vortex picture does not explain

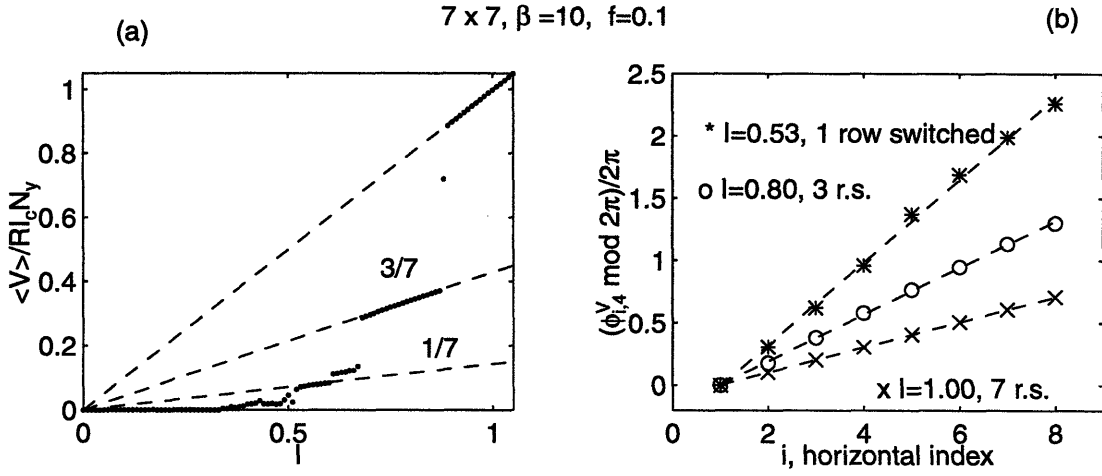


Figure 3-9: Partially row-switched states in a 7×7 array, with $\beta = 10$, $f = 0.1$: (a) I - V characteristic. The dotted lines have slopes $3/7$ and $1/7$ for the resistance as given by (3.21). Moreover, the frequency of all the row-switched states (both partially or totally) is $\omega \simeq I\sqrt{\beta}$, as shown in Figure 3-7. (b) Example of spatial dependence of the switched rows. The dashed lines depict the linear dependence, as in a whirling mode, with slopes $1/\lambda_{num}$ given in Table 3.2.

the observation that

$$1/\lambda_{num} \approx p f, \quad p \in \mathcal{Z}.$$

We show now that this dependence is a direct consequence of the constraints from the edges and is accounted for within the whirling mode formulation. This calculation, for a 7×7 array with notation from Figure 3-1, can be summarized as follows:

The conservation of current (3.5) imposed at the $N_y + 1 = 8$ right edge nodes yields:

$$\left\{ \begin{array}{l} I + I_{7,1}^H = I_{8,1}^V \\ I_{8,j-1}^V + I_{7,j}^H = I_{8,j}^V, \quad j = 2, \dots, 7 \\ I_{8,7}^V + I_{7,8}^H = I \end{array} \right\} \Rightarrow \sum_{j=1}^8 I_{7,j}^H = 0. \quad (3.23)$$

That is, the balance of current moving in the x direction is zero. This is the condition of returning currents when edges are present, as seen for the ladder array. It can be

propagated successively to the left to yield the more general expression:

$$\sum_{j=1}^8 I_{i,j}^H = 0, \quad \forall i. \quad (3.24)$$

Let us consider now the solution for the *1 row-switched* state. As observed numerically, this solution corresponds to having row 4 in a whirling mode with all the other rows in a superconducting solution:

$$\begin{cases} \phi_{i,j}^V = \arcsin I + A_{i,j}, & j = 1, 2, 3, 5, 6, 7 \\ \phi_{i,4}^V = \omega\tau + ki + \mathcal{O}(\omega^{-2}), & \text{with } \omega = I\sqrt{\beta} \text{ large} \end{cases} \quad (3.25)$$

where $A_{i,j}$ are corrections introduced by the presence of the edges. Here we have used the solutions obtained for the ladder as an approximation for each of the rows: the whirling solution for row 4 and the no-vortex superconducting solution for the rest.

As a preliminary, but not trivial, calculation, let us consider the zeroth order of the assumed solution (3.25), by neglecting the corrections $A_{i,j}$ and contributions of order $\mathcal{O}(\omega^{-2})$. This zeroth order solution can be shown to fulfill the governing equations (3.8)-(3.9) when the following conditions are met for all i ,

$$\phi_{i,j+1}^H - \phi_{i,j}^H = -2\pi f, \quad j = 1, 2, 3, 5, 6, 7 \quad (3.26)$$

$$\phi_{i,5}^H - \phi_{i,4}^H = k - 2\pi f. \quad (3.27)$$

One last assumption is needed to obtain a solution for the one-row-switched state. In Chapter 2 we established that the corrections $A_{i,j}$ for the superconducting solution *near the edges* are larger, of $\mathcal{O}(1)$, than the corrections for the whirling mode, $\mathcal{O}(\omega^{-2})$. Thus, we can assume that the current across the whirling row is roughly I

$$I_{i,4}^V \simeq I, \quad \forall i. \quad (3.28)$$

Substituting this in (3.24) we obtain two independent conditions for the upper and

bottom halves of the array

$$\sum_{j=1}^4 I_{i,j}^H = 0, \quad \sum_{j=5}^8 I_{i,j}^H = 0, \quad \forall i. \quad (3.29)$$

Thus, the presence of a whirling row divides the array in almost independent sides coupled only through the existence of the horizontal junctions (3.27).

Some algebraic manipulations with (3.26),(3.27) and (3.29) yield the zeroth order (no edges) solution for the one-row-switched state:

$$\begin{cases} \phi_{i,1}^{H\dagger} = 3\pi f = \phi_{i,5}^{H\dagger} \\ \phi_{i,2}^{H\dagger} = \pi f = \phi_{i,6}^{H\dagger} \\ \phi_{i,3}^{H\dagger} = -\pi f = \phi_{i,7}^{H\dagger} \\ \phi_{i,4}^{H\dagger} = -3\pi f = \phi_{i,8}^{H\dagger} \end{cases} \quad (3.30)$$

$$\begin{cases} \phi_{i,j}^{V\dagger} = \arcsin I, & j = 1, 2, 3, 5, 6, 7 \\ \phi_{i,4}^{V\dagger} = \omega\tau + ki, & \text{with } k = 8\pi f, \end{cases} \quad (3.31)$$

and we take this solution to be valid for all i , since we are neglecting the effect of the edges. Also, all phases have been reduced to the $[-\pi, \pi)$ interval. The calculated wavelength for the only row switched is then

$$1/\lambda_1 = \frac{k}{2\pi} = 4f. \quad (3.32)$$

The same calculation is performed for the solution with three switched rows to obtain

$$\begin{cases} \phi_{i,j}^{H\dagger} = (-1)^{j+1}\pi f, \\ \phi_{i,j}^{V\dagger} = \arcsin I \text{ for } j \text{ odd} \\ \phi_{i,j}^{V\dagger} = \omega\tau + ki \text{ for } j \text{ even, with } k = 4\pi f. \end{cases} \quad (3.33)$$

Thus, in this case

$$1/\lambda_3 = 2f, \quad (3.34)$$

in agreement with the values of Table 3.2.

The comparison of these approximate solutions and the numerical results is presented in Figure 3-10. It is readily observable that the zeroth order approximation captures the main features of the numerics and explains the values obtained for the wavelength of the whirling rows (Table 3.2). The small discrepancies observed are due to the effect of the edges which have been neglected in this simple calculation. A future direction of work is the incorporation of those corrections using the techniques developed in Chapter 2.

There is one last important observation to be made from this physical picture of the row-switched states. Consider our 7×7 array in the dynamical state where three rows (2,4 and 6) have switched to a whirling solution and the rest remain superconducting, as shown in Figure 3-10 (c)-(d). Comparing the approximate solution (3.33) for this state and the solutions obtained in Chapter 2 for the ladder, we conclude that the phase configuration of each the switched (superconducting) rows in (3.33) is the same as the whirling (no-vortex superconducting) solution for a single isolated ladder. That is, the $2-D$ array with an alternating sequence of superconducting-whirling rows is equivalent to a series of quasi-independent superconducting ladders, weakly coupled. In this sense, the effect of a whirling row is to “uncouple” the regions above and below it.

Because the three-switched-rows solution is roughly equivalent to four uncoupled superconducting ladders with no vortices, an immediate consequence can be drawn: the point at which the three-rows switched state becomes unstable is equivalent to the point at which these four no-vortex ladders *depin*, i.e. the critical current for the ladder for the given frustration. This prediction is checked to excellent agreement by comparing the values for the end of the three switched-rows state in Table 3.1, and the depinning currents for the ladder in Table 2.1. Likewise, the $2-D$ 7×7 array with one row switched is equivalent to two quasi-uncoupled superconducting 7×3 arrays. Hence, the switching point from the one whirling row solution, should correspond to the depinning of a 7×3 array with no vortices present. We obtained numerically values of 0.82 and 0.60 for $f = 0.05$ and 0.1 respectively in excellent agreement with

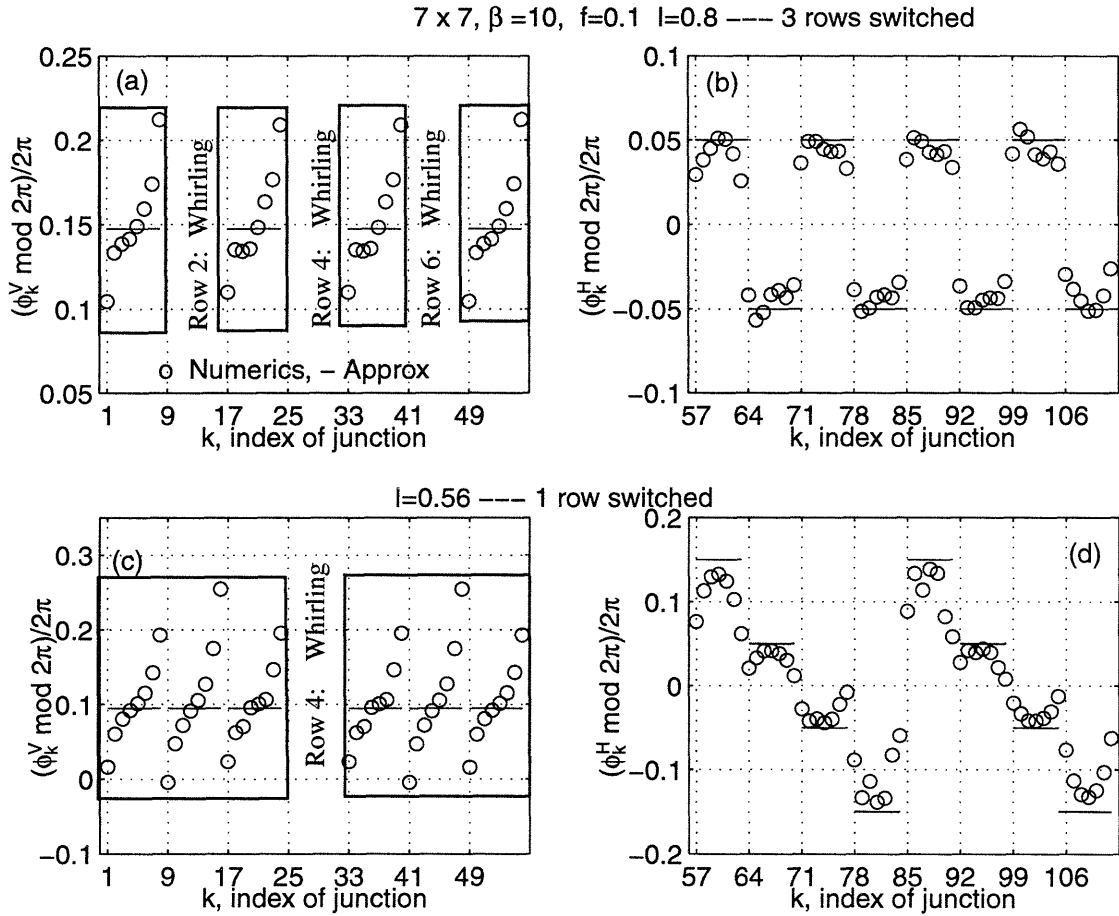


Figure 3-10: Partially row-switched state: — approximated $\{\phi_{i,j}^{V\dagger}, \phi_{i,j}^{H\dagger}\}$ and \circ numerical solutions for $f = 0.1$. (a) and (b) show the vertical and horizontal junctions of the superconducting rows when rows 2, 4, 6 have switched. The same is depicted in (c) and (d) for the case when only one row (number 4) is whirling. The whirling rows effectively divide the array in quasi-independent regions. This feature can be used to predict the critical currents for some of the row-switching events.

the values in Table 3.1.

These observations supply evidence that the sequence of row-switching events can be related to the depinning currents of smaller semi-independent subarrays in which the global array is divided by the existence of whirling rows acting as separating boundaries. The analysis presented here is, by no means, exhaustive. It is reasonable to expect that it could be meaningful for small arrays where the row-switching steps are clearly marked and visible, specially in the last row-switching jumps. Not so much when the arrays are bigger with a larger number of vortices, since then the row-switching sequence is more complicated resulting in smoother jumps. We note also, that our studies are performed in the limit where self-field effects are neglected. The presence of a finite λ_{\perp} modifies the row-switching process introducing added asymmetries and complexity [85]. In conclusion, the “wave” formulation, in terms of whirling modes, provides an accurate description of the problem, as shown by the calculation of the wavelength of the waveforms and the good approximation obtained for the phase configuration. On the other hand, the “particle”, or vortex, picture is not illuminating in high I limit and can lead to wrong conclusions.

3.3.4 Flux-flow regime

We finish this section with the numerical characterization of the flux-flow region. This regime has been classically described in terms of the motion of vortices under electromagnetic and drag forces as in the flux-flow of continuous superconductors. This fluid mechanical model [63] translates into a linear dependence of $\langle V \rangle$ vs. I with a resistance R_{ff} , smaller than the normal resistance of the array. Moreover, R_{ff} is linearly dependent on f , in the limit of small f .

From the dynamical point of view, the flux-flow region presents two features which we have used for the identification of the regime:

1. The spatio-temporal evolution of the system is dominated by the motion of *kink-like localized excitations*, which can be associated with the motion of vortices. These excitations produce jumps of 2π as they propagate in the array.

2. If the junctions are viewed as mechanical pendula, their motion in this regime can be characterized as *whirling-ringing*: periods of small oscillations around a center (ringing) interspersed with rapid overturns (whirling). Operationally, this means there is always an interval of the trajectory with negative velocity. Note that the pendula are underdamped and there is some inertia in their motion, which intuitively explains the presence of the ringing due to overshooting after the whirling. Moreover, these small oscillations can couple to the linear modes of the lattice providing an additional mechanism for the dissipation of energy in the propagation of the vortices in the lattice.

These two properties are illustrated in row 6 of Figure 3-4 and in Figure 3-5 C.

Although this qualitative description is not in conflict with the fluid mechanical view of flux-flow expressed above, it underlines the oversimplification involved in such a model as pointed out by Bobbert [8] and Beck [4]. Indeed, a nonlinear viscosity has been recently introduced [32] to account for the observed quantitative discrepancies with the linear viscous force model. However, the nonlinear functional form for the viscosity is introduced *ad hoc* and its physical interpretation is not straightforward. Other approaches have taken the interaction with spin waves to explain the non-linearity of the propagation [90, 28]. Our observation of the dynamical simulations supports the view of the complexity of the vortex motion in the array. First, the motion of the vortices is clearly nonuniform. Second, the horizontal junctions also play a role allowing some vertical motion of the vortices. Thus, a simple and meaningful statistical description could be difficult. A possible line of research would be the characterization of the flow of vortices as a process of anomalous diffusion stemming from a nonlinear deterministic system [3, 35, 80]. We do not follow this approach here.

Instead, we study the spatiotemporal dynamics of the flux-flow region with the tools described in Section 3.2.2 to identify features of the solution which can be hidden if only averaged quantities are considered. The detailed numerical analysis for $f = 0.1$ is summarized in Figure 3-11 where the $I-V$ curve is shown together with the dependence of the period and the velocity of propagation of vortices on the current.

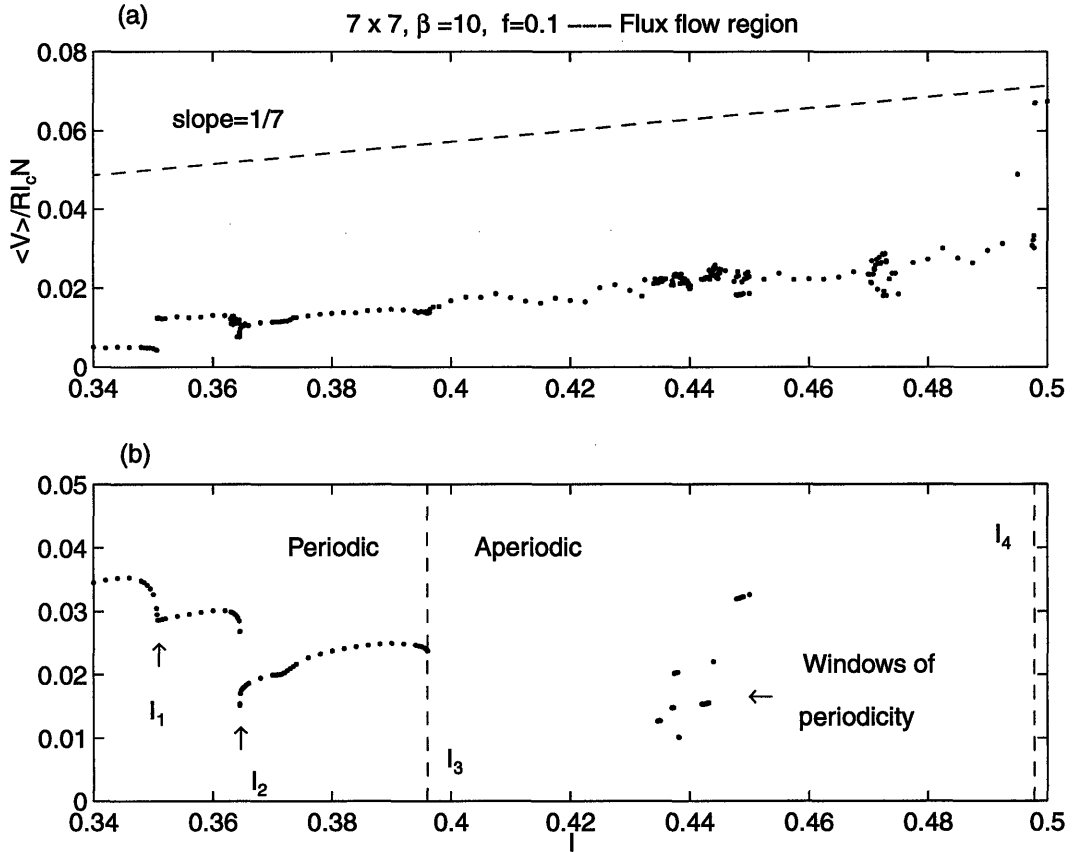


Figure 3-11: Detailed study of the flux-flow region for $\beta = 10$ and $f = 0.1$: (a) blow-up of the I - V characteristic, (b) frequency of the solution. The critical currents which mark the bifurcations have been indicated on the graphs. Note that the frequency is ~ 10 times smaller than the corresponding whirling frequency.

We emphasize the following unexpected properties:

- *Row activation:* An active row is a non-superconducting, non-whirling row, with a finite voltage difference caused by the propagation of kink-like excitations along it. In a process similar to row-switching, rows become active as the current is increased. In our example, a change from a one-active-row to a three-active-rows state occurs at $I \simeq I_1 = 0.3506$. After that, only three rows are active. We do not elaborate this point here since it will be treated more thoroughly in the following section on overdamped arrays where the full scale of row-activation can be observed. We note, however, that the critical currents at which a certain number of rows become active (Table 3.1) are the same for underdamped and overdamped arrays.

- *Periodicity*: Despite its overall complexity, the flux-flow solution is periodic in several intervals. The description of our case of study is:

- * For $0.34 < I < 0.396$, the solution is periodic with period T which changes continuously with I . However, at $I_2 = 0.3645$, T jumps discontinuously from a value of 37.22 to 65.39. We have studied this transition carefully to conclude that it is not exactly a period doubling bifurcation.

- * At $I_3 = 0.3960$, the system becomes aperiodic through an unspecified bifurcation. However, the system remains close to the periodic solution and some windows of periodicity reappear within the aperiodic region. This behavior presents some characteristics of quasi-periodicity.

- * The flux-flow solution switches to the whirling solution at $I_4 = 0.4978$.

These transitions, depicted in the following figures, suggest the complexity of the flux-flow solutions. A careful numerical analysis of the bifurcations to classify and identify the traits in the behavior has not been undertaken in this thesis. We will explore this regime in more depth in the next section, when we deal with overdamped junctions. The impossibility of row-switching –due to the intrinsic properties of the “pendula”– in that case, allows the unfolding of a larger region of “flux-flow” where the features we have discussed can be fully developed.

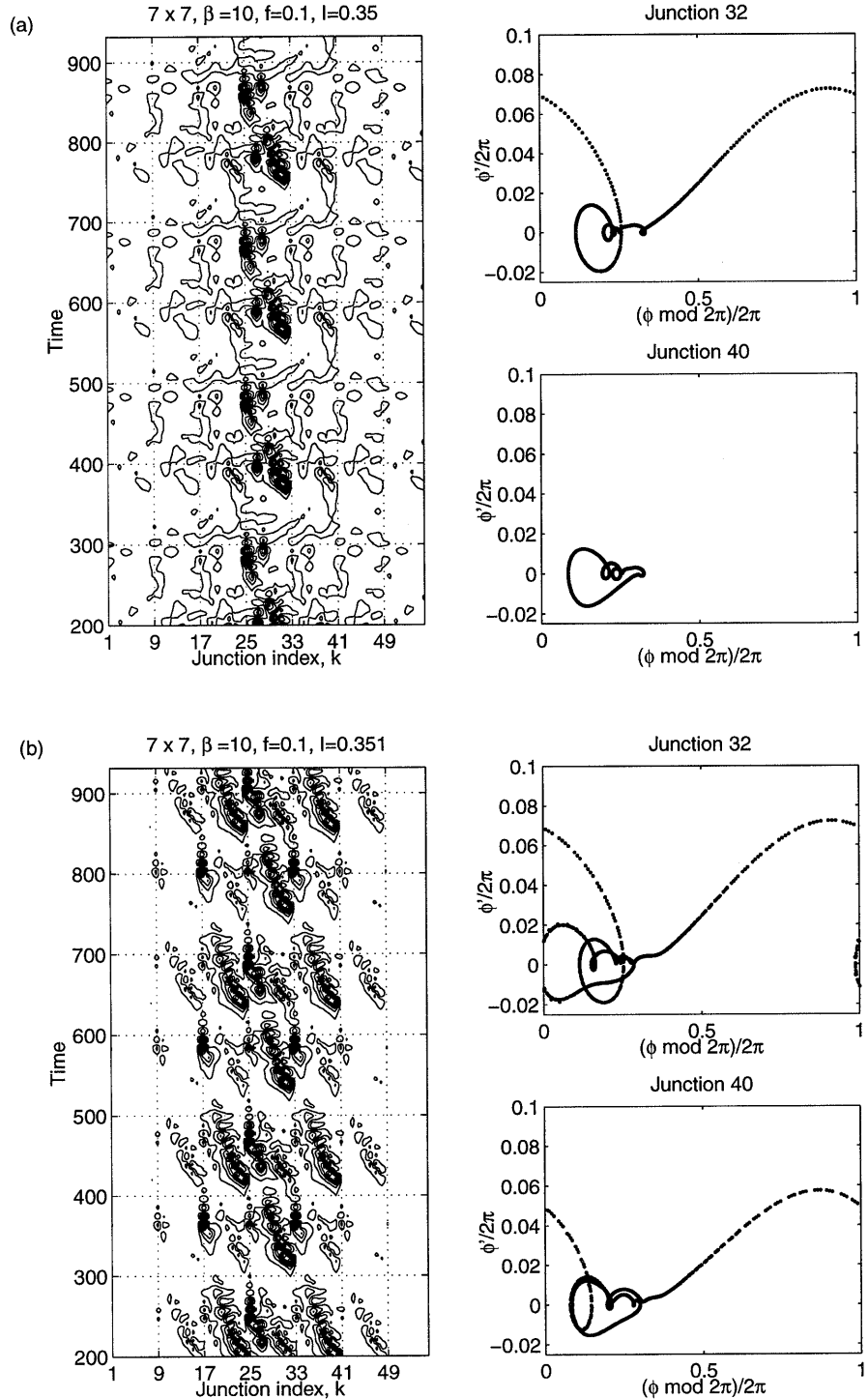


Figure 3-12: Transition from 1 to 3 active rows, i.e. (a) to (b). At $I_1 \simeq 0.350$, flux begins to flow in rows 3 and 5. The junctions in those rows change from librating to whirling-ringing. Note the similarity between the attractor of the libration, before the bifurcation, and the ghost attractor around which the ringing occurs for junction 40 after I_1 .

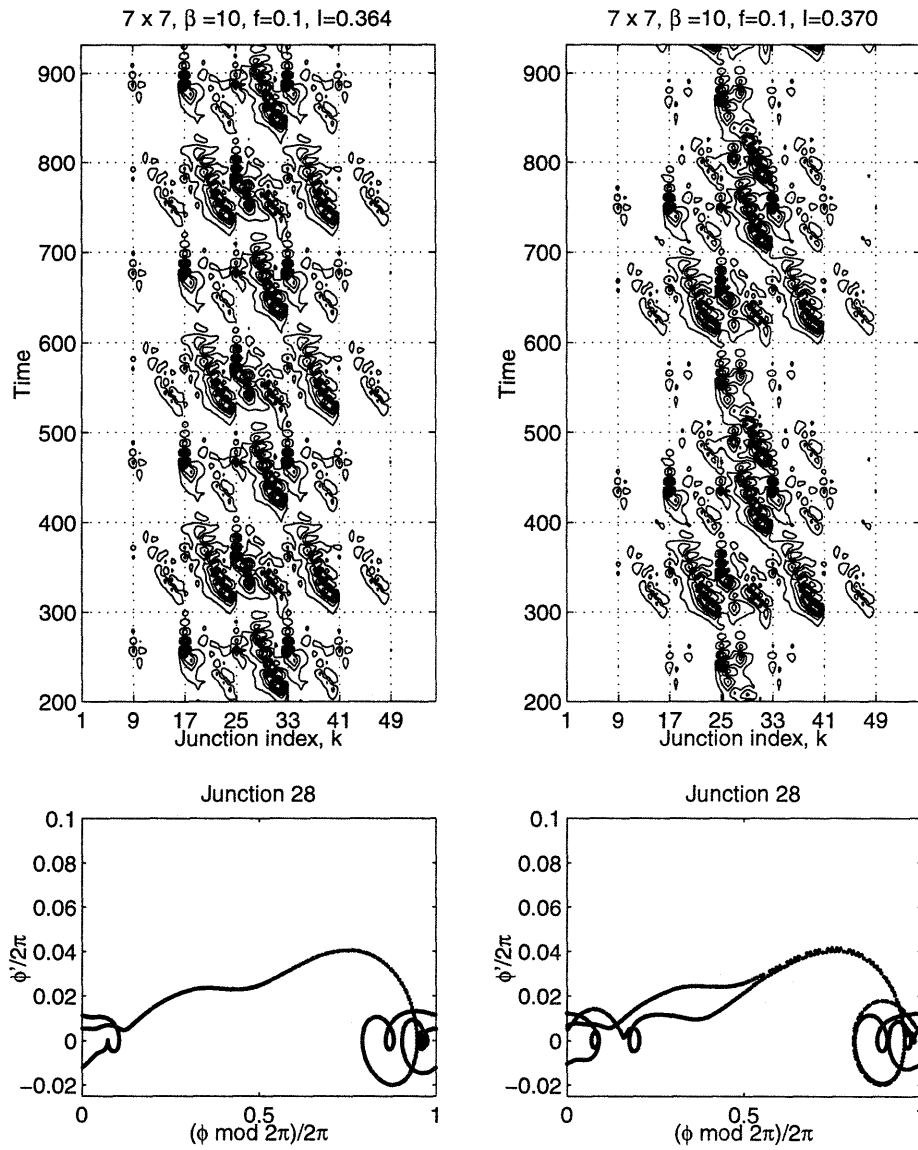


Figure 3-13: Quasi-period doubling at $I_2 \simeq 0.365$. The period changes discontinuously almost doubling. Note the second trajectory appearing in the phase portrait of junction 28. Each of those correspond to a different vortex propagating in the row.

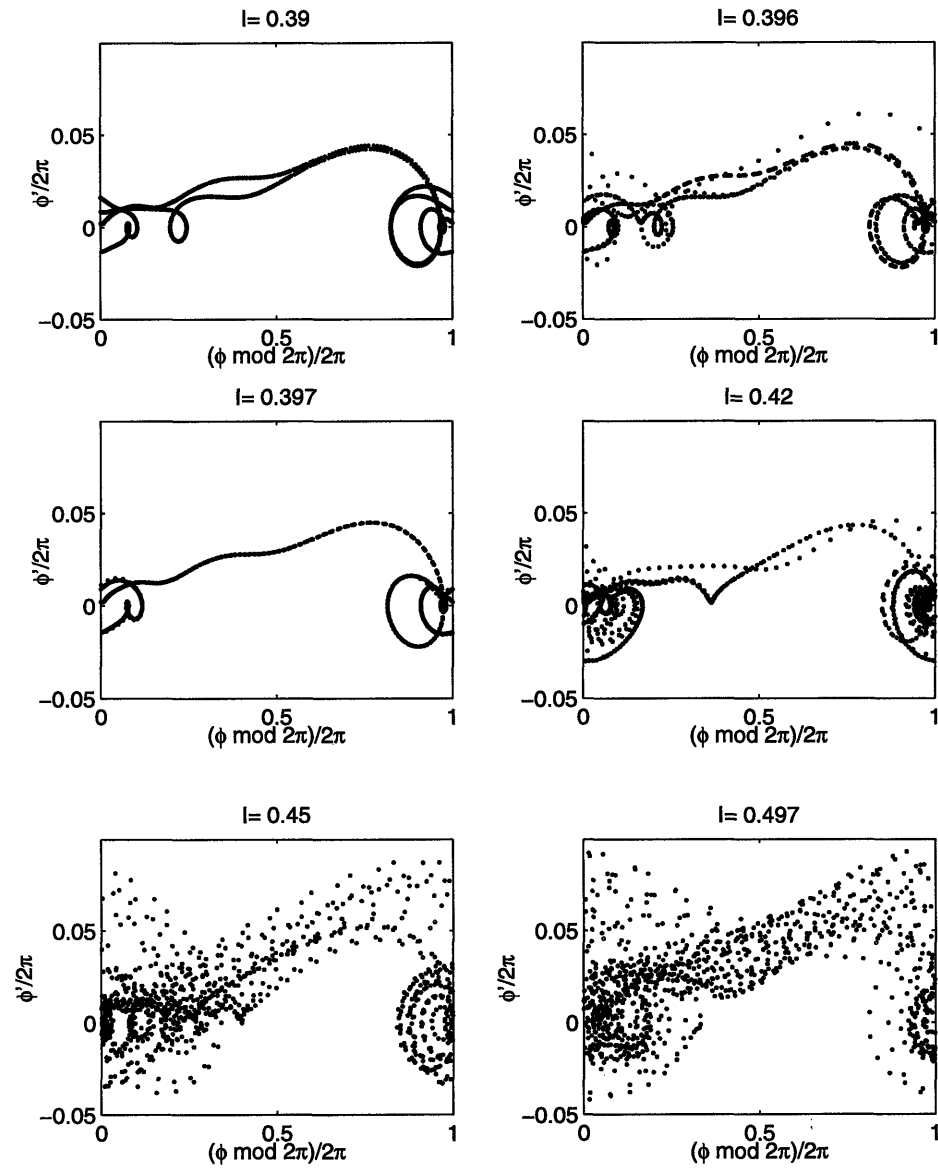


Figure 3-14: Sequence of states between $I_3 \simeq 0.396$, where the system becomes aperiodic, and $I_4 \simeq 0.498$, where the flux-flow solution becomes unstable and the system switches to the whirling dominated states. In this region, there is a parallel existence of periodic and aperiodic solutions which hints at a quasi-periodic pattern.

3.4 Array of overdamped junctions

The general methodology for the simulations in overdamped arrays is identical to the underdamped case, and we will not review it here. The procedure is mathematically and computationally simpler since the equations for the individual junctions are first order differential equations in the overdamped system, i.e. the overdamped junction corresponds to the limit $\beta = 0$ in (3.7) which now becomes

$$\phi' + \sin \phi = I. \quad (3.35)$$

Thus, each individual pendulum is a first order system with no inertia. An exact solution for this separable equation is readily obtainable, namely

$$\phi = 2 \arctan \left\{ \frac{1}{I} + \frac{\sqrt{I^2 - 1}}{I} \tan \left(\frac{\tau \sqrt{I^2 - 1}}{2} \right) \right\},$$

which can be integrated over a period to give [63]

$$\langle V \rangle = \frac{1}{T} \int_0^T \frac{d\phi}{dt} dt = \sqrt{I^2 - 1}.$$

This is the non-superconducting solution for the single overdamped junction when $I > 1$, i.e. after depinning.

Due to the properties of the individual junctions, we expect that the behavior of the array is qualitatively different to the underdamped case. Very briefly, and using the notation introduced in Section 3.3, the sequence of dynamical regimes is the following:

1. For $I < I_{dep}$, the solution is *superconducting* and the junctions librate negligibly.
2. At $I = I_{dep}$, a finite voltage develops and the system enters the *flux-flow* regime, characterized by propagation of solitonic excitations and by whirling-ringing motion for the active pendula.
3. Contrary to the underdamped array, there are *no* row-switching events. This is

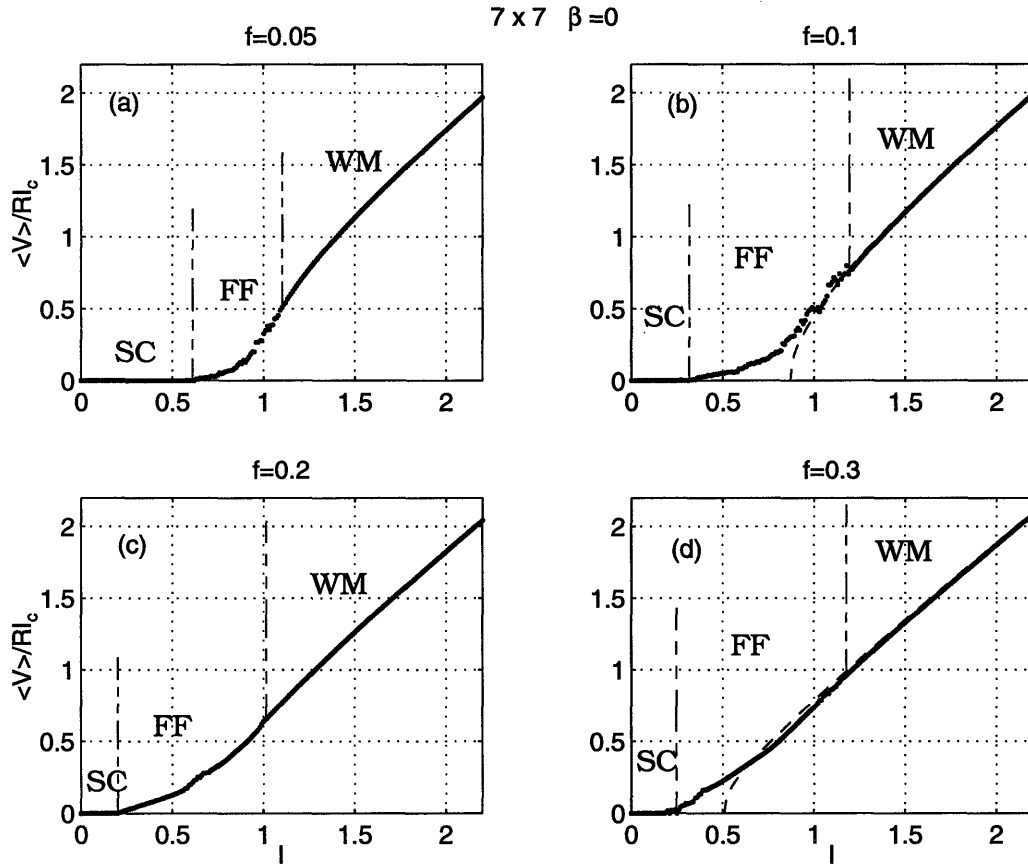


Figure 3-15: Direct path of the $I-V$ curves for an overdamped 7×7 array with $\beta = 0$ and varying f . The three dynamical regions, superconducting (SC), flux-flow (FF) and whirling modes (WM) are indicated. Dashed lines in (b) and (d) are the $I-V$ characteristics of overdamped ladders with the corresponding frustration, f .

the result of the lack of inertia of the pendula, which prevents the appearance of regions of “localized whirling”. Thus, the flux-flow region unfolds fully and extends until the whirling solution is reached continuously at I_{switch} . This makes the overdamped limit ideal to study the complicated series of dynamical states which take place in the flux-flow regime, as we will do in the remainder of this section.

4. It is not clear from the I - V curves where the whirling mode starts since there is no clear jump and the transition is continuous. However, we can denote I_{switch} , the current at which we enter the whirling region, in the sense introduced in the previous section: that the motion of all the pendula is always forward and no pendulum has intervals where $\phi' < 0$. In short, there is no more ringing in the array.

This sequence is exemplified by representative I - V characteristics in Figure 3-15.

As seen above, the information contained in the I - V curves is not sufficient for a satisfactory characterization of the regimes. The situation is greatly improved by the systematic use of the numerical tools described in Section 3.2.2. The detailed numerical study of the cases represented in Figure 3-15 yields some conclusions regarding the three dynamical regimes which we now summarize.

First, the *depinning current* is roughly the *same* as for underdamped arrays. This is expected from our studies of the depinning in the ladder array (Section 2.3) since β does not have any effect on the existence of the superconducting solutions.

Secondly, at the other end of the I - V curve, the whirling solution, defined as the configuration where all the pendula whirl and none undergoes a whirling-ringing motion, is reached continuously from the flux-flow. This solution is characterized in the literature as a phase of homogeneous flow [16] or in terms of the absence of defects in the flux-lattices [22, 29]. Our definition in terms of the dynamics of the pendula, though very different in nature, is in effect associated with the same physical picture: a lattice of vortices propagating *rigidly* in time is incompatible with some of the pendula describing whirling-ringing motions. These motions create the characteristic

defects and mismatches of the last region of flux-flow.

Regarding the whirling solution, we also note that the asymptotic behavior of this branch at high I is the same as that of a ladder of overdamped junctions under the same frustration, as shown for $f = 0.1$ and $f = 0.3$ in Figure 3-15(b) and (d). This can serve as a simplified path to calculate the limiting whirling configuration [53, 24].

Finally, we describe the most important regime in overdamped arrays: the *flux-flow* region. Although its convoluted behavior with its precise details is difficult to account for, we find the following three general features:

Sequence of row-activation The number of rows which participate in the flux-flow is directly proportional to f and I . When f is sufficiently small, a sequence of *row-activation* events is observed as the current is increased, as seen very clearly in Figure 3-16 for $f = 0.05$. However, the rows do not jump to the whirling mode, as in the row-switching phenomena of Section 3.3, and instead go now from the superconducting to the flux-flow solitonic solution; that is, they go from being silent to “active”. The critical currents for the row-activation events, presented in Table 3.3, imply a sequence of changes in the slope of the I - V curve (Figure 3-16). It is intriguing to observe, by comparing Tables 3.1 and 3.3, that the current intervals for which a given number of rows are active, are roughly the same for $\beta = 0$ and $\beta = 10$. This seems to suggest that the number of active rows depends on the flow and the current and not on β . In the underdamped array, however, the full extension of the flux-flow is not realized as the system switches to the states dominated by the whirling modes.

In all our simulations with no inductances we also note that the order in which rows *activate* and *switch* follows different rules. In Section 3.3 we deduced that, in underdamped arrays a switched row effectively acts as a boundary which divides the array in two parts. Within this picture, the consecutive switchings are equivalent to depinnings of smaller subarrays. This mechanism predicts that the switched rows will be as *separated* from the edges and from other switched rows as possible, since the center of the array is where the depinning is more

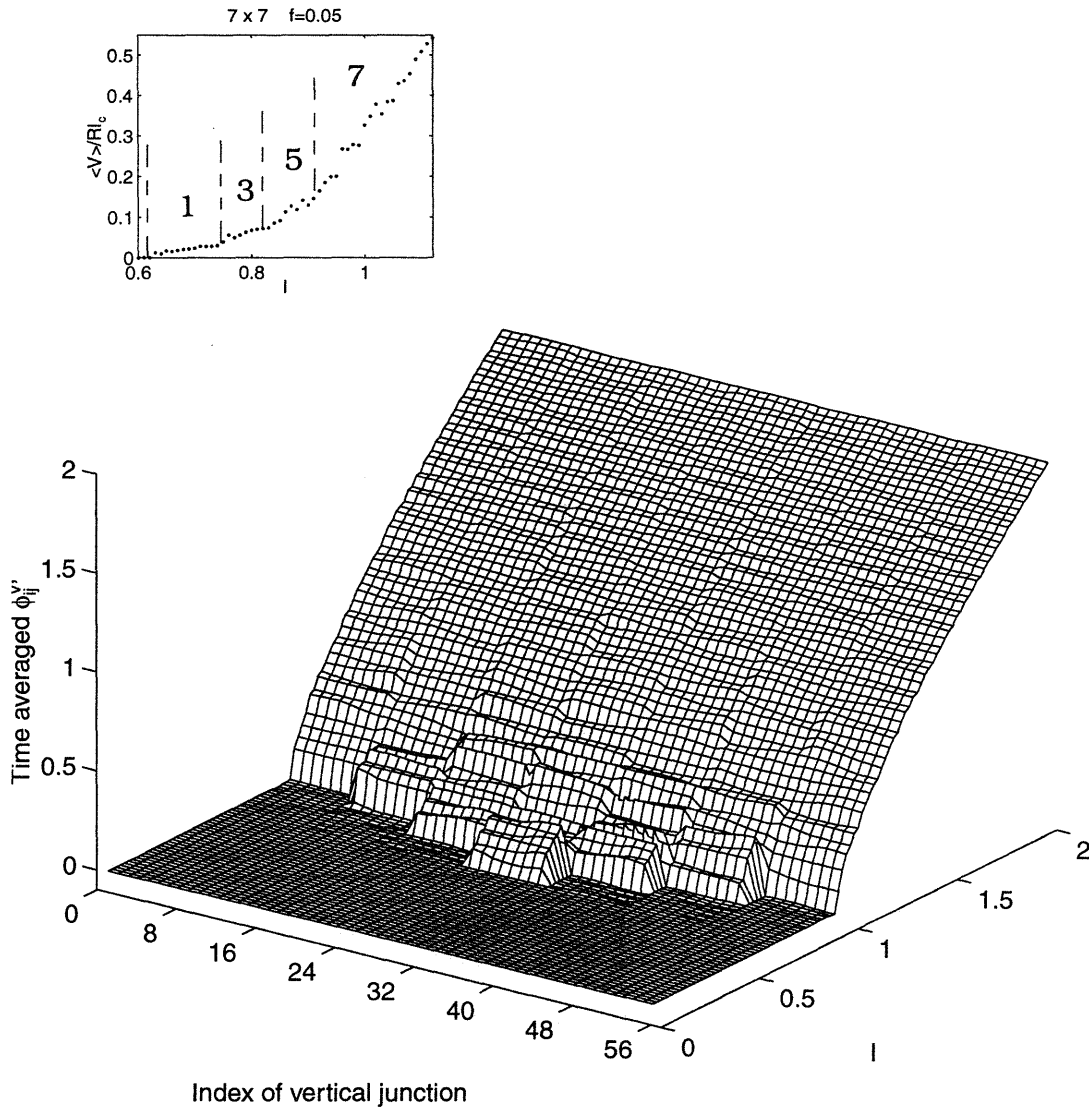


Figure 3-16: Activation of rows in the flux-flow region of a 7×7 array of overdamped junctions $\beta = 0$ with $f = 0.05$. Inset shows a blow-up of the flux-flow region of the $I-V$ characteristic showing the change in slope as the number of active rows changes.

Normalized current, I						
f	I_{dep}	Flux-flow region: No. of active rows				I_{switch}
		1	3	5	7	
0.05	0.63	0.63-0.74	0.75-0.80	0.85-0.92	0.93-0.99	1.09
0.1	0.31	0.31-0.35	0.36-0.51	0.59-0.81	0.82-1.06	1.17
0.2	0.25			0.25-0.48	0.59-0.67	1.01
0.3	0.26				0.35-0.43	1.14

Table 3.3: Critical currents for a 7×7 overdamped array and intervals where flux-flow is constrained to a given number of rows. I_{switch} is the current at which all junctions whirl with no ringing.

likely to be produced. The contrary occurs here: in overdamped arrays, active rows tend to appear around rows which are already activated. This is expected since the wake of the propagating vortices excites the junctions in the closer rows, thereby favoring their activation.

Alternation of periodic and aperiodic solutions As the current is swept up, periodic and aperiodic solutions alternate. Also, the period changes, both continuously and discontinuously. The periodicity of the overdamped system has been discussed in the literature in connection with Frenkel-Kontorova models [22, 29, 56, 53]. However, rigorous results which could justify either the asymptotic periodicity of the solutions (as obtained under special constraints for first order systems with convex potentials by Middleton [58]) or the persistence of truly chaotic metastable states under the dynamical evolution of the system [56], are not applicable in this case. Thus, the observed aperiodicities cannot be disregarded as mere transients. Numerically, however, we observe a strong underlying periodicity in the system which manifests itself even in the aperiodic intervals (Figure 3-17 (a) and (b) is a clear example of all these features).

Transition to whirling solution When all the rows are active, the end of the flux-flow regime occurs through a final transition from a disordered, internally flexible phase of propagating vortices to an ordered, rigid whirling configuration [53], where relative displacements between rows do not occur. The transition can be

7 x 7 $\beta=0$ $f=0.3$

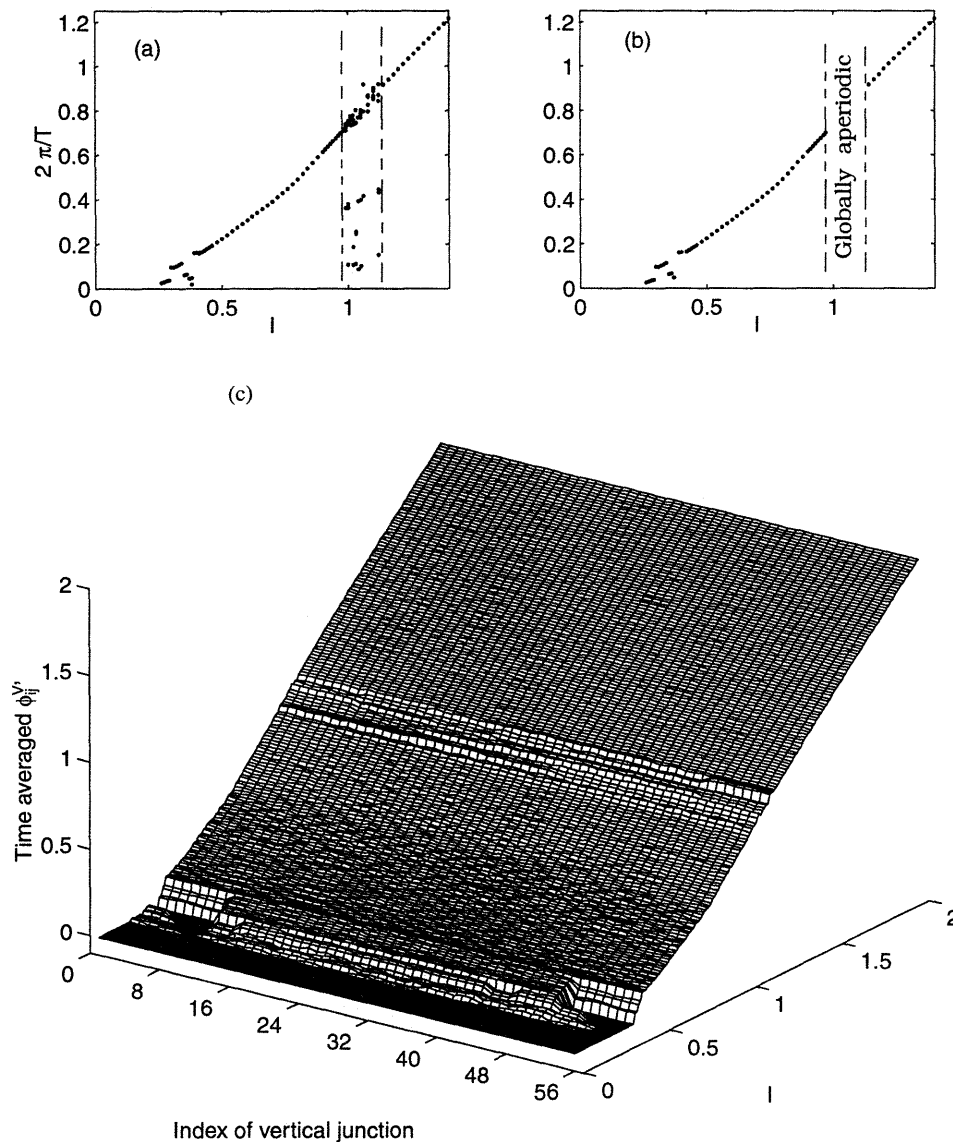


Figure 3-17: Frequency of the solution for $\beta = 0$ with $f = 0.3$ and transition to the rigid whirling state. (a) and (b) show the frequency of each of the seven rows and of the total solution respectively. In the interval $0.98 < I < 1.2$, all the rows are roughly periodic but with different periods. Thus, the overall periodicity is lost. Observe in (c) the spatially inhomogeneous solutions in that interval. In effect, the rows are displacing relative to each other. After the transition to the rigid whirling state, these displacements do not occur.

seen in Figure 3-17 and occurs for all values of f for values of I slightly larger than 1. This is the point when all the pendula go to a state of pure whirling motion and no whirling-ringing is left. As the current is increased further, the motion of all the pendula becomes more homogeneous. Thus, a network of whirling pendula with quasi-homogeneous motion tends to be equivalent to a rigid space-time structure with no internal displacements.

In summary, the physical picture that emerges from these observations is the following: for moderate f , and at low current, the I - V characteristic is dominated by the consecutive activation of rows; once all of them are active, the variations in type and number of defects in the flux lattice are responsible for the I - V dependence. The transition to the whirling solution is produced when the flux-lattice becomes rigid and internal relative displacements vanish.

The importance of the edges is shown in Figure 3-18, where the dynamics at small f and current close to the depinning value is shown. In this case, the evolution of the system is described as an aperiodic succession of individually propagating vortices being nucleated and expelled at the edges. Sometimes they are reflected from the boundary and propagate from left to right as *antivortices*. This dynamical description explains the observations of Chung *et al.* [12] in their simulations for small fields. As they hypothesized from inspection of the time-dependent voltage, the spikes in this voltage correspond to propagation of individual vortices; the bursts of spikes are the result of collisions and complex motion of the vortices. This behavior is typical of the zero-field regime and has been documented both experimentally [47] and in simulations [33]. We have also observed similar modes in the open-ended ladder array for $f = 0$.

We conclude by emphasizing the similarities of this picture with the behaviors which appear in systems, both continuous [74, 54] and discrete [16], where flux-lattices move under a potential with a certain amount of randomness. In those cases, three similar regimes to the ones listed above are also observed: channel-like motion of vortices; global “plastic” motion of the deformable flux-lattice; transition to a rigid flux-lattice which displaces coherently in time. We conjecture that the presence

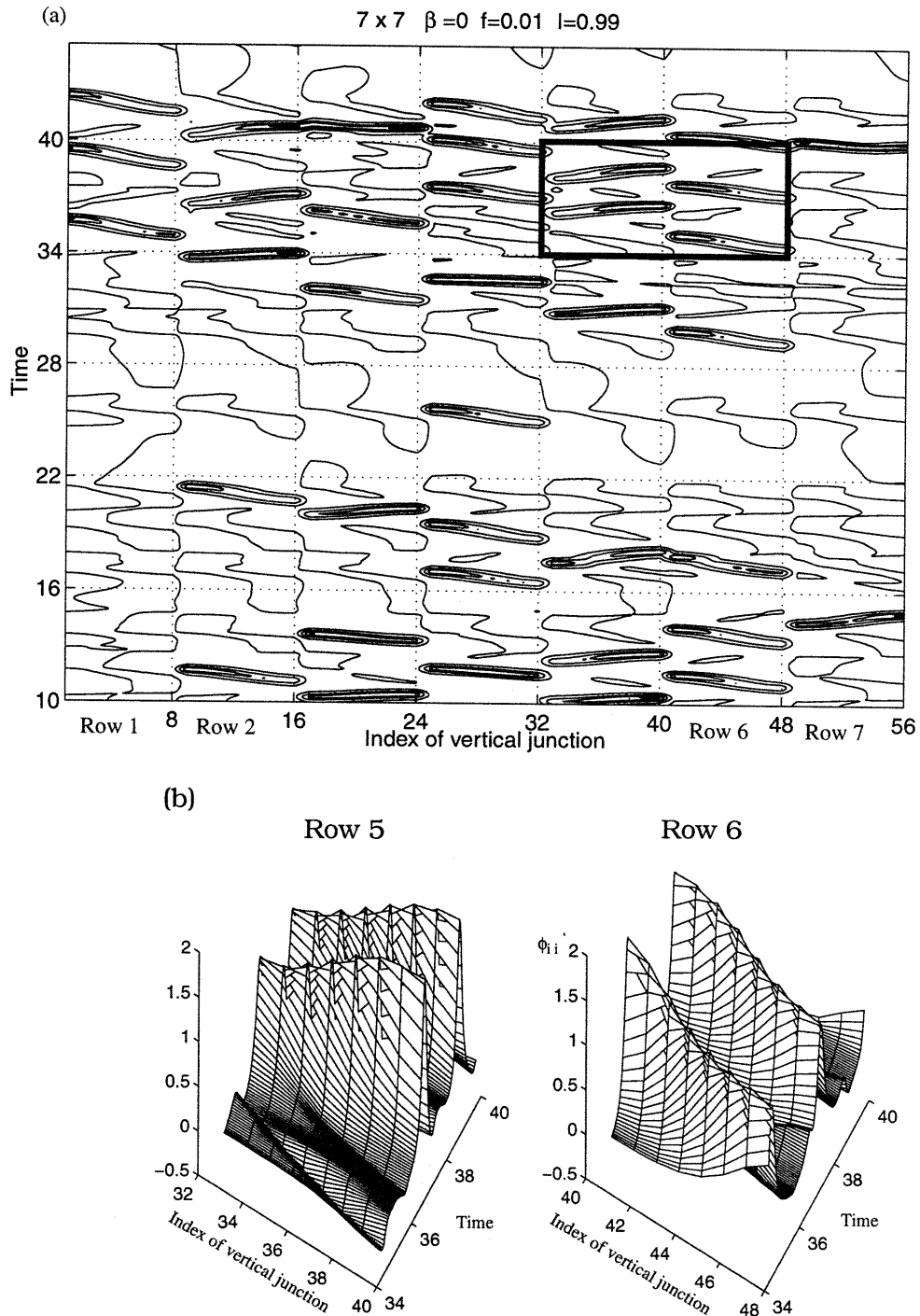


Figure 3-18: (a) Spatio-temporal diagram of the solution at very small field $f = 0.01$ close to the depinning current of the array. The solution is given by an aperiodic sequence of propagating vortices and antivortices. In (b) an enlargement corresponding to the solid rectangle shows propagating vortices, in row 6, and antivortices, in row 5, which can be viewed as reflecting from the edges of the array.

of open boundaries is enough to produce those effects without the need of extrinsic randomness. We hope to investigate in the future this and the other outlined conclusions.

3.5 Summary and discussion

In this chapter we have presented studies of square two-dimensional Josephson junction arrays. First, we have introduced the methodology to analyze the data from numerical simulations. We underline the fact that space and time averaged quantities provide a gross simplification of these systems which can present a subtle interplay of both coordinates. Specifically, spatially inhomogeneous solutions are characteristic of these arrays (as they are of other transport processes). Hence, we propose the study of spatially extended averages, together with frequency and phase velocity as a means to unfold the underlying structure. We have also established the connection between the three types of motion of the individual pendula (libration, whirling-ringing, whirling) and the three dynamical states of the array (superconducting, flux-flow, whirling).

Second, we have applied these methods, and other concepts drawn from the solutions for ladder arrays, to two-dimensional arrays. The first conclusion concerns the depinning current. Since the Meissner-like state is only stable for very small values of the field, the depinning of the array is *not* dominated by the edges, as was the case for the ladder. Here, different factors come into play since the depinning of flux-lattices is the relevant factor. Thus, the commensurability of the lattice with the underlying array will influence the critical current of the array. On the other hand, when the lattice is not commensurate we expect to have an almost constant value for the depinning current.

For the dynamical regimes, we have studied two different limits: underdamped and overdamped dynamics. In underdamped arrays, we conclude that the whirling mode is very similar to the ladder array's and the repinning picture is not modified: it will be caused by parametric instabilities with no restabilization steps being observable. Moreover, when the damping is small, row-switching events can occur. Using the

solutions for the ladder array obtained in Chapter 2, we have obtained a zeroth order solution which explains quantitatively the numerical solutions observed. In short, when a row switches, it effectively acts as a boundary which separates and uncouples the two halves (“up” and “down”) of the array. Thus, the array is divided in subunits which will now depin. The “depinning” of these subarrays corresponds to the next row-switching event. The flux-flow in underdamped arrays is not fully observable since the system jumps to this partially row-switched states.

In the overdamped arrays, row-switching is not possible. This allows the flux-flow to unfold fully. Three features are worth noting: a sequence of row-activation for small f ; the alternation of periodic and aperiodic solutions but with a strong underlying periodicity of the system; and a final transition, coincident with the continuous switch to the whirling mode, where the flexible flux-lattice turns into a rigidly displacing entity with no internal relative displacements. The appearance of these three phenomena, which have been described in systems with randomness, occurs in an ordered system and can be due to the presence of edges which break the symmetry of the system [29]. This is only one of the many unresearched directions, both numerical and analytical, which we hope to investigate in the future.

Bibliography

- [1] M. Abramowitz and I. Stegun. *Handbook of Mathematical Functions*. Dover, New York, 1965.
- [2] V. Ambegaokar and A. Baratoff. Tunneling between superconductors. *Phys. Rev. Lett.*, 10:486, 1963.
- [3] M. Avellaneda, F. Elliott, and C. Apelian. Trapping, percolation and anomalous diffusion of particles in a two-dimensional random-field. *J. Stat. Phys.*, 72:1227, 1993.
- [4] H. Beck. Anomalous vortex dynamics in two-dimensional superconducting arrays. *Phys. Rev. B*, 49:6153, 1993.
- [5] K.A. Benedict. The quasi-one-dimensional frustrated xy model. *J. Phys. : Condens. Matter*, 1:4895, 1989.
- [6] R. Bhagavatula, C. Ebner, and C. Jayaprakash. Dynamics of capacitive Josephson-junction arrays subjected to electromagnetic radiation. *Phys. Rev. B*, 45:4774, 1992.
- [7] R. Bhagavatula, C. Ebner, and C. Jayaprakash. Spatiotemporal chaos in Josephson-junction arrays. *Phys. Rev. B*, 50:9376, 1994.
- [8] P.A. Bobbert. Simulation of vortex motion in underdamped two-dimensional arrays of Josephson junctions. *Phys. Rev. B*, 45:7540, 1992.
- [9] P.A.A. Booij and S.P. Benz. Emission linewidth measurements of two-dimensional array Josephson oscillators. *Appl. Phys. Lett.*, 64:2163, 1994.

- [10] O.M. Braun and M. Peyrard. Ground-state of the Frenkel-Kontorova model with a transverse degree of freedom. *Phys. Rev. E*, 51:4999, 1995.
- [11] S.E. Burkov and A.E. Lifsic. Stability of moving soliton lattices. *Wave motion*, 5:197, 1983.
- [12] J.S. Chung, K.H. Lee, and D. Stroud. Dynamical properties of superconducting arrays. *Phys. Rev. B*, 40:6570, 1989.
- [13] C. Denniston and C. Tang. Phases of Josephson junction ladders. *Phys. Rev. Lett.*, 75:3930, 1995.
- [14] C.A. Desoer and E.S. Kuh. *Basic Circuit Theory*. McGraw-Hill, New York, 1969.
- [15] T. Doderer, V.K. Kaplunenko, J. Mygind, and N.F. Pedersen. Imaging of the dynamic magnetic structure in a parallel array of shunted Josephson junctions. *Phys. Rev. B*, 50:7211, 1994.
- [16] D. Domínguez. Critical dynamics and plastic flow in disordered Josephson junction arrays. *Phys. Rev. Lett.*, 72:3096, 1994.
- [17] D. Domínguez and J.V. José. Non-equilibrium coherent vortex states and subharmonic giant Shapiro steps in Josephson junction arrays. *Mod. Phys. B*, 8:3749, 1994.
- [18] P.G. Drazin. *Solitons: an introduction*. Cambridge University Press, New York, 1989.
- [19] D.B. Duncan, J.C. Eilbeck, H. Feddersen, and J.A.D. Wattis. Solitons on lattices. *Physica D*, 68:1, 1993.
- [20] A. Duwel, E. Trías, T.P. Orlando, H.S.J. van der Zant, S. Watanabe, and S.H. Strogatz. Resonance splitting in discrete planar arrays of Josephson junctions. *J. Appl. Phys.*, 79:7864, 1996.

- [21] W.J. Elion, J.J. Wachters, L.L. Sohn, and J.E. Mooij. Observation of the Aharonov-Casher effect for vortices in Josephson-junction arrays. *Phys. Rev. Lett.*, 71:2311, 1993.
- [22] F. Falò, A.R. Bishop, and P.S. Lomdahl. I - V characteristics in 2-dimensional frustrated Josephson-junction arrays. *Phys. Rev. B*, 41:983, 1990.
- [23] R. Fazio, U. Geigenmüller, and G. Schön. Quantum fluctuations in mesoscopic and macroscopic systems. *Quantum Chaos: Adriatico Research Conference and Miniworkshop*, ed. H.A. Cerdeira, R. Ramaswamy, M.C. Gutzwiller and G. Casati. (World Scientific), page 214, 1991.
- [24] G. Filatrella and K. Wiesenfeld. Magnetic-field effect in a two-dimensional array of short Josephson junctions. *J. Appl. Phys.*, 78:1878, 1995.
- [25] M.G. Forest, S. Pagano, R.D. Parmentier, P.L. Christiansen, M.P. Soerensen, and S.-P. Sheu. Numerical evidence for global bifurcations leading to switching phenomena in long Josephson junctions. *Wave motion*, 12:213, 1990.
- [26] Y.I. Frenkel and T. Kontorova. *Zh. Eksp. Teor. Fiz.*, 8:1340, 1938.
- [27] T.A. Fulton, R.C. Dynes, and P.W. Anderson. Flux Shuttle-Josephson junction shift register employing single flux quanta. *Proc. IEEE*, 61:28, 1973.
- [28] U. Geigenmüller, C.J. Lobb, and C.B. Whan. Friction and inertia of a vortex in an underdamped Josephson array. *Phys. Rev. B*, 47:348, 1993.
- [29] N. Grønbech-Jensen, A.R. Bishop, F. Falò, and P.S. Lomdahl. Flux-lattice noise and symmetry breaking in frustrated Josephson-junction arrays. *Phys. Rev. B*, 46:11149, 1992.
- [30] G. Grüner. The dynamics of charge-density waves. *Rev. Mod. Phys.*, 60:1129, 1988.
- [31] J. Guckenheimer and P. Holmes. *Nonlinear oscillations, dynamical systems, and bifurcations of vector fields*. Springer, New York, 1983.

- [32] T.J. Hagenaaars, P.H.E. Tiensinga, J.E. van Himbergen, and J.V. José. Nonlinear viscous vortex motion in two-dimensional Josephson junction arrays. *Phys. Rev. B*, 50:1143, 1994.
- [33] T.J. Hagenaaars, J.E. van Himbergen, J.V. José, and P.H.E. Tiesinga. Vortex reflections at boundaries of Josephson-junction arrays. *Phys. Rev. B*, 53:2719, 1996.
- [34] I-J. Hwang, S. Ryu, and D. Stroud. Screening in Josephson-junction ladders. *Phys. Rev. B*, 53:R506, 1996.
- [35] T. Iizuka. Anomalous diffusion of solitons in random-systems. *Phys. Lett. A*, 181:39, 1993.
- [36] A.K. Jain, K.K. Likharev, J.E. Lukens, and J.E. Sauvageau. Mutual phase-locking in Josephson junction arrays. *Phys. Report*, 109:309, 1984.
- [37] D.W. Jordan. *Nonlinear ordinary differential equations*. Oxford University Press, New York, 1994.
- [38] B.D. Josephson. Supercurrents through barriers. *Advan. Phys.*, 14:419, 1965.
- [39] W. Kaplan. *Advanced Calculus*. Addison-Wesley, Reading, MA, 1984.
- [40] M. Kardar. Free energies of the discrete chain in a periodic potential and the dual Coulomb gas. *Phys. Rev. B*, 30:6368, 1984.
- [41] M. Kardar. Josephson-junction ladders and quantum fluctuations. *Phys. Rev. B*, 33:3125, 1986.
- [42] R. Kleiner, P. Müller, H. Kohlstedt, N.F. Pedersen, and S. Sakai. Dynamic behavior of Josephson-coupled layered structures. *Phys. Rev. B*, 50:3942, 1994.
- [43] R. Kleiner, F. Steinmeyer, G. Kunkel, and P. Müller. Intrinsic Josephson effects in $\text{Bi}_2\text{Sr}_2\text{CaCu}_2\text{O}_8$ single-crystals. *Phys. Rev. Lett.*, 68:2394, 1992.

- [44] J.M. Kosterlitz and D.J. Thouless. Ordering, metastability and phase transitions in 2 dimensional systems. *J. Phys. C*, 6:1181, 1973.
- [45] Y. Kuramoto. Self-entrainment of a population of coupled nonlinear oscillators. *International Symposium on Mathematical Problems in Theoretical Physics*, ed. by H. Araki (Springer, NY), 39:420, 1975.
- [46] Y. Kuramoto. *Chemical oscillations, waves and turbulence*. Springer, New York, 1984.
- [47] S.G. Lachenmann, T. Doderer, D. Hoffmann, and R.P. Huebener. Observation of vortex dynamics in two-dimensional Josephson-junction arrays. *Phys. Rev. B*, 50:3158, 1994.
- [48] A.S. Landberg, Y. Braiman, and K. Wiesenfeld. Effect of disorder on synchronization in prototype two-dimensional Josephson arrays. *Phys. Rev. B*, 52:15458, 1995.
- [49] K.K. Likharev. *Dynamics of Josephson junctions and Circuits*. Gordon and Breach, New York, 1986.
- [50] C.J. Lobb, D.W. Abraham, and M. Tinkham. Theoretical interpretation of resistive transition data from arrays of superconducting weak links. *Phys. Rev. B*, 27:150, 1983.
- [51] K. Maginu. Stability of travelling wave solutions of the active Josephson-junction transmission line. *J. Diff. Eqns.*, 37:238, 1980.
- [52] A. Majhofer, T. Wolf, and W. Dieterich. Irreversible magnetization effects in a network of resistively shunted tunnel junctions. *Phys. Rev. B*, 44:9634, 1991.
- [53] I.F. Marino and T.C. Halsey. Dynamics of two-dimensional frustrated Josephson arrays. *Phys. Rev. B*, 50:6289, 1994.

- [54] T. Matsuda, K. Harada, H. Kasai, O Kamimura, and A. Tonomura. Observation of dynamic interaction of vortices with pinning centers by Lorentz microscopy. *Science*, 271:1393, 1996.
- [55] J.J. Mazo, F. Falo, and L.M. Floría. Josephson junction ladders: Ground state and relaxation phenomena. *Phys. Rev. B*, 52:10433, 1995.
- [56] J.J. Mazo, F. Falo, and L.M. Floría. Stability of metastable structures in dissipative ac dynamics of the Frenkel-Kontorova model. *Phys. Rev. B*, 52:6451, 1995.
- [57] D.E. McCumber. Effect of an ac impedance on dc voltage-current characteristics of superconductor weak-link junctions. *J. Appl. Phys.*, 39:3113, 1968.
- [58] A.A. Middleton. Asymptotic uniqueness of the sliding state for charge-density waves. *Phys. Rev. Lett.*, 68:670, 1992.
- [59] A.A. Middleton and N.S. Wingreen. Collective transport in arrays of small metallic dots. *Phys. Rev. Lett.*, 71:3198, 1993.
- [60] M. Octavio, C.B. Whan, U. Geigenmüller, and C.J. Lobb. Dynamical states of underdamped Josephson arrays in a magnetic field. *Phys. Rev. B*, 47:1141, 1993.
- [61] M. Octavio, C.B. Whan, U. Geigenmüller, and C.J. Lobb. Dynamics of underdamped Josephson arrays in a magnetic field. *Physica B*, 194-196:115, 1994.
- [62] M. Octavio, C.B. Whan, and C.J. Lobb. Phase coherence and disorder in Josephson-junction arrays. *Appl. Phys. Lett.*, 60:766, 1992.
- [63] T.P. Orlando and K.A. Delin. *Foundations of Applied Superconductivity*. Addison-Wesley, Reading, MA, 1991.
- [64] A. Petraglia, N.F. Pedersen, P.L. Christiansen, and A.V. Ustinov. Comparative dynamics of 2d shorted arrays and continuous stacked Josephson junctions. *preprint*.

- [65] M. Peyrard and M.D. Kruskal. Kink dynamics in the highly discrete sine-Gordon system. *Physica D*, 14:88, 1984.
- [66] J.R. Phillips, H.S.J. van der Zant, and T.P. Orlando. Dynamics of row switched states in Josephson-junction arrays. *Phys. Rev. B*, 50:9380, 1994.
- [67] J.R. Phillips, H.S.J. van der Zant, J. White, and T.P. Orlando. Influence of induced magnetic fields on the static properties of Josephson-junction arrays. *Phys. Rev. B*, 47:5219, 1993.
- [68] J.R. Phillips, H.S.J. van der Zant, J. White, and T.P. Orlando. Influence of induced magnetic fields on Shapiro steps in Josephson junction arrays. *Phys. Rev. B*, 50:9387, 1994.
- [69] Z.H.L. Qu, G. Hu, B.K. Ma, and G. Tian. Spatiotemporally periodic patterns in symmetrically coupled map lattices. *Phys. Rev. E*, 50:163, 1994.
- [70] D. Reinel, W. Dieterich, T. Wolf, and A. Majhofer. Flux-flow phenomena and current-voltage characteristics of Josephson-junction arrays with inductances. *Phys. Rev. B*, 49:9118, 1994.
- [71] S. Ryu, W. Yu, and D. Stroud. Dynamics of an underdamped Josephson-junction ladder. *Phys. Rev. E*, 53:2190, 1996.
- [72] M.S. Rzchowski, S.P. Benz, M. Tinkham, and C.J. Lobb. Vortex pinning in Josephson junction arrays. *Phys. Rev. B*, 42:2041, 1990.
- [73] H.R. Shea, M.A. Itzler, and M. Tinkham. Inductance effects and dimensionality crossover in hybrid superconducting arrays. *Phys. Rev. B*, 51:12690, 1995.
- [74] A.-C. Shi and A.J. Belinsky. Pinning and i - v characteristics of a two-dimensional defective flux-line lattice. *Phys. Rev. Lett.*, 67:1926, 1991.
- [75] L.L. Sohn and M. Octavio. Half-integer Shapiro steps in single-plaquette Josephson-junction arrays in a magnetic field. *Phys. Rev. B*, 49:9236, 1994.

- [76] J.M. Speight and R.S. Ward. Kink dynamics in a novel sine-Gordon system. *Nonlinearity*, 7:475, 1994.
- [77] G. Strang. *Introduction to Applied Mathematics*. Wellesley-Cambridge Press, Wellesley-Mass., 1986.
- [78] S.H. Strogatz. *Nonlinear Dynamics and Chaos*. Addison-Wesley, Reading, MA, 1994.
- [79] S.H. Strogatz and I. Stewart. Coupled oscillators and biological sunchronization. *Sci. Am.*, 269:102, 1993.
- [80] A. Pikovsky T. Bohr. Anomalous diffusion in the Kuramoto-Shivashinsky equation. *Phys. Rev. Lett.*, 70:2892, 1993.
- [81] S. Teitel and C. Jayaprakash. Josephson-junction arrays in transverse magnetic fields. *Phys. Rev. Lett.*, 51:1999, 1983.
- [82] S. Teitel and C. Jayaprakash. Phase transitions in frustrated two-dimensional xy models. *Phys. Rev. B*, 27:598, 1983.
- [83] T.S. Tighe, A.T. Johnson, and M. Tinkham. Vortex motion in 2-dimensional arrays of small, underdamped Josephson junctions. *Phys. Rev. B*, 44:10286, 1991.
- [84] T.S. Tighe, M.T. Tuominen, J.M. Hergenrother, and M. Tinkham. Measurements of charge soliton motion in two-dimensional arrays of ultrasmall Josephson junctions. *Phys. Rev. B*, 47:1145, 1993.
- [85] E. Trías, T.P. Orlando, and H.S.J. van der Zant. Self-field effects on flux-flow in two-dimensional arrays of nb Josephson junctions. *Phys. Rev. B*, submitted.
- [86] A.V. Ustinov, M. Cirillo, and B.A. Malomed. Fluxon dynamics in one-dimensional Josephson junction arrays. *Phys. Rev. B*, 47:8357, 1993.
- [87] A.V. Ustinov, H. Kohlstedt, and C. Heiden. Possible phase-locking of vertically stacked Josephson flux-flow oscillators. *Appl. Phys. Lett.*, 65:1457, 1994.

- [88] H.S.J. van der Zant, F.C. Fritschy, W.J. Elion, L.J. Geerligs, and J.E. Mooij. Field-induced superconductor-to-insulator transitions in Josephson-junction arrays. *Phys. Rev. Lett.*, 69:2971, 1992.
- [89] H.S.J. van der Zant, F.C. Fritschy, T.P. Orlando, and J.E. Mooij. Ballistic vortices in Josephson-junction arrays. *Europhys. Lett.*, 18:343, 1992.
- [90] H.S.J. van der Zant, F.C. Fritschy, T.P. Orlando, and J.E. Mooij. Vortex dynamics in two-dimensional underdamped, classical Josephson junction arrays. *Phys. Rev. B*, 47:295, 1993.
- [91] H.S.J. van der Zant, L.J. Geerligs, and J.E. Mooij. Superconductor-to-insulator transitions in non- and fully frustrated Josephson-junction arrays. *Europhys. Lett.*, 19:541, 1992.
- [92] H.S.J. van der Zant, C.J. Muller, L.J. Geerligs, C.J.P.M. Harmans, and J.E. Mooij. Coherent phase slip in arrays of underdamped Josephson tunnel-junctions. *Phys. Rev. B*, 38:5154, 1988.
- [93] H.S.J. van der Zant, T. P. Orlando, and J.E. Mooij. Phenomenological model of vortex dynamics in arrays of Josephson junctions. *Phys. Rev. B*, 43:10218, 1991.
- [94] H.S.J. van der Zant, T.P. Orlando, S. Watanabe, and S.H. Strogatz. Kink propagation in a highly discrete system - observation of phase locking to linear waves. *Phys. Rev. Lett.*, 74:174, 1995.
- [95] S. Watanabe, M. Barahona, E. Trías, H.S.J. van der Zant, S.H. Strogatz, and T.P. Orlando. To be published.
- [96] S. Watanabe, S. H. Strogatz, H.S.J. van der Zant, and T.P. Orlando. Whirling modes and parametric instabilities in the discrete sine-Gordon equation: Experimental tests in Josephson rings. *Phys. Rev. Lett.*, 74:379, 1995.

- [97] S. Watanabe and S.H. Strogatz. Constants of motion for superconducting Josephson arrays. *Physica D*, 74:197, 1994.
- [98] S. Watanabe and J. Swift. Stability of periodic solutions in series arrays of Josephson junctions with internal capacitance. *Journal of Nonlinear Science*, submitted.
- [99] S. Watanabe, H.S.J van der Zant, S.H. Strogatz, and T.P. Orlando. Dynamics of circular arrays of Josephson junctions and the discrete sine-Gordon equation. *Physica D*, submitted.
- [100] C.B. Whan, C.J. Lobb, and M.G. Forrester. Effect of inductance in externally shunted Josephson tunnel junctions. *J. Appl. Phys.*, 77:382, 1995.
- [101] K. Wiesenfeld, S.P. Benz, and P.A.A. Booij. Phase-locked oscillator optimization for arrays of Josephson junctions. *J. Appl. Phys.*, 76:3835, 1994.
- [102] A.T. Winfree. *The geometry of biological time*. (Biomathematics, vol. 8) Springer, New York, 1980.
- [103] W. Yu, E.B. Harris, S.E. Hebboul, J.C. Garland, and D. Stroud. Fractional Shapiro steps in ladder Josephson arrays. *Phys. Rev. B*, 45:12624, 1992.
- [104] W. Yu and D. Stroud. Vortex motion and vortex-friction coefficient in triangular Josephson-junction arrays. *Phys. Rev. B*, 49:6174, 1994.
- [105] W.B. Yu, K.H. Lee, and D. Stroud. Vortex motion in Josephson-junction arrays near $f=0$ and $f=1/2$. *Phys. Rev. B*, 47:5906, 1993.
- [106] S.P. Yukon and N.C.H. Lin. Dynamics of triangular and tetrahedral Josephson junction oscillator arrays. *IEEE Trans. Appl. Supercond.*, 5:2959, 1995.

O weiter, stiller Friede!
So tief im Abendrot.
Wie sind wir wandermüde—
ist dies etwa der Tod?

J. von Eichendorff